

- 4 AUG 2004

- 2 JUL 2004

10369218

40 0748146 4



ProQuest Number: 10182979

All rights reserved

INFORMATION TO ALL USERS

The quality of this reproduction is dependent upon the quality of the copy submitted.

In the unlikely event that the author did not send a complete manuscript and there are missing pages, these will be noted. Also, if material had to be removed, a note will indicate the deletion.



ProQuest 10182979

Published by ProQuest LLC (2017). Copyright of the Dissertation is held by the Author.

All rights reserved.

This work is protected against unauthorized copying under Title 17, United States Code  
Microform Edition © ProQuest LLC.

ProQuest LLC.  
789 East Eisenhower Parkway  
P.O. Box 1346  
Ann Arbor, MI 48106 – 1346

# **42 GHZ MULTIMEDIA WIRELESS SYSTEM - MEASUREMENT AND ANALYSIS**

**Ee Beng, Lam**

A thesis submitted in partial fulfilment of the requirements of  
The Nottingham Trent University for the degree of  
Doctor of Philosophy

Faculty of Construction, Computing & Technology  
School of Computing & Technology  
The Nottingham Trent University  
United Kingdom

**April 2004**

Collaborating establishment:  
MMRadiolink Ltd. (Philips, U.K.)

This copy of the thesis has been supplied on condition that anyone who consults it is understood to recognise that its copyright rests with the author and that no quotation from the thesis and no information derived from it may be published without the author's prior written consent.

## ABSTRACT

Millimetre-wave broadband fixed wireless access systems are particularly suited to meet the growing demand for the provision of cost-effective, high capacity broadcast, data and telecommunication services over the 'last-mile' connection between the service provider and the user's home. In Europe, the allocated spectrum band of 40.5-43.5 GHz for Multimedia Wireless System is envisaged to support the convergence and provision of these services.

The research detailed in this thesis focuses on the investigation and development of relevant hardware and infrastructure necessary to establish long-term, widespread field measurements on a live 42 GHz Multimedia Wireless System.

The 42 GHz campus network experimental test-bed, on which the field measurements are based, is described. This includes an investigation into equipment integration, radio calibration, and provision of digital video and high-speed data network services into the local trial area. In order to facilitate signal measurements, an innovative, low-cost measurement system was developed. Utilising a custom-designed data acquisition module in combination with off-the-shelf satellite set-top boxes and an inexpensive weather station, a system able to monitor and log various parameters of the millimetre-wave signal and meteorological conditions has been developed, and successfully integrated into the field measurement campaign. Novel application of an iterative cumulative sum analysis with associated randomisation test, is shown to successfully mitigate the variation in the long-term local mean level of the measured, received signal power, arising due to system gain variation. This has enabled accuracy to be maintained despite the low cost of the measurement system.

Measured data from the field are statistically analysed within the specific context of long-term precipitation, propagation through foliage and the spatial correlation of precipitation fade. The results obtained and the empirically-drawn conclusions are compared to measurements, predictions and models where available in the literature. These results include the testing of the ITU-R availability prediction model using data from consecutive years and different sites, substantiation of the fade duration model, and the effects of seasonal and weather variation on the millimetre-wave signal as it propagates through foliage.

This thesis is dedicated to the following persons  
who have always stood by me,  
and have inspired and believed in me:

My parents, Mr. and Mrs. Lam Peng Kooi

My girlfriend, Ms. Ariel Tang

And my supervisor, Dr. Richard Germon

## ACKNOWLEDGEMENTS

First and foremost, I would like to express my sincere appreciation to my supervisor, Dr. Richard Germon, for his invaluable inspiration, encouragement and support throughout my doctoral study. I am greatly indebted to him and this dissertation is an acknowledgement of his tenacity and his confidence in me. Thank you.

The implementation and carrying out of the field measurement campaign is never a solo task. I would like to acknowledge the advice and technical aid that I received from the research sponsor, MMRadiolink Ltd. (Philips U.K.), and from the technicians and staff members of the faculty. Special thanks go to Mr. Chris Oswald for working closely with me on the initial set up of the campus network trial. I am also grateful to my colleagues, Leon Mun and Adrian Chuah, for always being there to lend a helping hand. Many thanks as well to Dr. Steve Clark and Dr. Paul Evans for sharing their enthusiasm for research work with me, and making me understand that doing research is truly a privilege.

I would also like to thank my girlfriend, Ariel Tang, for constantly motivating me to complete this thesis. Her patience and understanding on my desire to do this research is more than I can ask for.

No words can express my deep gratitude to my parents and sisters back in Malaysia for their love, encouragement and understanding throughout the years, more than ever during the last 5 years of my study overseas. Especially to my mother who has taught me to be thorough in whatever I do, and to approach every challenge to the best of my ability.

A quick note of appreciation is also in order to the group of Ninjutsu practitioners from the Nottingham Hombu Dojo, for their friendship, encouragement and humour which have brightened the dry periods of this research.

Last, but not least, it is my pleasure to acknowledge the support of equipment from MMRadiolink Ltd., without which this Ph.D. work would not have been possible.

## TABLE OF CONTENT

<b>ABSTRACT .....</b>	<b>I</b>
<b>ACKNOWLEDGEMENTS .....</b>	<b>III</b>
<b>TABLE OF CONTENT .....</b>	<b>IV</b>
<b>LIST OF ACRONYMS.....</b>	<b>VII</b>
<b>LIST OF FIGURES .....</b>	<b>IX</b>
<b>LIST OF TABLES .....</b>	<b>XIII</b>
<b>1 INTRODUCTION.....</b>	<b>1</b>
1.1 TRENDS TOWARD MILLIMETRE-WAVE SYSTEM .....	3
1.2 MWS ACCESS NETWORK .....	4
1.3 42 GHZ MWS CAMPUS NETWORK TRIAL.....	5
1.4 RESEARCH OBJECTIVES.....	6
1.5 RESEARCH ACHIEVEMENTS .....	7
1.6 STRUCTURE OF THE THESIS.....	8
<b>2 MILLIMETRE-WAVE BROADBAND FIXED RADIO ACCESS .....</b>	<b>10</b>
2.1 42 GHZ MWS CAMPUS NETWORK TRIAL MEASUREMENT TEST-BED SET UP .....	11
2.1.1 <i>Service Provision</i> .....	11
2.1.2 <i>MWS Configuration</i> .....	14
2.1.3 <i>Radio Subsystem Calibration</i> .....	19
2.1.4 <i>Remote Sites Deployment</i> .....	21
2.2 TRIALS AND RESEARCH WORK ON MILLIMETRE-WAVE SYSTEMS.....	25
2.2.1 <i>Channel Measurements from Trials and Research Work</i> .....	26
2.3 PROPAGATION AND RECEPTION FUNDAMENTALS .....	27
2.3.1 <i>Path Loss Model</i> .....	27
2.3.2 <i>Link Budget</i> .....	28
2.4 TERRESTRIAL MILLIMETRE-WAVE PROPAGATION.....	29
2.4.1 <i>Refraction - Refractive Index Change</i> .....	29
2.4.2 <i>Reflection - Rough Surface</i> .....	29
2.4.3 <i>Diffraction - Fresnel Zone Clearance</i> .....	30
2.4.4 <i>Attenuation and Scattering - Effects of Vegetation</i> .....	31
2.4.5 <i>Attenuation and Scattering - Effects of Precipitation</i> .....	34
2.5 42 GHZ MWS SPECIFIC ISSUES .....	35
2.5.1 <i>Effect of Blockage – Area Coverage</i> .....	35
2.5.2 <i>Effect of Precipitation - Availability Predictions</i> .....	36
2.5.3 <i>Effect of Precipitation - Link Availability</i> .....	38

2.5.4	<i>Effect of Precipitation - Diversity</i> .....	39
2.5.5	<i>Effect of Foliage – Attenuation Prediction</i> .....	40
2.5.6	<i>Effect of Foliage - Variation in Fade</i> .....	41
2.5.7	<i>Effect of Foliage – Flat Fading</i> .....	43
2.5.8	<i>Effect of Buildings and Terrain - Multipath</i> .....	43
2.6	RESEARCH DIRECTIONS .....	45
<b>3</b>	<b>COST-EFFECTIVE MEASUREMENT SYSTEM</b> .....	<b>48</b>
3.1	MEASUREMENT SYSTEM DESIGN REQUIREMENTS.....	50
3.2	MILLIMETRE-WAVE SIGNAL MEASUREMENT .....	51
3.2.1	<i>Definition of Signal Parameters</i> .....	51
3.2.2	<i>Signal Measurement via Satellite STB</i> .....	53
3.2.3	<i>Signal Power Measurement and Calibration</i> .....	55
3.2.4	<i>BER Measurement</i> .....	60
3.2.5	<i>Frequency Offset Measurement and Calibration</i> .....	62
3.3	DATA ACQUISITION MODULE FOR SATELLITE STB .....	65
3.3.1	<i>Satellite STB Operation</i> .....	65
3.3.2	<i>I<sup>2</sup>C Bus Specifications</i> .....	66
3.3.3	<i>DAM Design Requirements</i> .....	67
3.3.4	<i>SRAM Based DAM</i> .....	70
3.3.5	<i>Assembly Language Program for SRAM Based DAM</i> .....	73
3.3.6	<i>SmartMedia Based DAM</i> .....	76
3.3.7	<i>Assembly Language Program for SmartMedia Based DAM</i> .....	79
3.4	METEOROLOGICAL DATA MEASUREMENT .....	83
3.4.1	<i>Meteorological Data via 1-Wire Weather Station</i> .....	83
3.4.2	<i>Rainfall Rate Measurement</i> .....	84
3.4.3	<i>Wind Speed Measurement</i> .....	85
3.4.4	<i>Temperature Measurement</i> .....	86
3.5	DATA ACQUISITION MODULE FOR WEATHER STATION.....	87
3.5.1	<i>1-Wire Bus Specifications</i> .....	87
3.5.2	<i>DAM Design Requirement</i> .....	87
3.5.3	<i>Weather Station DAM</i> .....	88
3.5.4	<i>Assembly Language Program for Weather Station DAM</i> .....	89
3.6	FADE SIMULATION SYSTEM .....	92
3.6.1	<i>FSS Design Requirements</i> .....	92
3.6.2	<i>FSS Hardware Development</i> .....	93
3.6.3	<i>Assembly Language Program for FSS</i> .....	94
3.6.4	<i>FSS Calibration Results</i> .....	95
3.7	SUMMARY .....	96
<b>4</b>	<b>IDENTIFYING CHANGES IN THE LOCAL MEAN</b> .....	<b>98</b>

4.1	CHANGES OF LOCAL MEAN IN LONG-TERM MEASUREMENT TRIAL .....	99
4.1.1	<i>Radio Subsystem Gain Variation</i> .....	99
4.1.2	<i>Effect of Varying Local Mean</i> .....	101
4.1.3	<i>Characteristic of Measured Data</i> .....	103
4.1.4	<i>Local Mean Problem Statement</i> .....	104
4.2	CUSUM ANALYSIS OF A SINGLE CHANGE IN THE LOCAL MEAN.....	105
4.2.1	<i>Monitored Data as Mean-Shift Model</i> .....	107
4.2.2	<i>CUSUM Method</i> .....	108
4.2.3	<i>Randomisation Test</i> .....	110
4.2.4	<i>Significance of CUSUM Plots</i> .....	111
4.2.5	<i>Least-Square Estimation of Change-Point</i> .....	112
4.3	ITERATIVE CUSUM ANALYSIS OF MULTIPLE CHANGES IN LOCAL MEAN.....	112
4.3.1	<i>Detection of Potential Change-Points</i> .....	112
4.3.2	<i>Reassessment of Change-Points</i> .....	113
4.3.3	<i>Local Mean Data Segmentation</i> .....	113
4.3.4	<i>Software Implementation of Proposed Algorithm</i> .....	114
4.4	HARDWARE TEST OF PROPOSED ALGORITHM.....	115
4.5	POWER OF ITERATIVE CUSUM ANALYSIS.....	117
4.6	SUMMARY .....	119
<b>5</b>	<b>ANALYSIS OF FIELD MEASUREMENT RESULTS.....</b>	<b>121</b>
5.1	LONG-TERM FADE STATISTIC.....	123
5.1.1	<i>Fade Non-Exceedance Statistic</i> .....	124
5.1.2	<i>Fade Duration Statistic</i> .....	127
5.2	DYNAMICS OF FOLIAGE BLOCKAGE.....	130
5.2.1	<i>Measurement Set Up</i> .....	131
5.2.2	<i>Through Tree Signal Power Variation Characteristics</i> .....	133
	<i>Fade Variation Statistic</i> .....	139
5.2.3	<i>Fade Non-Exceedance Statistic</i> .....	147
5.3	ROUTE DIVERSITY IMPROVEMENT .....	149
5.4	INHOMOGENEITY OF PRECIPITATION EVENT .....	150
5.4.1	<i>Diversity Statistic</i> .....	152
5.5	SUMMARY .....	154
<b>6</b>	<b>CONCLUSIONS .....</b>	<b>155</b>
6.1	SUMMARY AND CONCLUSION FROM WORK DONE.....	156
6.2	FURTHER RESEARCH WORK .....	159
	<b>LIST OF PUBLICATIONS .....</b>	<b>160</b>
	<b>REFERENCES.....</b>	<b>161</b>
	<b>APPENDIX A - PHOTOS OF REMOTE SITES.....</b>	<b>174</b>

## LIST OF ACRONYMS

AGC	Automatic Gain Control
ALC	Automatic Level Control
ADC	Analogue-To-Digital Converters
AWGN	Additive White Gaussian Noise
A-D	Anderson-Darling
BER	Bit Error Rate
BFWA	Broadband Fixed Wireless Access
CRABS	Cellular Radio Access for Broadband Services
CNR	Carrier-to-Noise Ratio
CPE	Customer Premises Equipment
CW	Carrier Wave
CUSUM	Cumulative Sum
DAM	Data Acquisition Module
DRO	Dielectric Resonant Oscillator
DTH	Direct-to-Home
DVB	Digital Video Broadcasting
DVB-RC	DVB Return Channel for Cable
DVB-S	DVB Satellite
DVB-T	DVB Terrestrial
ERC	European Radiocommunications Committee
FSS	Fade Simulation System
FEC	Forward Error Correction
GOF	Goodness-of-Fit
HFC	Hybrid Fibre Coaxial Cable
i.i.d.	Independent and Identically Distributed
I <sup>2</sup> C	Inter-IC
IC	Integrated Circuit
IDU	Indoor Unit
IF	Intermediate Frequency
INA	Interactive Network Adapter
IP	Internet Protocol

IRD	Integrated Receiver Decoders
ITU-R	International Telecommunications Union Radiocommunication Sector
K-S	Kolmogorov-Smirnov
LMDS	Local Multipoint Distribution System
LOS	Line of Sight
LVDS	Low Voltage Differential Signal
MMIC	Monolithic Microwave Integrated Circuit
MPEG	Motion Picture Expert Group
MPEG-2	MPEG Layer 2
MPEG-2 TS	MPEG-2 Transport Layer
MWS	Multimedia Wireless System
NED	Non-Exceedance Distribution
NECD	Non-Exceedance Cumulative Distribution
ODU	Outdoor Unit
QEF	Quasi Error Free
QPSK	Quadrature Phase Shift Keying
RAL	Rutherford Appleton Laboratory
RAM	Random Access Memory
RS	Reed Solomon
SDD	Satellite Demodulator and Decoder
STB	Satellite Set-top Box
UART	Asynchronous Receiver Transmitter
USB	Universal Serial Bus

## LIST OF FIGURES

Figure 1-1: Basic MWS network configuration.....	4
Figure 2-1: Broadcast service digital video source.....	13
Figure 2-2: Head-end radio transceiver architecture.....	15
Figure 2-3: Head-end base station network topology.....	16
Figure 2-4: Campus network trial frequency and polarisation plan.....	17
Figure 2-5: User-end broadcast only reception radio receiver architecture.....	17
Figure 2-6: User-end broadcast only reception system set up.....	18
Figure 2-7: User-end two-way system set up.....	19
Figure 2-8: User-end radio receiver chain gain response.....	20
Figure 2-9: User-end radio transceiver receiver chain gain response.....	21
Figure 2-10: Photo of the base station millimetre-wave radio transceiver.....	22
Figure 2-11: Campus network trial cell coverage.....	23
Figure 2-12: Campus network trial radio links layout.....	23
Figure 2-13: Rough surface scattering.....	29
Figure 2-14: Knife-edge diffraction.....	31
Figure 2-15: Potential sources of multipath propagation.....	43
Figure 2-16: Geometry for a two path channel due to reflection.....	44
Figure 3-1: Satellite STB architecture block diagram.....	53
Figure 3-2: Satellite STB front-end architecture.....	54
Figure 3-3: Configuration of signal measurement system.....	55
Figure 3-4: AGC block layout.....	55
Figure 3-5: $AGC_{amp}$ calibration result.....	57
Figure 3-6: $AGC_{amp}$ calibration steps.....	57
Figure 3-7: $AGC_{amp}$ corresponding actual power level.....	58
Figure 3-8: $AGC_{amp}$ range test.....	59
Figure 3-9: $AGC_{amp}$ response test.....	60
Figure 3-10: Pre-Viterbi BER measurement.....	61
Figure 3-11: Different stages of $E_b/N_0$ measurement.....	61
Figure 3-12: Phase-frequency loop block layout.....	63
Figure 3-13: Frequency offset measurement calibration result.....	63
Figure 3-14: Frequency offset measurement accuracy test.....	64

Figure 3-15: I <sup>2</sup> C bus communication protocol.....	66
Figure 3-16: DAM top level block diagram. ....	67
Figure 3-17: I <sup>2</sup> C bus data waveform. ....	69
Figure 3-18: SRAM based DAM components layout. ....	71
Figure 3-19: Photo of the SRAM based DAM. ....	73
Figure 3-20: SRAM based DAM program flowchart. ....	74
Figure 3-21: SRAM based DAM program subroutines.....	76
Figure 3-22: SmartMedia based DAM components layout.....	77
Figure 3-23: Photo of the SmartMedia based DAM. ....	79
Figure 3-24: SmartMedia based DAM program flowchart. ....	80
Figure 3-25: Block replacements following SmartMedia write failure.....	81
Figure 3-26: SmartMedia based DAM program subroutines. ....	82
Figure 3-27: Installation of 1-Wire weather station. ....	84
Figure 3-28: Weather station DAM components layout. ....	88
Figure 3-29: Weather station DAM program flowchart.....	90
Figure 3-30: Weather station DAM program additional subroutines.....	91
Figure 3-31: FSS top level block diagram. ....	92
Figure 3-32: FSS components layout. ....	93
Figure 3-33: Photo of satellite STB calibration via the FSS.....	94
Figure 3-34: FSS program flowchart.....	94
Figure 3-35: FSS calibration result. ....	95
Figure 3-36: FSS response test.....	96
Figure 4-1: Temperature induced gain variation of user-end radio receiver. ....	100
Figure 4-2: Temperature induced gain variation of user-end radio transceiver.....	101
Figure 4-3: Received signal power variation for a typical site. ....	103
Figure 4-4: Data segmentation of a fade event. ....	104
Figure 4-5: Overview algorithm flowchart for single local mean change identification. .	106
Figure 4-6: Possible CUSUM chart variations. ....	109
Figure 4-7: Iterative CUSUM analysis algorithm flowchart. ....	114
Figure 4-8: Hardware test for iterative CUSUM analysis. ....	115
Figure 4-9: Local mean detection test. ....	116
Figure 4-10: Local mean detection test in the present of fade events. ....	117
Figure 4-11: Identified local means from iterative CUSUM analysis.....	118
Figure 4-12: Variation of non-exceedance curves with baseline level.....	118

Figure 5-1: Effect of precipitation on the received signal power..... 123

Figure 5-2: Link  $L_{BHall}$  fade NECD for year of 2002. .... 124

Figure 5-3: Link  $L_{BHall}$  fade NECD for year of 2003. .... 125

Figure 5-4: Link  $L_{Home\ LOS}$  fade NECD for year of 2003. .... 126

Figure 5-5: Link  $L_{BHall}$  fade duration NECD for year of 2003 (prediction given as smooth line plot). .... 128

Figure 5-6: Aerial view of the spatial diversity links path profile. .... 131

Figure 5-7: Photo of the spatial diversity link set up. .... 132

Figure 5-8: Measured received signal power from spatial diversity link. .... 134

Figure 5-9: Influence of wind speed and rain on signal variation..... 135

Figure 5-10: Influence of seasonal transition from in-leaf to out-of-leaf on through tree signal variation. .... 136

Figure 5-11: Photos of the sycamore tree covering the time period of (a) in-leaf-segment, (b) yellow-senescing, (c) rapid leaf shedding, and (d) out-of-leaf. .... 136

Figure 5-12: Influence of wind speed and rain on the through tree signal variation. .... 137

Figure 5-13: Service quality of the through tree broadcast signal. .... 138

Figure 5-14: Fade diurnal variation..... 139

Figure 5-15: Influence of wind speed on fade variation NED for in-leaf, arid condition, for (a) link  $L_{Home\ LOS}$ , (b) Link  $L_{Tree+path}$ , and (c) link  $L_{Tree}$ . .... 140

Figure 5-16: Influence of wind speed on fade variation NED for in-leaf, rain condition, for (a) link  $L_{Home\ LOS}$ , (b) Link  $L_{Tree+path}$ , and (c) link  $L_{Tree}$ . .... 142

Figure 5-17: Influence of wind speed on fade variation NED for arid condition and link  $L_{Tree}$ , for (a) yellow-senescing, and (b) rapid leaf shedding..... 143

Figure 5-18: Distribution fitting of link  $L_{Tree}$  fade variation NED for  $ws \geq 0$  m/s, arid condition..... 144

Figure 5-19: Distribution fitting of link  $L_{Tree}$  fade variation NED for  $ws \geq 0$  m/s, rain condition..... 145

Figure 5-20: Influence of wind speed on fade NECD for in-leaf, (a) arid, and (b) rain condition..... 147

Figure 5-21: Path details for route diversity analysis using link  $L_{Home\ LOS}$  and  $L_{BHall}$ . .... 150

Figure 5-22: Received signal power of link  $L_{Home\ LOS}$  and  $L_{BHall}$  for the month of June. .. 150

Figure 5-23: Received signal power of link  $L_{Home\ LOS}$  and  $L_{BHall}$  during rain event on 01/06/03. .... 151

Figure 5-24: Received signal power of link $L_{Home\ LOS}$ and $L_{BHall}$ during rain event on 18/06/03. ....	151
Figure 5-25: Route diversity improvement to fade NECD for year of 2003. ....	152
Figure 5-26: Route diversity improvement factor for year of 2003. ....	153

## LIST OF TABLES

Table 2-1: Deployed remote sites radio link details.....	24
Table 3-1: Breakdown of signal parameter data bytes. ....	68
Table 3-2: DAM requirements under different satellite STB modes. ....	70
Table 3-3: Breakdown of meteorological parameter data bytes. ....	88
Table 5-1: Tabulated $R_A$ for link $L_{BHall}$ . ....	127
Table 5-2: Segmentation of the through tree signal variation measurement period. ....	139
Table 5-3: GOF test for distribution fitting of link $L_{Tree}$ fade variation NED for different wind speed range, under arid condition. ....	144
Table 5-4: GOF test for distribution fitting of link $L_{Tree}$ fade variation NED for different wind speed range, under rain condition. ....	145
Table 5-5: Parameters for best empirical fitted distribution of link $L_{Tree}$ fade variation NED for different wind speed range, under arid condition. ....	146
Table 5-6: Parameters for best empirical fitted distribution of link $L_{Tree}$ fade variation NED for different wind speed range, under rain condition. ....	147

## Chapter 1

# Introduction

Terrestrial millimetre-wave broadband fixed wireless access (BFWA) systems, such as 42 GHz Multimedia Wireless System (MWS), are particularly applicable to the growing demand for the provision of cost-effective, high-capacity broadcast, data and telecommunication services over the 'last-mile' connection between the service provider and the users' home [1, 2]. A MWS essentially consists of all the network elements necessary for it to serve as a generic delivery mechanism for providing broadband services to multiple users in the same geographic area, using millimetre-wave radio as the fundamental transport medium. It operates in the spectrum band of 40.5-43.5 GHz that has been designated by regulatory organisations as the harmonised band for the introduction of MWS in Europe following a European Radiocommunications Committee (ERC) decision [3]. With such large available bandwidth, MWS could support and provide the said services.

The suitability of 42 GHz MWS is, however, hampered by the limited range and coverage over which such systems can provide an effective service, as a result of propagation effects and blockage considerations [1]. Restrictions due to propagation arise when the propagation medium for the millimetre-wave signal is perturbed by atmospheric effects, the most dominant of which being precipitation. These effects are more significant at millimetre-wave frequencies, and in the case of precipitation, cause excess attenuation to the propagating signal. The blockage restriction that occurs owing to terrain, foliage and building, forms shadowed regions that are shielded from having clear line of sight (LOS) to the transmitting base station. As the millimetre-wave signal impinges on the different

blockages, it generally suffers severe attenuation, thus confining the MWS to having radio links that are dictated by the need of LOS between transmitting and receiving antennas.

At the current time, the studies of 42 GHz MWS and the associated millimetric transport medium are by no means exhaustive, particularly when it comes to the available statistical information on long-term link and system performance of realistic deployed radio links under different spatial distribution and propagation scenarios. Such studies, and the associated analysis, are important in providing insight into reliable MWS design and deployment.

The most direct method to investigate these millimetre-wave transmissions in order to achieve meaningful statistical models and verify propagation theory is via signal measurements. Since the studies should ideally mirror a realistic deployment, a long-term field measurement campaign covering the appropriate measurement sites will need to be carried out. Hence, both the enabling core 42 GHz MWS network and an appropriate measurement system need to be made available. This core network will serve as the experimental test-bed that provides the signal source and remote sites from which field measurements can be made and carried out from. The requirement for numerous measurement sites necessitates the development of a cost-effective measurement system to ensure that the field measurement campaign will not be limited by cost constraints.

In addition, for MWS to be commercially viable, it must be able to offer a rich set of services at an affordable cost to consumers. One way of accomplishing this is to make use of existing services flexibly, which drives the requirement for investigation into determining efficient interoperability between MWS and the different available broadcast and interactive technologies.

## 1.1 Trends toward Millimetre-wave System

One of the main focus areas of telecommunication today is the provision of efficient transport capacity, at acceptable cost, for the so-called 'last-mile' connection; the access network [1, 2]. The need for on-demand, broadband capacity has increased at a remarkable rate as a consequence of the increasing use of not only voice communication, but also capacity demanding data and multimedia applications. A recently published strategic report on worldwide broadband access forecasts that the number of broadband Internet connections will overtake narrow band by year 2007, with almost 300 million businesses and residents being connected via different access technologies [4]. Of this, broadband business premises will exceed 30 million, of which one-third will be located in Western Europe.

Existing network operators, from both broadcast and telecommunication, are facing the broadband requirement challenge by leveraging on and improving existing technologies [5]. The first step of digitising the broadband access network has already been made to allow the wireline and wireless technologies to cover a wide range of services. Broadcast networks are developed into two-way networks through the addition of an interactive channel that is very often based on a different technology [6]. The conversion of broadcast satellite networks and cable TV networks into interactive networks are representative examples. For the telecommunication side, upgrading on existing copper networks is undertaken to facilitate possibilities of transport capacities in the megabits-per-second range.

All these developments are in parallel with the current broadband access trend in Europe which is characterised by the ongoing deregulation of the traditional market segment of telecommunication, data and broadcast services [7]. This implies that the hitherto largely separate market segments are gradually being replaced by network operators offering multiple or full services in a strongly competitive market-place.

To provide profitable operation in this environment, the operators of access networks must, in general, be able to operate at low take-up rates and with rapidly changing service requirements. These circumstances lead to the demand of a highly flexible, scaleable and cost-effective access technology offering broadband capacities. In this context BFWA

technology has, through the recent development and demonstration of MWS [8] in providing broadcast and interactive services, become a proven alternative for broadband access.

The adoption of millimetre-wave frequencies for realising broadband radio access systems is primarily due to the uniquely large bandwidth availability of up to several hundreds of megahertz (MHz), which is non-existent in the congested lower frequencies. Since the signal propagation at these frequencies is limited in range, the resulting small coverage cell size allows high frequency reuse potential [9, 10] which effectively increases system capacity. For a fixed antenna size, the gain of the antenna increases with frequency [11, 12]. Consequently, the use of millimetre-wave transmission is an advantage where a high gain antenna is required, as the antenna size will be smaller and less obtrusive.

## 1.2 MWS Access Network

The size and shape of a MWS cell serving a local geographical area are determined by coverage, single-cell network capacity and access network availability. A typical cell is composed of a 90° sector with a diameter of 2-5 km. Figure 1-1 depicts the configuration for a basic MWS network cell.

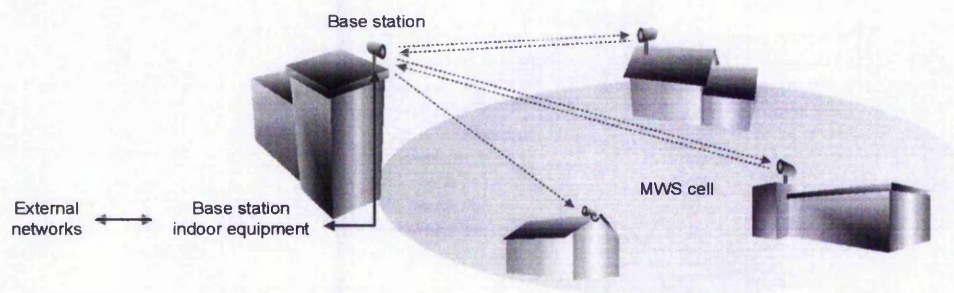


**Figure 1-1: Basic MWS network configuration.**

The main constituting network elements for providing broadband access are the base station at the head-end, and the customer premises equipment (CPE) on the user-end. Conversion from the wired to wireless infrastructure occurs at the base station, in which the base station connects the cell to the external networks and provides connections to individual CPEs. Due to the directional antenna of the CPE, the radio topology for the latter connection is a point-to-multipoint downlink from the base station, while the uplink

from an individual CPE is through a point-to-point uplink. The radio transceiver of the base station is generally sited at an elevated position, and provides a single sector edge-feed cell into the local area. Full coverage around a base station thus requires a number of radio transceivers corresponding to the beamwidth coverage of each one. Termination of the MWS network at the customer site is provided by the CPE.

The advantages offered by the MWS can be summarised as follows [13]:

- Possible multi-gigabit capacity following large allocated bandwidth, enabling the provision of various broadband services.
- Ease and speed of system deployment with minimal disruption to the community and environment.
- Lower entry and deployment costs, as customer premise equipment is not pre-installed.

### **1.3 42 GHz MWS Campus Network Trial**

The campus network trial project was undertaken by the Communication Research Group of The Nottingham Trent University to establish a campus wide 42 GHz MWS radio network, through sponsoring of MMRadioLink Ltd. (Philips, U.K.) and Hughes Network Systems Ltd. The trial is based at the university's city campus in the centre of Nottingham, with links from the base station at the university's main building to other university buildings and departments, halls of residence and individual homes. This radio access network enables extension of the existing university network to remote sites, with provision of services such as high-speed university Intranet and Internet access and broadcast digital TV [14, 15, 16].

The campus network trial philosophy is summarised as follows:

- Demonstration of a live 42 GHz MWS access network offering broadband broadcast and interactive services.
- Provision of an experimental test-bed for investigation into millimetre-wave propagation, network performance and quality at 42 GHz.
- Examination of equipment integration and service provision issues for a MWS network.

- Exploration of possible new applications and services that can be facilitated by the high-capacity transport medium.

The trial aims to establish a live multi-user radio network on which to demonstrate broadband applications and to undertake analysis of the link and system performance, including equipment and integration issues, as well as deployment and implementation of the radio hardware [14, 15]. Of these analyses, the core investigation will come from the envisaged long-term, widespread field measurement campaign which monitors the 42 GHz wideband millimetre-wave transmission under the various realistic deployment scenarios, and in a live network which is providing services.

As a trial environment, the university campus has a number of contributing attributes [16]. Implementation of a broadband radio network is simplified with access to existing high capacity communication networks, connection to a broadband data backbone and extensive real-estate infrastructure. Most students and staff are familiar with using the existing university network facilities and have work patterns that enable them to participate constructively in a trial of this type. Furthermore, many of them live within the coverage of the campus network cell. In addition, other departments in the university could also potentially make use of this broadband access technology in unique ways, such as the distribution of content created by students.

#### **1.4 Research Objectives**

The main thrust of this research programme concentrates on the investigations and set up of the relevant hardware and infrastructure necessary to establish a long-term field measurement campaign, obtain accurate and useful field trial measurements, and analyse the measured data and its implication with the aim towards presenting results that can be used to devise new approaches for 42 GHz MWS design and deployment. The investigation philosophy of the long-term field measurement campaign is to research the performance of deployed 42 GHz wideband millimetre-wave radio links under different scenarios of coverage, blockage and propagation effects as encountered in a real deployment.

The objectives that facilitate the said investigations are summarised as follow:

- Setting up of a basic real live 42 GHz MWS network which provides broadcast and interactive services.
- Investigation and development of cost-effective means for long-term monitoring of the transmission performance and quality of the 42 GHz radio link.
- Establishing and maintaining a long-term field measurement campaign.
- Statistical analysis of field trial measurement data with aim of verifying and contributing to available predictions and procedures for 42 GHz MWS.

## 1.5 Research Achievements

The undertaken work in this research has resulted in the following main contributions:

- Provision of a reliable digital video source using cost-effective digital terrestrial front-end modules, in place of professional terrestrial integrated receiver decoders, which are an order of magnitude more expensive. The obtained digital video feed is required for the provision of broadcast service.
- Setting up of the core 42 GHz MWS campus network trial which provides broadcast and interactive services\*. The MWS network serves as the underlying experimental test-bed on which the field measurement campaign can thus be carried out.
- Development of a cost-effective signal measurement system which utilises an off-the-shelf satellite set-top box in combination with a custom built data acquisition module. The signal measurement system facilitates widespread, long-term field measurements, of the 42 GHz wideband millimetre-wave signal received by the radio receiver, with potential for further multiple sites without significant cost constraint.
- Development of a similarly cost-effective meteorological measurement system which measures rainfall, wind speed and direction, and temperature, to enable correlation of the collected signal data to the weather condition under which the measurement is made.

---

\* This was undertaken with the appropriate technical support from the university and sponsoring companies.

- Novel implementation of an iterative cumulative sum analysis with associated randomisation test to mitigate the temperature dependent variation in the local mean level of the monitored received signal power. Through the proposed algorithm, the conventional use of a single baseline level to derive fade values is discarded in favour of the estimated significant local mean levels, which better reflect the measured data.
- Unique results from statistical analysis, and comparison to prevailing measurements, predictions and models, of the measured 42 GHz wideband millimetre-wave signal, within the specific context of long-term precipitation fade, propagation through foliage and spatial correlation of precipitation fade distribution.

## **1.6 Structure of the Thesis**

The organisation and brief description of the thesis on a chapter by chapter basis is as follows:

Chapter 2 details the investigation into equipment integration and calibration tasks involved in the set up of the 42 GHz MWS campus network trial experimental test-bed. Service provision in the form of digital TV feeds and a high-speed Internet protocol (IP) based data network is delivered into the local trial area, and is received by the suitably deployed remote sites. A thorough literature review then follows, focusing on background materials and progress of research work on BFWA, with attention specifically to millimetre-wave propagation and MWS. The review work identified the key areas of long-term precipitation fade, propagation through foliage and spatial distribution of precipitation fade as possible research direction.

Chapter 3 covers the research into, and development of, a cost-effective signal measurement system for measuring the signal parameters of the millimetre-wave radio link. The signal measurement system integrates the use of low cost consumer satellite set-top box (STB) and custom built data acquisition module. Additional development work presented includes a similarly cost-effective meteorological measurement system for monitoring of weather conditions, and a fade simulation system for use in relevant calibration and testing tasks.

Chapter 4 highlights the issues of the temperature dependent variation in the long-term local mean level of the monitored received signal power, and proposes a mitigation technique in the form of the novel use of an iterative cumulative sum analysis with associated randomisation test. Testing of the proposed algorithm on actual measured data indicates a more accurate unbiased derived fade statistic.

Chapter 5 presents a comprehensive statistically based analysis of the data from the long-term field measurement campaign. Verification using measured data from different years and links, shows that the availability prediction model needs further improvement, while the fade duration prediction model gives reliable estimate. Previously unavailable results showing the effect of seasonal and weather variation on the signal propagating through foliage are also given, based on analysis of the measured data that was gathered over 6 months. Other results covered include indication of route diversity improvement using measured data from two moderately spatial distributed radio links.

Finally, Chapter 6 summarises the research work undertaken and defines further possible research directions.

## **Chapter 2**

# **Millimetre-wave Broadband Fixed Radio Access**

A literature review of millimetre-wave broadband fixed wireless access is covered, with the aim of establishing the background and rationale for the research work undertaken. It includes previous trials and measurement campaigns, and specific propagation issues. An overview is also given of the campus network trial which forms the basis for the field measurement campaign of the research.

The literature review establishes that available results lack measurement of; (i) the actual 42 GHz signal, (ii) a wideband signal, and (iii) a long-term time period. Key areas for research direction were also identified to be the specific analysis of long term precipitation fade statistic, propagation through foliage and spatial distribution of precipitation fade.

## **2.1 42 GHz MWS Campus Network Trial Measurement Test-Bed Set Up**

The trial arises from the enabling campus network platform which serves as an experimental test-bed for, the exploration of millimetre-wave propagation, equipment and integration, and broadband application issues at 42 GHz. Within the context of the campus network trial, the measurement campaign aims to undertake long-term statistical studies of the millimetre-wave radio link under a realistic deployment scenario. The investigation includes various aspect of propagation, through foliage blockage and coverage. To facilitate these studies, a suitable 42 GHz MWS with appropriate remote sites was set up.

### **2.1.1 Service Provision**

The aim of a MWS access network is to provide the transparent transport of user services from the core network to the end user. Historically, these services have been broadcast TV and circuit switched telephony, but have since been equalled or even surpassed by the huge growth in demand for broadband data access such as fast Internet [5]. For the campus network trial to be a relevant implementation of a realistic MWS deployment, it needs to provide the basic broadcast and interactive access services. The relevant technology and equipment integrations and set up were thus investigated, with the aim of realising the provision of these services.

#### **Broadcast Service**

In order to enhance the overall value of the broadcast services, which has the added advantages of encouraging and getting trial participants on board, a variety of suitable digital video content sources need to be procured. The broadcast service used in previous trials [8] is comprised of direct-to-home (DTH) satellite digital TV transmission, as it allows off-the-shelf satellite STB to be used at the remote sites for reception of the signal. This DVB satellite (DVB-S) compliant satellite signal is quadrature phase shift keying (QPSK) modulated and encoded with the forward error correction (FEC) concatenation of convolutional and Reed Solomon (RS) codes [17]. For quasi-error-free reception (QEF) of the Motion Picture Expert Group Layer 2 (MPEG-2) transport stream encoded video, the

typical required carrier-to-noise ratio (CNR) (see Section 2.3) at the satellite integrated receiver decoder (IRD) is approximately 6.8 dB [18].

The re-broadcasting schemes utilised in the previously conducted trials cover the three possible approaches of using frequency conversion, DVB-S re-modulation, and re-multiplexing with re-modulation. When only frequency conversion is used, the signal suffers a CNR degradation from off-air reception of 4 to 5 dB, while receiver site measurements showed that the CNR was typically 11 to 12 dB [7]. This limits the dynamic range available for partial LOS measurements such as through foliage, envisaged for the campus network trial measurement campaign.

A suitable alternative, apart from the expensive equipment cost of re-multiplexing, will be to re-broadcast using DVB-S re-modulation. The typical configuration involves using a professional satellite IRD that is connected to a satellite dish, to tune in to a single satellite transponder multiplex. The demodulated and decoded MPEG-2 transport stream (TS) transponder data that is made available on the serial parallel interface (SPI) of the IRD is then fed to a DVB-S modulator prior to re-broadcasting.

However, in terms of TV content, suitable unscrambled TV channels that are available on satellite transmission are fairly limited and also distributed among the different satellite transponders [19]. To make available the different channels will necessitate a separate satellite dish, IRD and DVB-S modulator for each required transponder. More suitable TV channels were found on the digital terrestrial transmission, grouped together into the BBC, ITV/Channel 4 and Channel 5 multiplex [20]. As both transmission schemes adhere to the DVB standard, the common MPEG-2 TS layer [21] should guarantee a seamless interoperability between the terrestrial and satellite TV signals.

A hardware interoperability test was performed to validate this approach. The test involves demodulating the received off-air DVB terrestrial (DVB-T) signal into a MPEG-2 TS which is then delivered to a DVB-S modulator for modulation onto a suitable carrier, as depicted in Figure 2-1. Each of the DVB-T digital TV multiplex signals which is coming in at a rate of 24.13 Mbits/s [22] can be completely retransmitted in a 23.625 MHz wide channel at a DVB-S modulated symbol rate of 17.5 Msymbols/s using the common 3/4 code rate.

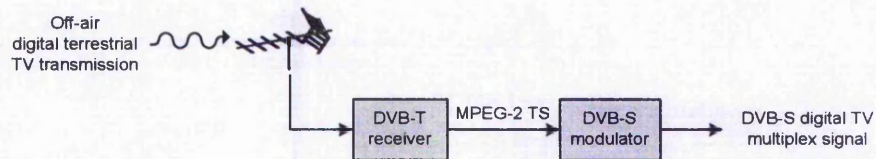


**Figure 2-1: Broadcast service digital video source.**

To test the compatibility of this modulated signal, a suitable consumer satellite STB with manual tuning capability, is used for reception and viewing of the digital TV channels. With the exception of two TV channels on the BBC multiplex, all the others could be viewed correctly, proving the interoperability between the standards. For those channels in question, the entire picture frame was shifted approximately a quarter of a frame to the right, with a resulting black vertical bar running on the left. No plausible explanation could be given and no further enquiry was made as this is beyond the main scope of the campus network trial. Whilst this phenomenon is unexplained, it did not have a significant bearing on the campus network trial since the TV channels affected are available on analogue transmission.

Several professional terrestrial IRDs were evaluated in the interoperability test for extracting the MPEG-2 TS. Having demonstrated the viability of this approach, a cost-effective alternative consisting of a sub-£300 DVB-T front-end module was found to replace the professional terrestrial IRDs, which is an order of magnitude more expensive. This front-end module requires only an external low voltage differential signal (LVDS) level conversion on its MPEG-2 TS output for compatible interface to the SPI input of the DVB-S modulator. Two units of the DVB-T front-end module with the corresponding DVB-S modulator are currently employed to provide two digital TV multiplex video sources, which comprises of the ITV/Channel 4 and Channel 5 multiplex.

### **Interactive Service**

The campus network trial adopts the DVB-RC [23] access technology designed for hybrid fibre coaxial cable (HFC) network to provide interactive service. The rationale behind using cable technologies is that readily available, proven equipment may then be used in a hybrid network employing both cable and radio media with the associated cost benefits. Integration of the cable network equipment to the radio system involves a frequency

translation of the modulated downstream and upstream signal of the cable to the intermediate frequency (IF) interface of the radio network.

The main enabling equipment is the Interactive Network Adapter (INA) from Hughes Network Systems which controls the bidirectional broadband data communication over the HFC network to the connected cable modems. It uses the in-band architecture to carry the interactive data. IP packets are transported bidirectionally in ATM cells that are encapsulated in MPEG-2 TS frames [24]. With QPSK modulation, the 8 MHz downstream data channel offers a raw data rate of 13.8 Mbits/s. This downstream capacity is time division multiplexed between all users. On the upstream return channel, the data is carried over a 2 MHz channel using differential QPSK (DQPSK) modulation. The resulting raw data rate of 3 Mbits/s is shared between users on a time division multiple access basis (TDMA), governed by a user specified fixed rate, reserved or contention access protocol.

System management of the INA is based on the simple network management protocol (SNMP) standard. Apart from the standard management software, the Hewlett-Packard OpenView Network Node Manager software is also used for better administration of the cable network.

Complete networks of PCs emulating a real deployment scenario were set up under the cable network environment to both investigate and resolve any device configuration and internetworking issues. This task has resulted in a stable working data network for porting over to the radio system.

### **2.1.2 MWS Configuration**

Both the broadcast and interactive service technologies are integrated to the 42 GHz radio network, forming the core MWS configuration of the campus network trial. This provides a test-bed from which the field trial measurement campaign can be carried out. Apart from that, the performance of the current system configuration could also be continuously assessed in line with the exploratory aim of the campus network trial into equipment integration issues.

Investigation of the millimetre-wave radio architecture and the overall system configuration of the campus network trial is required if any accurate channel measurement is to be made. Even simple received signal power measurement necessitates knowledge of the transmitter and receiver gain in order to determine the absolute level of the measurement. Other issues which might affect the measurement campaign due to the hardware implementation of the MWS will also need to be accounted for.

### Head-end System Configuration

The base station equipment is separated at an IF interface based on DTH satellite downlink frequency band, into an outdoor unit (ODU) comprising of the millimetre-wave radio transceiver, and an indoor unit (IDU) which consist of signal sources and interfacing equipment. Adoption of this IF interface enables the ODU hardware to be minimised, in addition to ensuring compatibility with various indoor equipment. Figure 2-2 shows the architecture of the ODU 42 GHz millimetre-wave radio transceiver that is provided by the sponsor company, MMRadiolink, for deployment in the campus network trial.

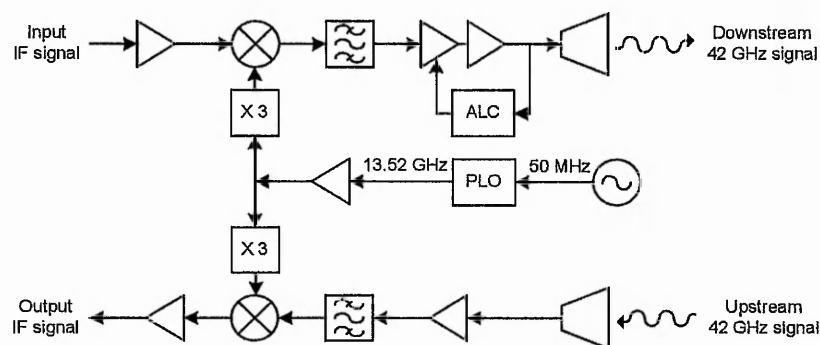
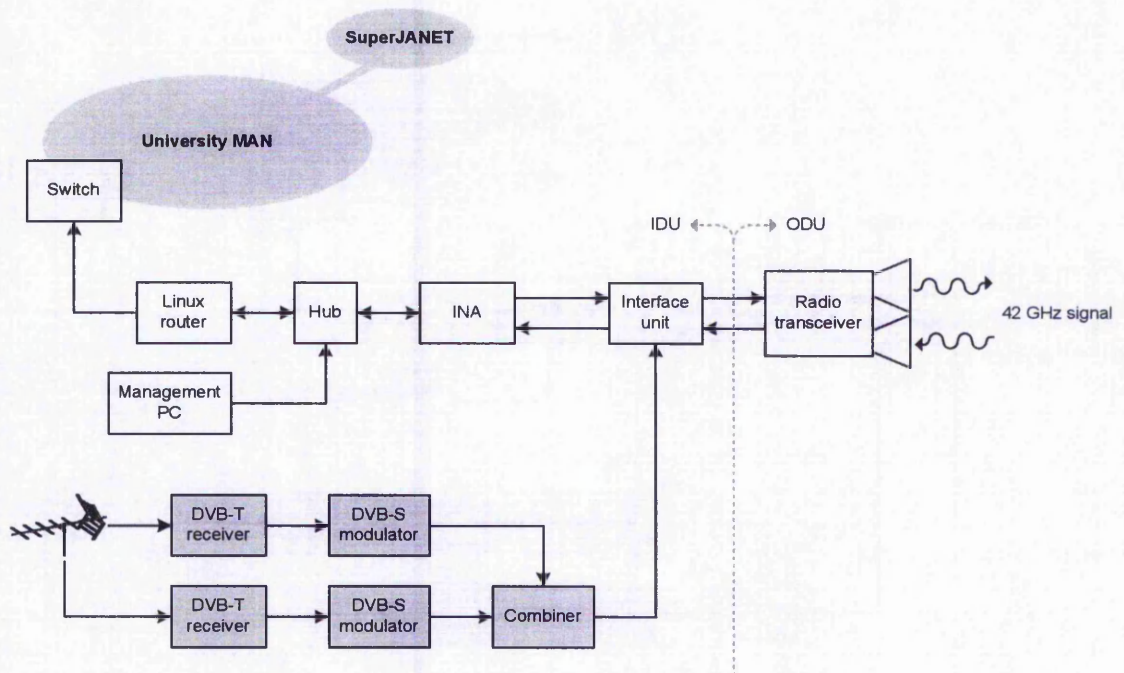


Figure 2-2: Head-end radio transceiver architecture.

The millimetre-wave radio transceiver is essentially a broadband linear up/down-converter and amplifier, converting between the IF and 42 GHz. In order to be tolerant to frequency stability and phase noise issues, the radio transceiver employs a phase locked local oscillator with an ovenised crystal reference. An automatic level control (ALC) module is present on the transmit chain to compensate for temperature dependent gain change while permitting back-off control of the monolithic microwave integrated circuit (MMIC) amplifier power output. Total output power of the head-end radio transceiver was fixed to 16 dBm. This is shared equally among all available downstream channels.

Separation and isolation between the downstream and upstream signals is achieved through spatial duplexing via separate antennas, orthogonal polarisation and bandpass filtering for transmit and receive. The head-end unit uses sectorial horn antennas with a large beamwidth of  $64^\circ$  and gain of 15 dBi.

An overview of the IDU equipment set up for the head-end base station is given in Figure 2-3. The campus network is configured to deliver a broadcast digital TV network and a parallel IP based data network.



**Figure 2-3: Head-end base station network topology.**

To integrate the cable network equipment to the radio system, the lower operating band of the INA is translated to the higher frequency range of the IF interface via an interface unit. As the baseband modulation occurs in the cable modem, the MWS in essence becomes a transparent extension of the cable network. Besides frequency translation, the gain of the interface unit is also configured to ensure that both the data and broadcast signals are at the appropriate IF power level.

A Linux PC router serves as the gateway to the university Metropolitan Area Network (MAN). Access to the Internet is then made possible through the university's SuperJANET broadband data backbone connection.

With the current implementation, the radio network enables extension of the existing university's network to remote sites, with provision of high-speed university Intranet and Internet access, along with broadcast digital TV. The associate frequency and polarisation plan adopted by the campus network trial is as defined in Figure 2-4.

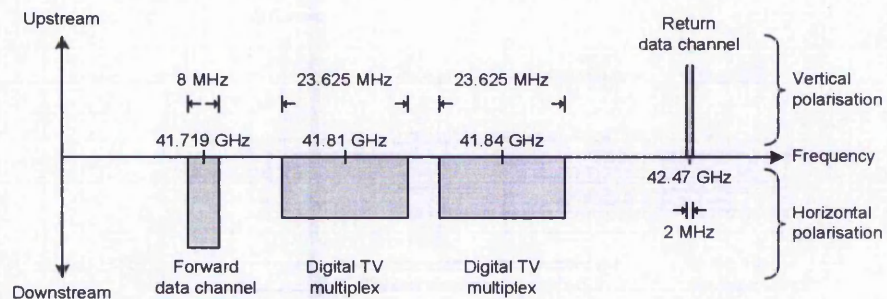


Figure 2-4: Campus network trial frequency and polarisation plan.

Three RF channels are transmitted downstream at 42 GHz using horizontal polarisation. Two of these channels carry the DVB-S re modulated terrestrial digital TV multiplex while the remaining channel is the DVB-C compliant QPSK modulated data stream. The vertical polarised narrowband return data stream forms the only upstream channel.

### User-end System Configuration

The CPE at the user end is similarly separated at the IF level. Figure 2-5 illustrates the user-end radio receiver architecture for broadcast only reception.

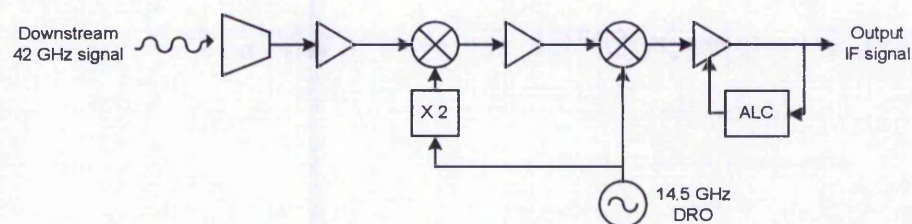
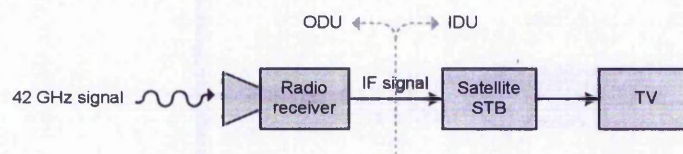


Figure 2-5: User-end broadcast only reception radio receiver architecture.

The millimetre-wave radio receiver ODU comprises an integrated 3° narrow beamwidth horn antenna, and a two-stage downconversion with amplification [25]. To keep the manufacturing cost down, the downconverter uses a low cost dielectric resonant oscillator (DRO) as the local oscillator. An ALC is built-in to limit the dynamic range of the output signal. Output from the radio receiver is in the common DTH satellite reception IF band.

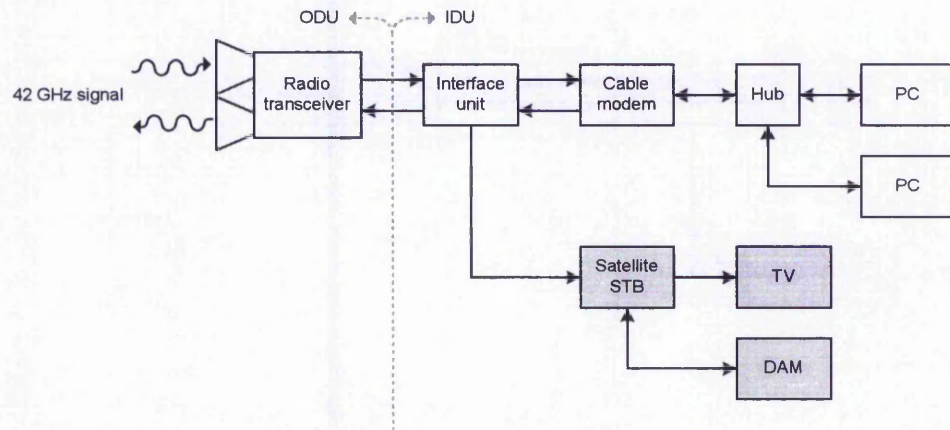
If the radio receiver is to be used for channel measurements of the millimetre-wave transmission, any adverse effect of multipath signal is expected to be slight, due to employment of the narrow beamwidth antenna which causes the majority of multipath component signals to be very heavily attenuated (see Section 2.5.8). However, the combination of low cost volume manufacturing, outdoor mounting and lack of any temperature compensation circuit means that the received IF signal will be susceptible to changes in the ambient temperature. In addition, care must be taken to ensure that the radio receiver is operating in the linear range of the ALC when channel measurements are made with it.

Figure 2-6 depicts the configuration for the receive only system. The IF signals of the broadcast channels are directly fed from the millimetre-wave radio receiver to the satellite STB for viewing on a TV set.



**Figure 2-6: User-end broadcast only reception system set up.**

For two-way links, the user-end millimetre-wave radio transceiver ODU has the same basic structure as the head-end unit shown in Figure 2-2, albeit with a few exceptions. Levelling of the RF output of the radio is achieved by adjusting the input IF signal power as there is no ALC on the transmit chain. In addition, the radio transceiver uses a much narrower 3° beamwidth conical horn antenna with 34 dBi gain. The system configuration for a typical two-way link CPE is given in Figure 2-7.



**Figure 2-7: User-end two-way system set up.**

Frequency translation between the higher IF interface of the radio transceiver and the operating band of the cable modem is again realised by the interface unit, along with the necessary signal power level corrections. The cable modem incorporates a routing function with network address translation (NAT). This enables multiple PCs to be connected in a private network on the cable network side. Apart from two-way IP data channel, the interface unit also filters the broadcast channels for reception by the satellite STB.

### 2.1.3 Radio Subsystem Calibration

Channel measurements of the received IF signal that are made with the millimetre-wave radio receiver and transceiver need to be correlated to the equivalent 42 GHz RF signal for the measurement to be of any use. To achieve this and also ensure a more accurate measurement, the gain response of user-end ODU radios must be determined through calibration. The calibration process will need to take into account the previously defined frequency plan given in Figure 2-4. Of the three downstream channels, the RF signal of interest in the measurement campaign is the upconverted digital terrestrial TV multiplex channel at a carrier frequency of 41.84 GHz

#### User-end Radio Receiver Calibration

Initial calibration of the user-end millimetre-wave radio receiver is done using waveguides in place of the antenna and air interface. A similar 41.84 GHz signal source is fed through a rotary vane attenuator (RVA) and terminates into the receive chain of the radio under test. Output power of the IF signal from this radio receiver is then measured on a spectrum

analyser. By successively attenuating the input RF signal via the RVA, the resulting gain response shown in Figure 2-8 is obtained.

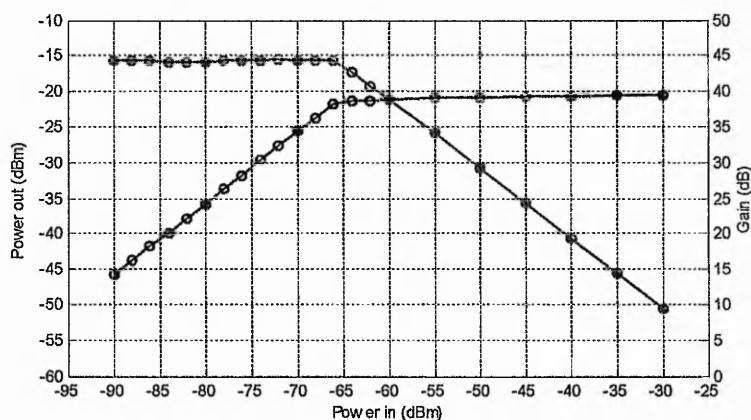


**Figure 2-8: User-end radio receiver chain gain response.**

The gain response indicates a sharp drop in gain when an RF signal larger than -65 dBm is present at the radio receiver. This is characteristic of the sharp activation of the ALC. When operating in the linear region, the gain of the receive chain is 44.2 dB. With knowledge of this gain, the user-end radio receiver is then tested across an actual radio link. By knowing the transmitted power and path loss, and ensuring that the radio receiver is not saturated, the gain of the antenna was determined to be approximately 32.7 dBi. The total gain of the radio receive chain is therefore 76.9 dB.

If the radio receiver is used for channel measurement of the millimetre-wave signal, it must be sited sufficiently far away from the head-end transmitting point to ensure that the received RF signal is not large enough to activate the ALC and bias the measurement. Based on the defined transmission and radio parameters, and assuming an ideal direct LOS radio link, this distance is shown to be approximately 1 km.

### User-end Radio Transceiver Calibration

Using the same calibration process, the gain of the user-end millimetre-wave radio transceiver minus the antenna is found to be 37 dB, as shown in Figure 2-9. The receive chain can be seen to start saturating when the input RF signal is larger than -30 dBm.

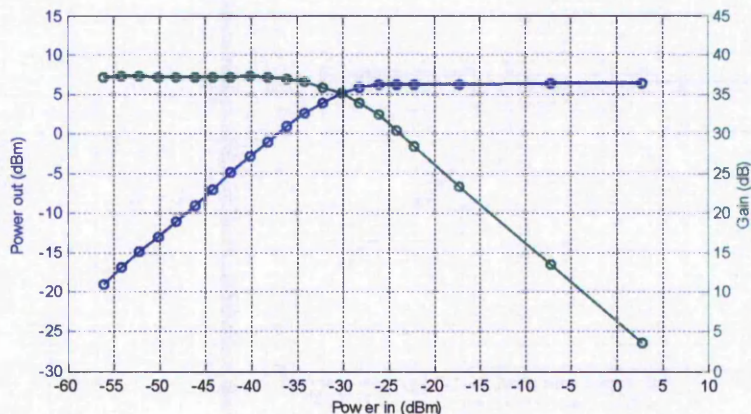


Figure 2-9: User-end radio transceiver receiver chain gain response.

Measurement across a radio interface yields an antenna gain close to 34 dBi, giving a total receiver gain of 71 dB. Similar argument and preventative measure must be taken to ensure that radio transceiver is sited at least 21 m away from the head-end transmitter to ensure that it is operating in its linear region.

#### 2.1.4 Remote Sites Deployment

The campus network trial is sited at the university's city campus in the city centre of Nottingham. A single sector edge-feed MWS cell is provided into the local area by the base station head-end radio transceiver, which is mounted on the rooftop of the university's Newton building. Conducted field site survey has indicated that there are more potentially suitable remote sites towards the North-Eastern segment of the base station. These sites include other university buildings, a halls of residence and individual homes of staff and students. Figure 2-10 shows a photo of this radio transceiver and the local service area.



**Figure 2-10: Photo of the base station millimetre-wave radio transceiver.**

Remote sites for the initial phase of the campus network trial will be selected in order to give locations that are valuable from both a service utilisation and channel measurement perspective. Appropriate remote sites for the latter requirement should ideally consist of spatially diverse distributed remote sites with combination of LOS and through foliage links, as this will maximise the possible type of propagation measurement scenario as encountered in a realistic MWS deployment. Other stipulations for these remote sites are that each must foremost be within coverage of the campus network trial service area, and permit feasible installation and ease of periodic access to the equipment.

### **Campus Network Trial Cell Coverage**

The link budget directly determines the range and deployment pattern possible for the campus network trial [26]. In addition to the parameters already defined by the MWS subsystems, the link budget also needs to account for network availability.

A remote site is considered to be within the area coverage of the campus network trial MWS cell if the received digital TV multiplex IF signal CNR is larger than 6.8 dB, as required by the satellite STB [18]. With knowledge of the transmitted signal, radio parameters and antenna beam pattern, the possible MWS cell coverage can be derived using Equation 2-15 (from later Section 2.5.3). An example of such coverage in terms of

CNR contour plots, assuming the use of millimetre-wave radio receiver for all remote sites and transmission under clear-air condition, is depicted in Figure 2-11. These contour plots illustrates the decrease in CNR with distance, as calculated from the link budget using the stated transmitted output power and frequency plan in Section 2.1.2.

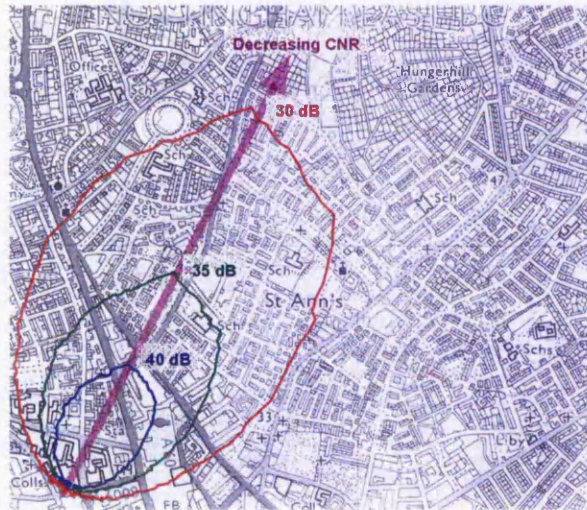


**Figure 2-11: Campus network trial cell coverage.**

### Remote Sites Details

Figure 2-12 illustrates the geometry of millimetre-wave radio links from the chosen and deployed remote sites. Specific details of each link are further tabulated in Table 2-1.

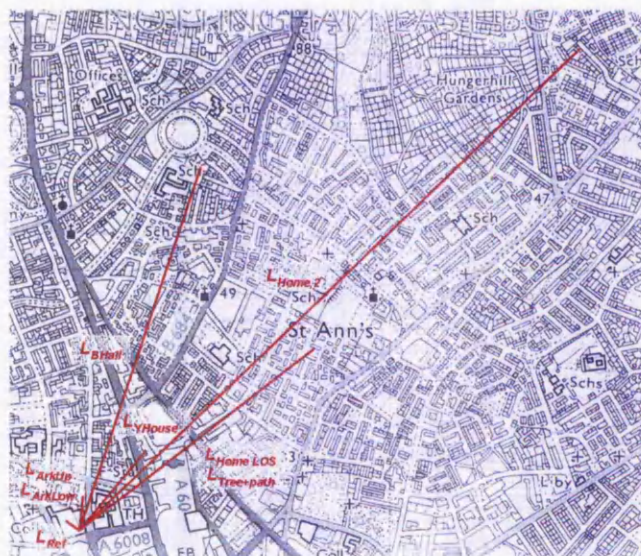


**Figure 2-12: Campus network trial radio links layout.**

Radio link	Location	Radio link type	Path length (km)	Angle wrt North (°)
$L_{BHall}$	Blenheim Halls of Residence	Two-way LOS	1.17	18
$L_{YHouse}$	York House – Dept. of Broad. & Jour.	Two-way LOS	0.26	38
$L_{Home\ LOS}$ $L_{Tree+path}$	Residence house 1	Receive only LOS Receive only thru tree	0.78	51
$L_{Home\ 2}$	Residence house 2	Receive only LOS	1.98	45
$L_{ArkUp}$ $L_{ArkLow}$	Arkwright	Receive only thru tree Receive only thru tree	0.10	5
$L_{Cal}$	Newton rooftop	Receive only LOS	0.06	306

**Table 2-1: Deployed remote sites radio link details.**

Link  $L_{BHall}$  connects the base station to one of the university's halls of residence, which serves as the main demonstration site for the campus network trial. Communal access to the university network, fast Internet and digital TV is provided for students and hall managers via the 42 GHz millimetre-wave radio link. However, this remote site has not been immune to roof-rights and local planning constraints which necessitate the user-end radio transceiver to be installed indoor with transmission through a window. Owing to the excessive path loss introduced by the double-glazed unit, which measured in excess of 20 dB, the window was replaced with a clear perspex layer with negligible loss. As the radio transceiver is located indoors, the measured received IF signal is relatively stable allowing it to be possibly used as reference for comparing with other radio links in the field trial measurement campaign. The second main data access point is located in the Department of Broadcasting and Journalism on link  $L_{YHouse}$ . Due to similar planning restrictions, the radio transceiver is also installed indoors.

The remaining remote sites are broadcast only reception sites. Link  $L_{Home\ LOS}$  and  $L_{Tree+path}$  are two parallel radio links terminating at individual millimetre-wave radio receivers. The former is a clear LOS link while the latter is partial LOS link with propagation through a tree. Each ODU is mounted at the same residence house but spaced horizontally apart, to enable potential correlation between propagation through air and foliage. Link  $L_{ArkUp}$  and  $L_{ArkLow}$  are another set of parallel radio links with propagation through foliage. The ODUs

for these links are mounted onto a lamppost in the compound of Arkwright building with a local vertical separation between them.

A temporary remote site at another residence house, forming link  $L_{Home\ 2}$ , is also deployed to provide a spatial distance complement to the other remote sites. The last remaining remote site is a reference radio link set up on the rooftop of Newton building to facilitate equipment calibrations and experimental measurements using the radio and air interface.

Photos of several of these remote sites are provided in Appendix A.

## 2.2 Trials and Research Work on Millimetre-wave Systems

Over the past several years, a number of trials have been conducted to address some of the issues that may arise within the application of terrestrial millimetre-wave BFWA. One of the major set of trials was undertaken in the Cellular Radio Access for Broadband Services (CRABS) project [27], carried out under the framework of the European Union Advanced Communication Technologies and Services (ACTS) research programme. The project involved a broad combination of operators, research and industrial organisations from several countries. The main objective of the project was to develop and demonstrate a 42 GHz MWS with interactivity [8]. In addition to these trials, the project also involved extensive propagation studies, primary undertaken by project partners in the UK, Norway and Italy [28].

Another group operating under the ACTS program and complementary to the CRABS is CABSINET. The CABSINET project [29] was focused on building a demonstrator to enable performance evaluation of a two layer macro cell and micro cell cellular system, at 40 GHz and 5.8 GHz, for interactive television and supporting both fixed and nomadic terminals. A follow-up and ongoing research programme, EMBRACE, carried out within the IST European Union funded framework, aims to develop a low cost radio access system for the mass market. Secondary to this is the extension of the work done in CRABS which had identified a need for improvement of the return link in the access systems and coverage issue. No significant propagation measurements or trial works are included in this project.

Trials of LMDS systems [13] at the lower frequency band of 28 GHz have also been undertaken by universities. The trial at the University of Madrid was focused on testing prototype radio transceivers and integration of applications, services and management system [30]. At Virginia Tech, the LMDS trial is used to test and demonstrate the suitability of the access technology for providing broadband access to rural areas [31]. Apart from service provision, the trial also enables propagation measurements to be performed.

Studies of millimetre-wave radio systems have also been broadly covered in various research work outside the context of a trial. These includes significant work on different aspects of the millimetre-wave propagation channel fundamental to BFWA, encompassing areas such as effects of meteorological condition and obstruction on the millimetre-wave signal, as shown in the latter sections.

Other related research work in terms of millimetre-wave radio systems, include the investigations of high-altitude platforms (HAPs) as a viable alternative approach to the conventional terrestrial delivery of BFWA [32, 33]. A development project, HeliNet, has focussed on the design of a prototype aeronautic platform operating at 48 GHz and applications for the platform [34]. The succeeding CAPANINA project, under the European Union's Framework VI initiative, is currently looking into the provision of low-cost BFWA services from HAPs [35].

### **2.2.1 Channel Measurements from Trials and Research Work**

Different measurement techniques have been developed to study different aspects of the RF channel. By convention, these techniques are classified as narrowband techniques and wideband techniques. In narrowband techniques, a continuous wave (CW) signal with known power is transmitted, and the received signal power is measured and analysed over space and time. Wideband techniques however, resolve each multipath component and provide time dispersion information of the channel. There are three types of commonly used wideband channel sounding system, namely the direct RF pulse, the vector network analyser (VNA) measurement, and the spread spectrum sliding correlator system (SCS) [37].

Most of the measurements carried out at millimetre-wave propagation tend to be a measurement of the CW signal. More recent measurement campaigns use and measure the channel power of a modulated wideband signal as transmitted by a real radio network, as oppose to the CW signal. Compared to the latter two channel measurement techniques, wideband channel sounding systems are rarely employed due to the complexity, cost and limitation involved [37]. More importantly, concluded field results indicated that the wideband millimetre-wave signal tends to experience flat fading over the bandwidth of interest. This is further compounded by the fact that the MWS system employs a highly directional antenna which significantly reduces multipath issues. More detail explanations for these factors will be covered in the next few subsequent sections.

### 2.3 Propagation and Reception Fundamentals

In any wireless system, the received signal must exceed the receiver noise floor by a minimum carrier-to-noise ratio in order for the receiver to correctly detect the transmitted information [36]. The fundamental concepts of radio wave propagation and reception are introduced with the aim of determining the basic expression for CNR, and in preparation for the forthcoming discussions.

#### 2.3.1 Path Loss Model

Channel induced attenuation is characterised by path loss, which is the difference of transmitted power and received power calibrating out system and antenna gains. The power attenuation in free space is given by *Friis free space path loss*,  $L_{path}$ , as [37]

$$L_{path} = 20 \log \left( \frac{4\pi d}{\lambda} \right) \quad (\text{dB}) \quad 2-1$$

where  $d$  is the separation between transmitter and receiver and  $\lambda$  is the wavelength.

Equation 2-1 is valid only for distances that are in the far-field or *Fraunhofer region* of the transmitter antenna. The far-field distance,  $d_{ff}$ , is the region that satisfies the following [12]

$$d_{ff} = \frac{2D^2}{\lambda} \quad (\text{m}) \quad 2-2$$

where  $D$  is the maximum aperture area of the antenna. For a 42 GHz radio transceiver with a 90 mm diameter antenna, as employed in the campus network trial, the far-field region is approximately 2 m.

### 2.3.2 Link Budget

The link budget allows the determination of possible coverage for a wireless system given a target CNR. Derivation for the link budget begins with evaluating the received signal power,  $P_r$ , which is given as [12]

$$P_r = P_t + G_t + G_r - L_{path} \quad (\text{dBm}) \quad 2-3$$

where  $P_t$  is the transmitted power,  $G_t$  and  $G_r$  are the transmitter and receiver gains respectively, and  $L_{path}$  evaluated as in Equation 2-1.

The noise power of the receiver, denoted as  $N$ , is determined by the effective receiver noise temperature and receiver bandwidth as [12]

$$N = 10 \log(kTB) \quad (\text{dBm}) \quad 2-4$$

where  $k$  is the Boltzmann constant,  $T$  is the effective noise temperature of the receiver and  $B$  is the receiver bandwidth. Since both received signal power and noise power is known, the CNR can thus be evaluated as follow

$$CNR = P_r - N \quad (\text{dB}) \quad 2-5$$

At millimetre-wave frequencies, the coverage area for a system employing an antenna of a certain fixed gain is much reduced due to the increased free space path loss that scales with frequency. By manipulating Equation 2-5, the possible transmission distances for a given CNR and vice-versa, can be ascertained.

## 2.4 Terrestrial Millimetre-Wave Propagation

In order to provide the same system performance as a wired system, quantitative knowledge of the millimetre-wave channel is essential. The following sections present a detailed review on the fundamental propagation mechanisms relevant to terrestrial millimetre-wave channels and available channel measurements. Some results at microwave frequencies are also included for comparison purposes.

### 2.4.1 Refraction - Refractive Index Change

Variation in the climatic conditions such as temperature, pressure and humidity will cause changes in the refractive index of the air. Consequently, electromagnetic waves may arrive at the receiver antenna along slightly different paths. When these discrete multipath components are refracted to the receiver by the layered atmosphere, the received LOS signal will suffer frequency selective fading [38]. The probability of occurrence becomes smaller with shorter path lengths, but larger with higher frequencies [36].

### 2.4.2 Reflection - Rough Surface

When an electromagnetic wave impinges on a surface of finite conductivity, part of the energy is reflected back and part of the energy is transmitted into the surface. If the reflecting surface is smooth, the reflected wave and transmitted wave are related to the incident wave by reflection and transmission coefficients given by *Snell's law*. However, when the surface is made progressively rougher, the reflected wave becomes scattered from a large number of positions on the surface, broadening the scattered energy [36]. Figure 2-13 qualitatively shows the effect of surface roughness on the reflected wave.

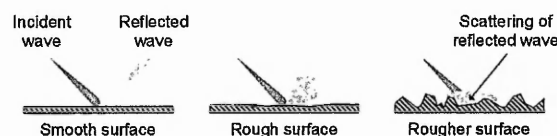


Figure 2-13: Rough surface scattering.

Surface roughness can be described using the *Rayleigh criterion*, which consider a surface rough if [36]

$$h > \frac{\lambda}{8 \cos \theta} \quad (\text{m}) \quad 2-6$$

where  $h$  the is surface height difference,  $\lambda$  the is wavelength and  $\theta$  is the incident angle. Although the Rayleigh criterion is based on a simplified surface scattering scenario, it predicts the basic trends of rough surface scattering, whereby the given surface becomes rougher when the frequency increases or the incident angle decreases.

Due to the random nature of the surface profiles, characterisation of the surface roughness is a complicated problem and still remained unsolved. Both a rigorous theoretical approach [39] and numerical method [40] has been developed to try to solve the rough surface scattering calculations.

Measurements of reflected and scattered signals were made on a variety of surfaces at normal incidence by Violette [41]. The results show an apparent reduction of the reflected power with the increase of frequency from 9.6 GHz to 28.8 GHz and 57.6 GHz. Langen presented reflection measurement at 60 GHz [42] where reflection loss at various angles was measured. As the incident angle increases, the measured reflection loss decreases. The result also indicates that when the standard deviation of the surface height is equal to or greater than 0.3 mm or over 6 % of the wavelength at 60 GHz, the rough surface structure has distinct influence on the reflection loss.

### 2.4.3 Diffraction - Fresnel Zone Clearance

Diffraction describes the phenomenon of radio waves propagating around obstacles such as buildings, hills and terrain, into a shadowed region. Diffraction can be explained by *Huygen's principle* which states that each point on a wavefront can be considered as a source of a secondary wavelet, and these wavelets combine to produce a new wavefront in the direction of propagation [36].

Figure 2-14 shows how plane wavefronts impinging on the edge of an absorbent plane (knife-edge) will curve, filling in the shadowed region with diffracted rays and results in a reduction of the received field strength.

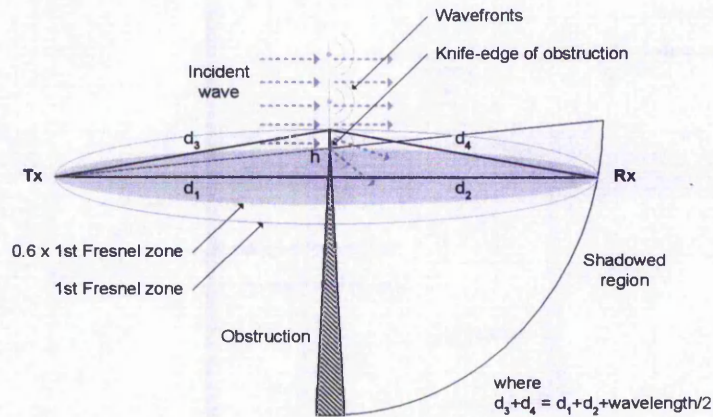


Figure 2-14: Knife-edge diffraction.

The geometry shown in Figure 2-14 also illustrates knife-edge diffraction in terms of obstruction of the *Fresnel zone* around the direct ray. In addition to LOS clearance, any diffraction loss can be avoided if the obstruction does not occupy anywhere within 60 % of the first Fresnel zone clearance [43].

#### 2.4.4 Attenuation and Scattering - Effects of Vegetation

At millimetre-wave frequencies, foliage appears as a medium of random discrete, lossy scatterers due to the haphazardly oriented scattering surfaces and much larger dimension of the foliage leaves relative to the propagating wavelength. Such propagation is characterised by attenuation, beam broadening and depolarisation [44, 45, 46]. The two common approaches applied to study and treat the penetration of the millimetre-wave signal in foliage are by analytical or numerical electromagnetic modelling [47, 48, 49, 50, 51], or by measurement based empirical models [52, 53, 54, 55].

The theoretical description of the propagation of the radiowave signals through the vegetative medium is given by the fundamental *theory of radiative energy transfer* [56]. Based on this transport theory, *Schwering* [44] developed an important hypothesis to explain the results of a conducted comprehensive measurement campaign on microwave

and millimetre-wave propagation in woods and forests, which becomes the basis for many subsequent modelling works.

The deterministic approach of the proposed hypothesis provides information on the field propagated through, and scattered from the foliage. It models the foliage environment as a statistical homogeneous medium of lossy random scatterers whose scatter pattern is assumed to consist of a strong narrow forward lobe superimposed over an isotropic background. A millimetre-wave signal penetrating into this foliage medium is treated in terms of a reduced coherent component of the field due to absorption and scatter of the incident wave by foliage, and an incoherent component due to the scattered wave.

Therefore, the total field intensity in the foliage half plane,  $I_{total}$ , can be defined as consisting of the reduced incident intensity,  $I_{ri}$ , and the diffused intensity,  $I_d$ . The latter term can be further split into forward and back scattered field intensity,  $I_{fs}$  and  $I_{bs}$ , respectively [44], giving the following relation

$$I_{total} = I_{ri} + I_{fs} + I_{bs} \quad 2-7$$

At short distances, the coherent field component,  $I_{ri}$  dominates and decreases exponentially due to absorption and scattering, whereas the incoherent field component,  $I_d$ , increases linearly at short distances, and then decreases exponentially at large distances. Of the two incoherent field components,  $I_{fs}$  is dominant at the intermediate distances while  $I_{bs}$ , with the smallest magnitude and attenuation rate, dominates at large distances. While the original hypothesis is restricted to infinite foliage layers and first-order multiple scattering contributions, recent works have since expanded to the calculation of attenuation for finite isolated foliage such as single trees or bushes [57], and also enables consideration of the influence of actual vegetation volume, cross polarization and beam broadening on the propagation properties [58].

The measurement campaign performed by *Schwering* involved taking CW measurements at 9.6 GHz, 28.8 GHz and 57.6 GHz, over a path length of 0.1 to 0.9 km with 1 to 35 trees on the path [44]. Measurements were repeated under both in-leaf and out-of-leaf conditions.

Curves of the received signal power showed that the range dependence or depth of millimetre-wave signals in foliage is not determined by a simple exponential decrease in signal strength at constant attenuation rate, but by a rapid attenuation rate at short distance into the foliage that transforms into a much reduced attenuation rate at larger foliage depth. Following the transition in attenuation rate, significant beam broadening and depolarisation occurs. These results are well explained by Equation 2-7 [44, 47], in terms of the interplay of the coherent and incoherent field components. For the study of frequency dependence, measurements at the two higher millimetre-wave frequencies indicate a much higher loss than at 9.6 GHz, with the loss at 28.8 GHz and 57.6 GHz being almost the same.

Implementation of the proposed deterministic model for propagation through foliage may be overcomplicated when the aim is to merely estimate the extent of attenuation on a known path. The model requires a precise knowledge of the geometry of the foliage boundaries in relation to the transmitter and receiver, and also of the scattering and absorption cross-sections and scattering profile of the foliage medium. Furthermore, the values for these parameters are obtained by comparison to measured data, and are therefore empirically fitted parameters, albeit more physically descriptive. In such scenario, a simpler empirical model may be more appropriate.

Through tree measurements by *Seville* at 38 GHz [59, 53], and at 11.2 GHz and 20 GHz [54] also shows a dual mechanisms of propagation through the foliage, as seen at the other frequencies and predicted by the *radiative energy transfer* theory. The gradient of rapid attenuation becomes shallower as the foliage depth increases, as scatter from tree to tree becomes a significant mode of propagation which contributes to the received signal, and therefore reduces effective attenuation. Furthermore, the back scattered field was found to have higher value with greater fluctuation at the tree trunk than at the canopy level.

By taking account of the measurement site geometry and optimising parameters based on the available experimentally measured data from 9.6 GHz to 57.6 GHz, a semi-empirical dual gradient (DG) model was developed. This has since been adopted as the prevailing prediction model in ITU-R P.833-3 [60], for millimetre-wave signal attenuation in foliage.

Other field measurement at 38 GHz [61, 62] indicate that the attenuation resulting from dry foliage obscuring the first Fresnel zone of a point-to-point link can account for 1-2.9 dB/m for a variety of deciduous trees. The degree of attenuation increases to 2.5-7 dB/m for the same foliage when wet.

#### 2.4.5 Attenuation and Scattering - Effects of Precipitation

Millimetre-waves suffer attenuation when propagating through precipitation due to absorption and scattering process by the raindrop particle. In particular, the scattering process is strongly frequency dependent, since wavelengths which are short relative to the raindrop size will be greatly scattered. The attenuation effects of precipitation on radio wave propagation have been studied extensively, and the most fundamental rain attenuation model are those that are presented by Olsen [63] and Crane [64]. More rigorous theoretical treatments of rain scattering have also been undertaken [65, 66].

Rain can be modelled as a random medium of sparsely distributed scatterers [64]. The specific attenuation,  $\gamma_R$ , is summarised as follow

$$\gamma_R = 10^4 \log_e \int_0^{D_{\max}} Q(D)N(D)dD \quad (\text{dB/km}) \quad 2-8$$

where  $Q(D)$  is the effective attenuation cross-section of a raindrop and  $N(D)$  is the number of raindrops of diameter  $D$ .

Detailed theoretical and numerical analysis of the effect of precipitation is given by Olsen [63] via applying a *Mie scattering* calculation to obtain  $Q(D)$ , and for different drop size distribution. General precipitation attenuation is derived theoretically and simplified by an exponential relationship as

$$\gamma_R = aR^b \quad (\text{dB/km}) \quad 2-9$$

where  $a$  and  $b$  are functions of frequency and polarisation, and  $R$  is the point rainfall rate in mm/h.

The precipitation attenuation model investigated by Crane [67] takes into account the variation of rain rates along a horizontal path. The path averaged rain rate is calculated based on the point rainfall rate. The proposed theoretical model is similarly based on the  $aR^b$  precipitation attenuation model but with empirically derived multipliers.

## 2.5 42 GHz MWS Specific Issues

Issues which impede the terrestrial millimetre-wave propagation channel will need to be taken into account in the deployment and operation of a MWS network. However, the very nature of using the millimetre-wave signal as a point-to-multipoint transport medium within the MWS that is providing services, introduces further potential complications which need to be analysed, so that statistical procedures and site-specific methods can be developed to predict or even mitigate any problem that arises.

In the context of a point-to-multipoint area coverage, there is a need to distinguish the single radio link to a particular user, and all the associated radio links to a given number of users in the service area. The signal carried by the radio link will also need to be considered, as it is a digitally modulated wideband signal, typically several tens of MHz wide. The significant of these two aspects comes into play when investigations are carried out on blockage conditions and propagation effects, which influence the area coverage. Probable scenarios include obstruction of certain area by buildings, foliage and terrains, and precipitation showers that are horizontally localised.

### 2.5.1 Effect of Blockage – Area Coverage

To obtain an insight on the problems of coverage at 42 GHz due to building and foliage effects, a comprehensive measurement campaign was made conducted in Oxford [28]. The signal from a 18 m high transmitter was recorded at over 130 locations using a receiver at a fix height of 8 m.

For any given distance range from the transmitter, the received signal values were found to be spread randomly between the expected free space level down to the system noise level. This is due to blockage by buildings or trees along the path to each receive position, indicating a strong dependence of the received signal on the specific local environment of

the receiver. The total coverage in terms of sufficient margin for reception of services was 63 %, while the measurements showed that approximately 25 % of the locations were obstructed by trees. These measured values of coverage and tree blockage are comparable with the extensive raytracing simulation performed on the 3D database of Oxford [28].

An independent coverage measurement at 28 GHz was also carried out in the urban area of Brooklyn [68]. Measurements were made at 77 different locations within 6 km of the transmitter that was sited at a height of 95 m. For a receiver height of 11.3 m, the coverage was found to be 68 %. A similar random signal spread highlighted by the measurements from Oxford were also apparent in the recorded data.

### 2.5.2 Effect of Precipitation - Availability Predictions

MWS access network availability is based on the yearly CNR statistics as determined by radio events. There are several radio propagation phenomena contributing to a reduction of the nominal CNR. By far the most important one in terms of reduced signal level is precipitation attenuation [28].

The estimate of average annual outage due to precipitation attenuation is determined from long-term statistics of local annual rainfall rates [69]. ITU-R Recommendations contain well established procedures for predicting the attenuation due to precipitation. According to the current prediction method in ITU-R P.530-9 [43], the rain attenuation  $A_{rain}$  for a given effective path length  $d_{eff}$ , radio frequency, polarisation, rain climate and availability required, is given by

$$A_{rain} = \gamma_{rain} \cdot d_{eff} \quad (\text{dB}) \quad 2-10$$

where  $\gamma_{rain}$  is the specific attenuation which can be obtained using ITU-R P.838-1 [70].

Since rainfall rate is not uniform along the path length,  $d$ , a path length reduction factor,  $r$ , is introduced such that the effective length,  $d_{eff}$ , is given by

$$d_{\text{eff}} = d \cdot r = \frac{d}{1 + \frac{d}{35e^{-0.015R_{0.01}}}} \quad (\text{km}) \quad 2-11$$

where  $R_{0.01}$  is the rainfall rate for 0.01 % of time of the average year. While regional rain rate information is available and tabulated in ITU-R 837-3 [71], the use of local rainfall rate is preferred.

The attenuation exceeded,  $A_p$ , for percentage of time,  $p$ , in the range of 0.001 % to 1 % may then be deduced from the attenuation at 0.01 % of time,  $A_{0.01}$ , via the following power law [43]

$$A_p = 0.12p^{-(0.546+0.043\log p)} \cdot A_{0.01} \quad (\text{dB}) \quad 2-12$$

Comparison between rain radar observations at Chilbolton and predictions from ITU-R, however, suggested that the path reduction factor should account for the observed dependence between rain cell structure and rainfall rate [72, 73]. A new path reduction factor which yields better agreement with measured cumulative distribution of precipitation attenuation statistics has been proposed, and is given by the minimum of the following expression

$$r = 1.35 + (2d^{-0.053} - 2.25)\log R(t) \quad \text{and} \quad r = 1 \quad 2-13$$

where  $R(t)$  is the rainfall rate at the percentage time of interest.

Measurements of signal strength at 40 GHz have been made on fixed radio links in Norway [28]. The paths were configured as a 6-link star network, with paths ranging from 0.5 to 6 km. The time exceedance statistic for precipitation attenuation for one year of propagation data was tabulated along with the ITU-R prediction models. The statistics agree well for lower fade depth on the longer links, but the measured attenuation was found to be more severe the longer the links are.

Another factor in accessing availability currently not addressed in the ITU-R Recommendations, is information on the distribution of outages due to rain attenuation, in terms of the durations of fading events. An empirical log-normal model for rain fade durations was also developed from statistics of the duration of point rainfall rates and analysis of fade durations of a 38 GHz link over a 9 km path [73, 74]. This model is based on the rainfall rate  $R$  (mm/h) which gives rise to a given attenuation, and make use of the RAL model for the path reduction factor from Equation 2-13. The number of fades,  $N$ , of depth  $A$  dB with durations  $t_d$  can be found from the following empirically determined expression

$$N = 1.7 \cdot 10^4 R^{-1.76} e^{\left\{ \frac{[\ln(273R^{-0.89} + (0.166 + 0.0194R)t_d - 2)]^2}{3.86 - 0.0409R} \right\}} \quad 2-14$$

### 2.5.3 Effect of Precipitation - Link Availability

For a given path length and with the other link parameters specified, Equation 2-5 can be expanded to yield the maximum CNR as a function of unavailability for a MWS. The general expression for the MWS CNR is defined by the following relationship

$$CNR = P_t + G_t + G_r - F_r - N - L_{path} - A_{gas} - A_{rain} \quad (\text{dB}) \quad 2-15$$

where	$P_t$	transmitter power	(dBm)
	$G_t$	transmitter antenna gain	(dBi)
	$G_r$	receiver antenna gain	(dBi)
	$F_r$	receiver radio subsystem noise figure	(dB)
	$N$	noise power received from the external environment by the receiver antenna	(dBm)
	$L_{path}$	free space path loss	(dB)
	$A_{gas}$	gaseous attenuation due to dry air and water vapour over $d$	(dB)
	$A_{rain}$	attenuation due to rain over $d$ , for unavailability $p$ % of time	(dB)
	$d$	path length	(km)

For a path length of  $d$ , the gaseous attenuation due to absorption by oxygen and water vapour which is always present, is given by

$$A_{gas} = \gamma_{gas} \cdot d \quad (\text{dB}) \quad 2-16$$

The specific attenuation  $\gamma_{gas}$ , can be obtained using ITU-R P.676 [75].

To counteract the signal attenuation due to precipitation, a power margin corresponding to the predicted maximum rain attenuation is engineered into the radio subsystems. Consequently, the network availability is determined by the time percentage corresponding to the maximum rain attenuation given by the added margin.

#### 2.5.4 Effect of Precipitation - Diversity

In a practical MWS, the severe attenuation on longer radio paths due to precipitation is unlikely to be compensated for by available fade margin alone. A possible mitigation technique to increase the potential availability of the system is through the use of site diversity. The use of two separate links to lessen the effect of precipitation attenuation by taking into account the inhomogeneous nature of precipitation, was first proposed by Hogg [76].

Precipitation varies considerably in time and in space both vertically and horizontally. Since the spatial distribution of rain cells depends on their temporal resolution such that convective events are localised whereas stratiform events are wide-spread [28], the attenuation statistics for each radio path of a remote site which have access to two diverse links will be different.

Studies of the spatial and temporal variation of precipitation usually involve using rain gauge networks [77] or radar measurements [78, 79]. These studies provide valuable information on structures inside the rain fields, such as the size, shape and orientation of rain cells. Rain cell modelling via radar indicates that vast majority of rain cells are less than 1 km<sup>2</sup> and that more of the smaller cells occur for greater rain rate thresholds. It also appears that rain cells are shaped by the prevailing wind direction [78].

Diversity improvements were demonstrated for a simulated 20 GHz slant path attenuation based on a dense network of rain gauge measurements for a year [77]. These compared well with the path angle diversity gain and diversity improvement results derived from rain radar measurements of the three-dimensional spatial structure of rain [79]. The results also illustrate that a typical remote site with two-way diversity on a path length of 4 km could maintain the same availability of 99.9 % with 4 dB less margin. Further simulations at 42 GHz show that the diversity has a dependence given as

$$\left[ \sin\left(\frac{\theta}{2}\right) \right]^x \quad 2-17$$

where  $\theta$  is the angular separation between two route diversity links which a remote site have access to, and  $x$  is a function of the link length ratio,  $L_{max}/L_{min}$ . For links of similar length, the optimum value for the coefficients of  $x$  for diversity gain plots,  $x_g$ , and diversity improvement plots,  $x_i$ , are found to be 0.55 and 0.8 respectively. In the event of links having different lengths, the following is applicable

$$\begin{aligned} x_g &= 0.61 \cdot \ln\left(\frac{L_{max}}{L_{min}}\right) + 0.84 & \text{for } 1 \leq \left(\frac{L_{max}}{L_{min}}\right) \leq 2 \\ x_i &= 0.87 \cdot \ln\left(\frac{L_{max}}{L_{min}}\right) + 0.55 & \text{for } 1 \leq \left(\frac{L_{max}}{L_{min}}\right) \leq 2 \end{aligned} \quad 2-18$$

The derived precipitation attenuation of a one year measured data from a 40 GHz star-network links in Norway [28] similarly indicates statistical diversity improvement.

### 2.5.5 Effect of Foliage – Attenuation Prediction

A reliable model for predicting the extent of attenuation due to foliage is important for situation where the system margin following propagation through a single tree, is still sufficient for service provision. The DG model [54] gives the attenuation through vegetation as a function of vegetation depth, by incorporating the dual slope nature of the measured attenuation versus depth curves. This model also accounts for the site geometry in the form of the illumination of the foliage medium, defined by the illumination width,  $W$ .

The attenuation for a given foliage depth,  $d$ , is given by

$$A = \frac{R_{\infty}}{f^a W^b} d + \frac{k}{W^c} \left( 1 - \exp \left( -\frac{(R_0 - R_{\infty}) W^c}{k} d \right) \right) \quad (\text{dB}) \quad 2-19$$

where the initial and final attenuation slope are respectively

$$R_0 = af \quad \text{and} \quad R_{\infty} = \frac{b}{f^c} \quad 2-20$$

with  $f$  as the signal frequency, and constants  $a$ ,  $b$ ,  $c$ ,  $k$ , tabulated for in-leaf and out-of-leaf conditions [54].

The applicability of this model is further validated by measurement undertaken in Norway to determine the attenuation of an actual modulated digital video signal at 42 GHz signal as the receiver is lowered from LOS at treetop height to heights behind the tree [28]. Comparison of the measured attenuation at each height range which varies the foliage depth, with the prediction of the DG model shows reasonable agreement. As the receiver is lowered, the foliage depth encountered will tend to thicken from the top to the bottom. The corresponding measured attenuation increases and then flattens out as the foliage becomes sufficiently thick. This general trend is adhered by all the measurements at the various observation sites and correlates well with the prediction model. As the attenuation becomes almost constant, certain sites close to the transmitter showed that the received signal strength is adequate to provide a service.

### 2.5.6 Effect of Foliage - Variation in Fade

Millimetre-wave signal propagating through foliage exhibits attenuation characteristics that vary with time. The fade that occurs is likely to be due to the phasing of components from different scatterers within the foliage that changes radically as leaves and branches move with wind. Studies and measurements have been made for these short term fades, to give a statistical account of the signal variability over these timescales [46, 55, 80, 81].

Time variability in signals through foliage is quantified in measurements surveying two suburban areas, with depolarisation caused by foliage found to be much greater than that induced by precipitation [46].

To quantitatively evaluate this time variability, a simulated swaying tree in wind was set up using foliated twigs and an electric fan in an anechoic chamber [55]. Measurements at 29.5 GHz indicate that the fading depth and variation scales with velocity of the wind, and is also dependent on the direction and foliage density. Depolarisation was also found to be significant. The fade was established to be 15 dB more compared to similar measurement at 5 GHz.

A comprehensive study comparing the various temporal characteristics of radio channels covering the broad range of 2.45, 5.25, 29 and 60 GHz, in various foliage and wind conditions has been carried out [81]. Measurements were made on a CW signal propagating through deciduous trees when in-leaf and out-of-leaf, and coniferous trees, along with the local wind speed.

Statistical analyses of the measurement results depict a strong frequency and wind speed dependent for the signal when propagating through trees. The amount of attenuation is larger when the size of the obstruction in the foliage, whether leaves or branches, are comparable in size to the wavelength of the particular signal. In the plotted exceedance curves, the 5.25 GHz signal is the most attenuated for the in-leaf deciduous trees while the 39 GHz signal exhibits more loss in the coniferous trees, but the variability is more significant for the largest two frequencies. The studies found the lognormal distribution to be the best representation of the temporal signal variations.

The possibility of service provision through the varying foliage medium has been shown through the reception of a 42 GHz modulated digital video behind a tree. A potential mitigation and improvement method in terms of local spatial diversity has also been demonstrated [82].

### 2.5.7 Effect of Foliage – Flat Fading

Although the deep fading associated with foliage attenuation is intrinsically caused by phase cancellations due to the multiple scatter, the frequency selectivity is shown to be small and hence flat across a typical MWS transmission channel [28]. Measurement work undertaken using a filterbank with a 34 MHz wide channel transmitted through a single tree under simulated windy conditions showed a small fading level of 1.5 dB across the channel, suggesting that there is no significant frequency selective fading. The filterbank measurements confirmed that the rapid time variability present in the broadband channel was also seen in each of the narrowband filter channels. Simultaneous measurements of fade depth and reception of digital video also showed that the picture only failed when the signal level dropped below the system margin.

Flat fading was further demonstrated by wideband measurements conducted at 26 GHz on several radio links through different foliage density [83]. The measurement results indicate that while the level of attenuation changes with foliage depth, the effect of any delay spread measured is negligible.

### 2.5.8 Effect of Buildings and Terrain - Multipath

Multipath effects occur when the received signal consists of a number of contributing signals that have travelled different path lengths. In a typical propagation environment, the millimetre-wave signal could potentially traverse different paths as a result of scattering, reflection or diffraction. Figure 2-15 illustrates the possible propagation mechanism that leads to multipath propagation.

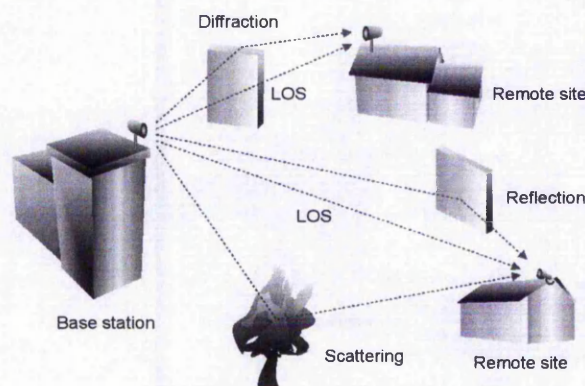
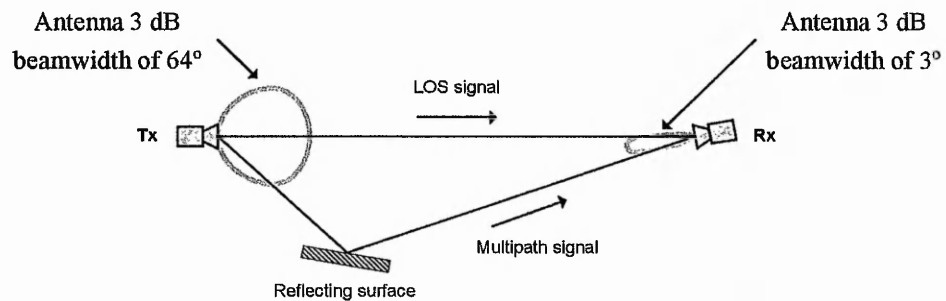


Figure 2-15: Potential sources of multipath propagation.

Due to the highly asymmetric radiation pattern of a typical head-end transmitter antenna, (which has a typical 3 dB beamwidth of  $64^\circ$  in the horizontal plane as opposed to  $10^\circ$  in the vertical plane) multipath reflections from vertical surfaces, such as from buildings, are likely to be the largest problem. A simple example of received signal consisting of a direct LOS signal and one reflected signal, is illustrated in Figure 2-16.



**Figure 2-16: Geometry for a two path channel due to reflection.**

Heuristic analysis of the scenario shown in Figure 2-16 [28] concluded that the reflecting surface must be sufficiently large and properly oriented in order to reflect directly into the narrow beamwidth antenna of the radio receiver. However, for the majority of receiver locations, this will probably not be the case even in an urban environment, due to the fact that buildings tend not to be randomly oriented, thus decreasing the chances of a suitable reflecting angle.

If a multipath signal is received, the resulting millimetre-wave channel transfer function may cause considerable distortion to the information signal. Extensive studies of building reflections and multipath have been carried out via measurement [84, 85], empirical modelling [86] and raytrace simulation [28].

Measurements at 28 GHz and 42 GHz in a realistic urban deployment scenario indicates the present of multipath components [84, 85, 28], that were obtained by looking at reflected signals received from all directions. However, virtually all of multipath signals are expected to be severely attenuated due to the use of receiver antennas with very narrow beamwidth employed at the user sites.

When an adequate LOS signal was available to provide a service, the ripple across a 100 MHz channel was found to be generally small [28]. The ripple is less than 6 dB for 95 % of locations, most of which can be attributed to time variability of the channel rather than multipath. Depolarisation by building reflections and scatter was determined to be relatively unimportant. Raytrace simulation on a 3 dimensional database of Oxford, also predicted that the delay spread values will be insignificant such that it will be of no consequence for service provision at 42 GHz, due to the use of highly directive user-end antenna.

## 2.6 Research Directions

The literature review has primarily focused on the background materials and progress of research work associated with millimetre-wave BFWA, with attention specifically to 42 GHz MWS and millimetre-wave propagation in general. At the current time, the studies of MWS and the associated millimetric transport medium is by no means complete, particularly when it comes to the available statistical information on long-term system performance.

Nearly all of the research work highlighted in the literature review tends to be based on measurements that were conducted for a relatively short duration. Apart from the few measurement campaigns carried out under the CRABS trial, data for long-term measurement is not readily available. The significance of long-term measurements is manifold. Firstly, results from long-term measurement are the best form of data to enable accurate modelling and prediction of the investigated scenario, as it accounts for all possible weather anomalies that will be experienced by a real link. Secondly, it potentially averages out any irregularity that could be present during the time of measurement.

Outside the context of long-term measurement, specific data for millimetre-wave signals at 42 GHz is also uncommon. The general trend seems to be to either imply the 42 GHz data from results at nearby millimetre-wave frequencies, or derive it, directly or with frequency scaling via other means such as rainfall rate measurements. Additionally, most research work has treated the investigation as a point-to-point link using narrowband CW signal as the transmission source.

The field measurement campaign undertaken in this work aimed to address all these shortcomings, whilst maintaining a live 42 GHz MWS network which is providing services.

No adequate comparison of actual measured 42 GHz signal is made with the prevailing availability prediction model recommended by ITU-R. This exercise is necessary in order to validate or improve the prediction model. Measurements spanning several years would permit statistically valid data to be obtained.

In a typical MWS deployment, blockage due to foliage is inevitable. To facilitate service provision through such a link when the system margin is adequate, a better understanding of the long-term performance of such transmission needs to be sought. At present, there is no published long-term measurement result for the propagation of 42 GHz wideband signal through foliage. A large matrix of environmental combinations needs to be considered when making the measurement. These include the transition from in-leaf to out-of-leaf with changes in season, the effect of wetness due to precipitation, and its impact on the overall millimetre-wave signal, and the temporal variability of the signal due to wind speed.

Apart from that, the statistics for route diversity gain covered in the literature review is mostly implied from rainfall and rain radar measurements, which could be considerably different to the actual attenuation measurement of a 42 GHz signal. In order to contribute to this research area, field measurement from proper spatially diverse millimetre-wave radio links need to be accumulated.

The combination of statistical parameters, measurement scenarios and time scale of the long-term measurements that will be undertaken, and to a lesser extent, the underlying live MWS on which the measurements will be made, should enable the long-term field measurement campaign of the campus network trial to provide a unique collation of data.

In order to facilitate widespread field measurements, a cost-effective and highly reliable measurement system must be available and is a central part of the research. The following chapter focuses on this aspect of developing the measurement system for realising the field measurement campaign.

Based on the initial field measurement results, a novel iterative algorithm to mitigate the issue of changes in the local mean of the monitored signal was developed and presented in Chapter 4. Finally, Chapter 5 presents the analysis result of the extensive 42 GHz field measurement campaign.

## Chapter 3

# Cost-effective Measurement System

The conventional use of dedicated measurement instruments to carry out channel measurement of the signal from the millimetre-wave radio receiver is not feasible when a large number of sites need to be monitored over a long-term observation period, due to the likely high costs that will be incurred. The feasibility of employing an off-the-shelf satellite STB as the measurement hardware for various signal parameters has been substantiated following a thorough investigation into the way measurements are performed by the satellite STB, and calibration of these measurements.

A custom data acquisition module was developed, in parallel, to obtain and log these measured signal parameters from an operational satellite STB. The data acquisition module also integrates sufficient storage media for the rapid sampling and extended duration requirement of the field trial measurement campaign. Pairing these two devices results in a cost-effective signal measurement system that comes in under £130 for each measurement site. Thus a widespread, long-term field measurement campaign is facilitated at a low cost.

The field measurement campaign also requires corresponding meteorological data to correlate with events on the channel measurements. To address this, a meteorological measurement system, consisting of a low-cost weather station which measures rainfall, wind speed and direction, and temperature, with automated data logging using a modified version of the developed data acquisition module, is developed. The selected instrumentation costs £150 for each measurement site.

Both developed measurement systems are central in carrying out the 42 GHz MWS campus network trial field measurement campaign, and in obtaining the results presented in Chapter 5.

Prior to installation into the field, each signal measurement system needs to be calibrated in a consistent manner. In view of this, a fade simulation system is developed to provide a relevant stable signal source that can be degraded in a known manner for the calibration task. The fade simulation system is also employed to simulate a given fade profile for algorithm testing in Chapter 4.

### 3.1 Measurement System Design Requirements

Signal measurements are the most direct method to study the millimetre-wave transmission, achieve statistical models and verify propagation theory. Accurate statistical characterisation of these millimetre-wave radio links requires, by convention, that the analysed signal data is obtained from continuous long-term measurement, spanning anywhere between a few months to several years. The measurements should also ideally be conducted at multiple sites with different propagation scenarios, to ensure a broad range of studies such as the spatial distribution of fade events and through foliage links, is possible. While the type of dedicated measurement instruments varies with chosen measurement techniques, these instruments share the same attribute of being fairly expensive due to the frequency of operation and high accuracy requirement. Therefore, it is not practical to make available and dedicate multiple units of these measurement instruments for use in the campus network trial measurement campaign.

To facilitate long-term, wide spread field measurements, the solution for a cost-effective signal measurement system needs to be investigated. The measurement system must be made robust to the uncontrolled operating environment at the deployment site, while measuring the millimetre-wave signal parameters. In addition, the integration of reliable data acquisition, logging and retrieval mechanism is also necessary.

Supporting meteorological data are required to enable correlation of the signal measurement to the weather condition under which the measurement was made. This meteorological measurement system should also share the similar requirement of cost-effectiveness and reliability.

In view of the potential deployment of numerous signal measurement systems, some means of calibrating them consistently must also be investigated.

## 3.2 Millimetre-wave Signal Measurement

One of the primary objectives of campus network trial measurement campaign is to provide a statistical understanding of the long-term performance of a transmitted 42 GHz wideband signal. More specifically, this is the upconverted digital video multiplex signal, adhering to the DVB-S scheme at a symbol rate of 17.5 Msymbols/s with occupied bandwidth of 23.625 MHz (see Section 2.1.1 and 2.1.2). This millimetre-wave signal is transmitted from the head-end base station, and received by the millimetre-wave radio receiver at the user-end which downconverts it to a carrier frequency of 1.66 GHz.

By understanding the types of signal parameter data available and calibrating them, the satellite STB will serve as an ideal source of cost-effective signal measurement hardware. The suitability of using the satellite STB is further compounded by the fact this equipment is already present as part of the CPE set up for service delivery.

The aim towards the important criteria of a cost-effective signal measurement system is met by utilising off-the-shelf satellite STB. One of the main consideration which motivates the investigation of the use of the satellite STB is due to the fact that this equipment is already present as part of the CPE. Both the architecture and functional operation of the satellite STB is extensively examined to understand the type of measurements possible with it. Prior to deploying into the field trial, each satellite STB undergoes an identical calibration process. Results of the calibration indicate repeatability, thus verifying the use of the satellite STB as part of the signal measurement system set up.

### 3.2.1 Definition of Signal Parameters

It is common to refer to the QPSK modulated RF/IF signal employed by DVB-S as *carrier (C)*, to distinguish it from *signal (S)*, which is generally used to refer to the baseband modulated signal. But, given that QPSK is a suppressed carrier modulation scheme [87], this parameter will be referred to as *RF/IF signal* in the rest of the text to remove any potential ambiguity.

The *RF/IF signal power* is defined as the total power of the modulated RF/IF signal as would be measured by a thermal power sensor in the absence of any other signals. For

DVB-S compliant systems, the RF/IF signal passband spectrum is shaped by root cosine filtering with a roll-off factor,  $\alpha$ , of 0.35 [17]. Hence, in an ideal system, all the RF/IF signal power will lie in the frequency band

$$BW_{occ} = f_c \pm (1 + \alpha) \times \frac{f_s}{2} \quad (\text{Hz}) \quad 3-1$$

Equation 3-1 defines the occupied bandwidth of the signal, where  $f_c$  is the carrier frequency, and  $f_s$  is the symbol rate of the modulation. The RF/IF signal power is the total power in this rectangular bandwidth with no further filtering applied.

When the RF/IF signal power is removed, the remaining unwanted interference power present in the system is known as the noise level. The occupied bandwidth as defined by Equation 3-1 is taken as the standard definition of noise bandwidth in DVB-S systems [88]. It is assumed that the noise power is evenly distributed across the frequency spectrum of interest and so can be described by a single noise power density value,  $N_0$ , which is the noise power present in 1 Hz bandwidth. From this, the noise power,  $N$ , present in any given system noise power bandwidth,  $BW_{noise}$ , can be obtained by simple multiplication

$$N = N_0 \times BW_{noise} \quad (\text{dBm}) \quad 3-2$$

Within the context of the campus network trial, there are two signals of relevance which differ by one being a frequency translation of the other. The *received RF signal* outlined in the preceding text is the primary signal of interest in the measurement campaign. However, in terms of practicality, measurements can't be feasibly carried out on the received RF signal directly. This leads to the other signal termed *received IF signal*, which is the product of frequency downconversion from the received RF signal by the millimetre-wave radio receiver. All measurements from the campus network trial are carried out on this IF signal. Given that the millimetre-wave radio receiver is essentially a frequency downconverter, by knowing its gain and linearity, any variation in the monitored received IF signal can be directly correlated to the received RF signal.

### 3.2.2 Signal Measurement via Satellite STB

In the campus network trial, the remote sites receiving live digital video broadcast services also serve as monitoring sites for the transmitted 42 GHz wideband millimetre-wave signal. Set up for the CPEs typically consists of a millimetre-wave radio receiver which downconverts the received RF signal, and a satellite STB that receives the converted IF signal. The Humax F1 satellite STB was chosen for the campus network trial, as it is reasonably priced (at ~£70 each) which matches the required cost criteria, and it also allows manual configuration of the reception signal transmission parameters [89]. This last factor is important as it enables the satellite STB receiver to lock on to digital video signals modulated at different frequency, symbol and forward error correcting rate.

In order to acquire the signal parameter data from the satellite STB, the architecture of the satellite STB need to be fully investigated and comprehended. The architecture here refers to the internal working of the satellite STB at the component level. Typical satellite STB platform entails separating the design into front-end and decoding-end [90], as depicted in Figure 3-1.

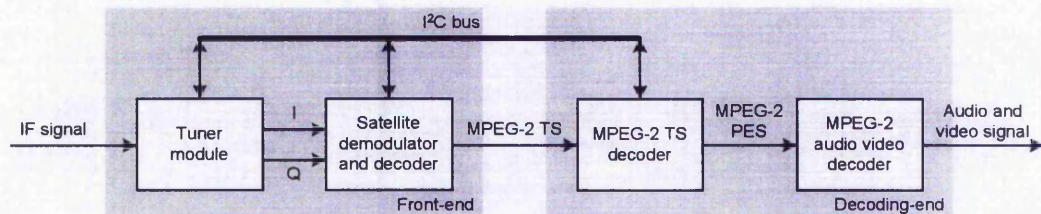


**Figure 3-1: Satellite STB architecture block diagram.**

A tuner module and the satellite demodulator and decoder (SDD) integrated circuit (IC) are the primary components of the front-end. This highly integrated SDD chip performs the demodulation and forward error correction of the received IF signal into MPEG-2 TS data.

The decoding stage combines two key devices that form the operating core of the satellite STB. First of these is the MPEG-2 TS source decoder IC, which descrambles and demultiplexes the MPEG-2 TS into packetised elementary stream (PES). In addition, this IC also carries out all controller tasks related to the satellite STB digital television application, with the embedded processor core and peripheral interfaces such as universal asynchronous receiver-transmitter (UART) and inter-IC (I<sup>2</sup>C) bus units. Further decoding

involves the MPEG-2 audio video decoder IC, which performs audio and video decoding. This IC receives the MPEG-2 PES data and renders it into suitable audio and video signals for reception on a television set.

For the application of signal measurements, the device of interest is the SDD IC. The chosen satellite STB employs the Philips Semiconductors TDA8044AH chip. This highly integrated IC has minimum interface to the tuner, requiring only demodulated analogue I and Q input signals, and a single automatic gain control (AGC) loop back, in order to perform demodulation and decoding on the DVB-S input IF signal [18]. Accordingly, various received signal related parameters could then be obtained from the satellite STB SDD IC. Figure 3-2 illustrates the front-end architecture in more details.

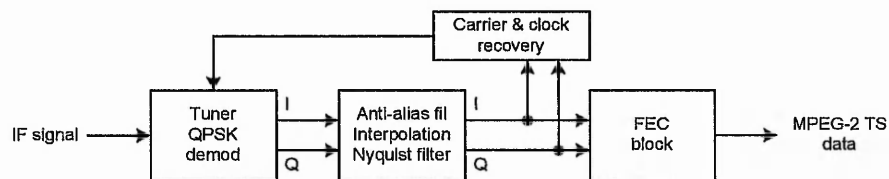


**Figure 3-2: Satellite STB front-end architecture.**

Variations in the received IF signal power can be monitored from the demodulation block. The quality of the transmission may be inferred from a demodulator bit-error-rate (BER) count that is obtained from the Viterbi module in the FEC block. Aspects of end-user service quality can also be gauged from this block in terms of Reed Solomon (RS) readout of packets corrected and packets lost. In addition, the carrier and clock recovery loop provides tracking of the frequency drift of the received IF signal. Data for all these signal parameters can be read from the internal registers of the TDA8044AH chip. Access to these registers, along with communication and control of the SDD, is via the I<sup>2</sup>C bus [18].

By comprehending the types of signal parameter data available and calibrating them, the satellite STB will serve as an ideal source of cost-effective signal measurement hardware. The suitability in using the satellite STB is further compounded by the fact this equipment is already present as part of the CPE set up. By adding a data acquisition module to query and log the signal parameter data from the STB, a very cost-effective signal measurement system can be implemented. Figure 3-3 illustrates the complete signal measurement system that will be employed in the campus network trial field measurement campaign.

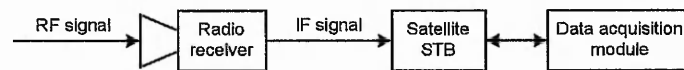


Figure 3-3: Configuration of signal measurement system.

### 3.2.3 Signal Power Measurement and Calibration

Measurements of the received IF signal power can be obtained from the AGC block of the SDD chip. This functional block is implemented to increase the effective dynamic input range of its embedded analogue-to-digital converters (ADC) input, which receive the I and Q channels from the tuner. The configuration for the AGC block is shown in Figure 3-4.

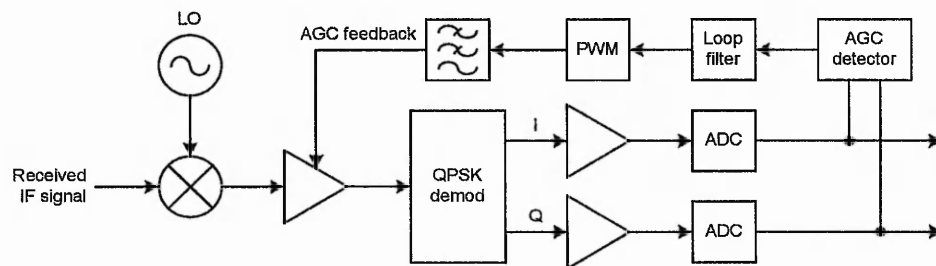


Figure 3-4: AGC block layout.

The AGC peak detector constantly monitors for overshoots in the ADC window. It then provides a feedback signal to the tuner amplifier to ensure the use of the full span of the ADC. The loop filter averages the detector output which in turn drives the external amplifier inside the tuner. This gain or amplification factor,  $AGC_{amp}$ , can be read with 8-bit precision. Therefore, the AGC loop when properly calibrated will provide an accurate indication, via  $AGC_{amp}$ , of the received IF signal power present at the input of the satellite STB.

When a large input signal is present, the required gain is less, resulting in a small  $AGC_{amp}$  (magnitude wise). It follows that as the signal power decreases,  $AGC_{amp}$  will increase. However, the quantisation of  $AGC_{amp}$  is non uniform, having fewer incremental steps for lower gain than at larger gain. Over the signal fade range of interest from -20 to -60 dBm, the typical  $AGC_{amp}$  is seen to traverse 2 steps for each 1 dB change.

Calibrating the values of  $AGC_{amp}$  requires both a stable DVB-S signal source as transmitted by the head-end, and a means of degrading this signal in a known repeatable way. The fade simulation system (introduced in Section 3.6) was designed and implemented to address this requirement. The chief advantage of using this approach is that the calibration process can be easily automated for a large number of satellite STBs. Apart from the considerable saving in time over manual calibration, the precision can also be increased through the simple process of repetition and averaging.

In the calibration process, the signal source is successively attenuated at fixed steps and the corresponding  $AGC_{amp}$  is noted. The attenuation range accounted for is 60 dB, with an attenuation of 0 dB giving a signal power level of -20 dBm. Since the signal source could potentially deviate by  $\pm 0.4$  dBm due to the limitation of the fade simulation system (see Section 3.6.4), the calibration process is carried out in steps of 1 dB.

Samples of the  $AGC_{amp}$  calibration results are presented in Figure 3-5. The plots for calibration of the same satellite STB that was carried out on three separate occasions are virtually identical, with minimal variations at each point. This demonstrates that the signal power measurement from the STB is valid given that it is consistent and repeatable over time. In relation to these, the calibration result for two different satellite STBs also exhibits similar trends albeit with slightly different shaped plot.

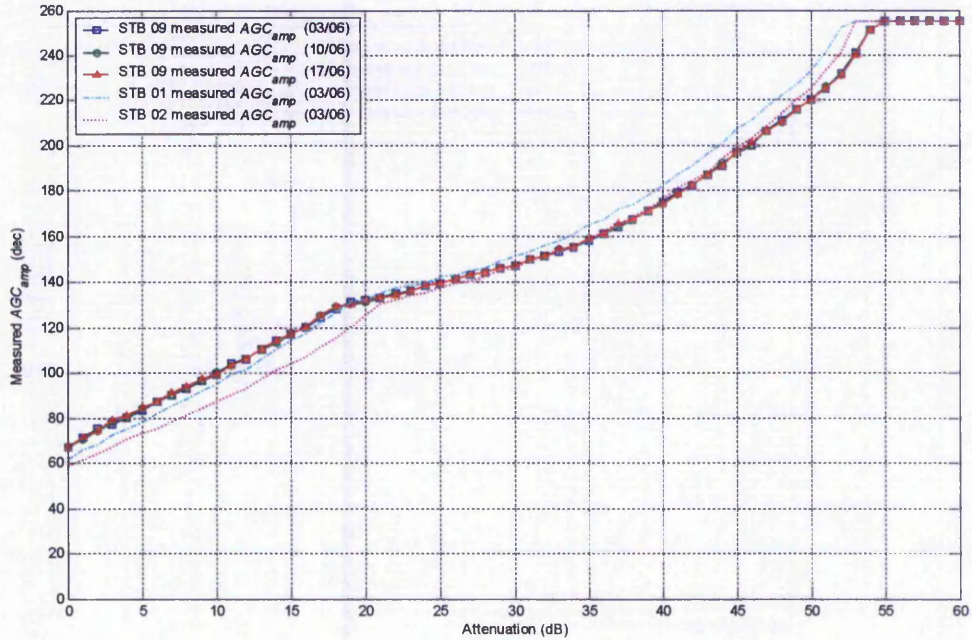


Figure 3-5:  $AGC_{amp}$  calibration result.

From the resulting calibration data, a look-up table consisting of consecutive signal power level and its corresponding assigned  $AGC_{amp}$  for each satellite STB is constructed. These look-up tables will be required to convert the logged  $AGC_{amp}$  into the equivalent received IF signal power in the field trial measurement campaign.

By using a look-up table, the calibration process is essentially quantising  $AGC_{amp}$  in steps of 1 dBm, as illustrated in Figure 3-6.

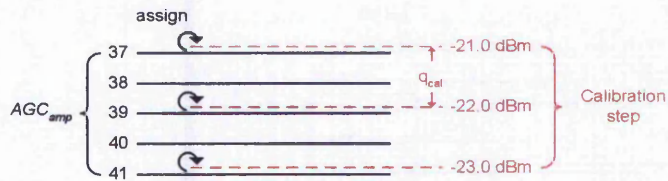


Figure 3-6:  $AGC_{amp}$  calibration steps.

This procedure introduces a quantisation error,  $E_{quant}$ , into the calibration data which is given as the deviation of half a calibration step

$$E_{quant} = \pm \frac{q_{cal}}{2} \quad (\text{dBm}) \quad 3-3$$

Apart from this error, the inaccuracy of the signal source will also need to be addressed. Figure 3-7 provides an extract of  $AGC_{amp}$  and the actual IF signal power that it signifies.

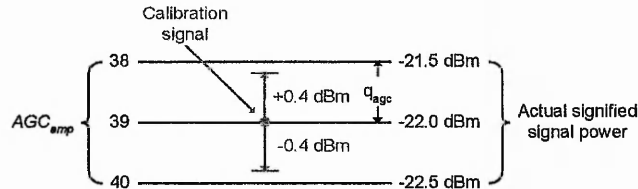


Figure 3-7:  $AGC_{amp}$  corresponding actual power level.

The example shows the representation of a -22 dBm signal source that is fed to the satellite STB, denoted with a period, and its corresponding error bar due to the signal source inaccuracy. There are two possible outcomes during the calibration process. In the first instant, if the signal source is equal to -22 dBm or deviates by up to +0.4 dBm,  $AGC_{amp}$  of 39 will be correctly assigned to the level of -22 dBm. However, if the input signal drops below -22 dBm, the  $AGC_{amp}$  of 40 will be incorrectly assigned to this level. Therefore, the ensuing calibration error,  $E_{cal}$ , is given as

$$E_{cal} = 0 \quad \text{or} \quad E_{cal} = -q_{agc} \quad (\text{dBm}) \quad 3-4$$

where  $q_{agc}$  is the step interval represented by consecutive  $AGC_{amp}$  in the range of interest. Both these errors need to be accounted for in determining the final accuracy of the received IF signal power represented by  $AGC_{amp}$ . The accuracy, denoted as  $AGC_{amp,acc}$ , is determined as

$$AGC_{amp,acc} = E_{cal} + E_{quant} \quad (\text{dBm}) \quad 3-5$$

Using the example of Figure 3-7, when an  $AGC_{amp}$  of 39 is received, the corresponding IF signal power is interpreted as -22 dBm with a maximum accuracy range of -1.0 to +0.5 dBm.

Figure 3-8 further demonstrates that the satellite STB can reliably measure the signal power over the range it was calibrated for. The recorded  $AGC_{amp}$  values measuring a repeating up/down-ramp signal profile can be seen to faithfully reproduce the equivalent attenuation level. Any discrepancies from the ideal attenuation values is inside the range of the stated accuracy of Equation 3-5.

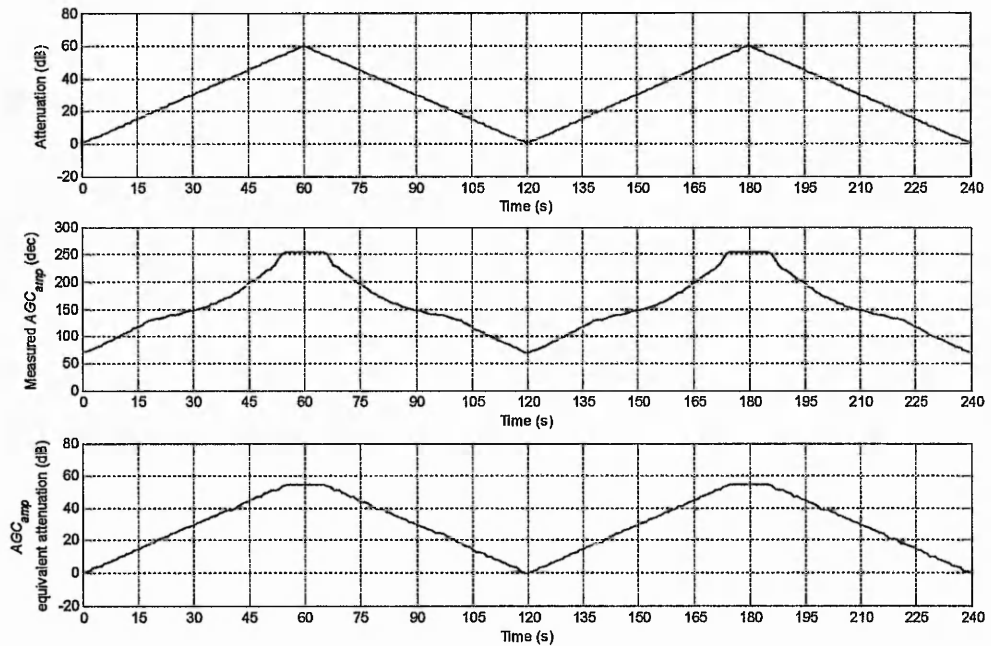
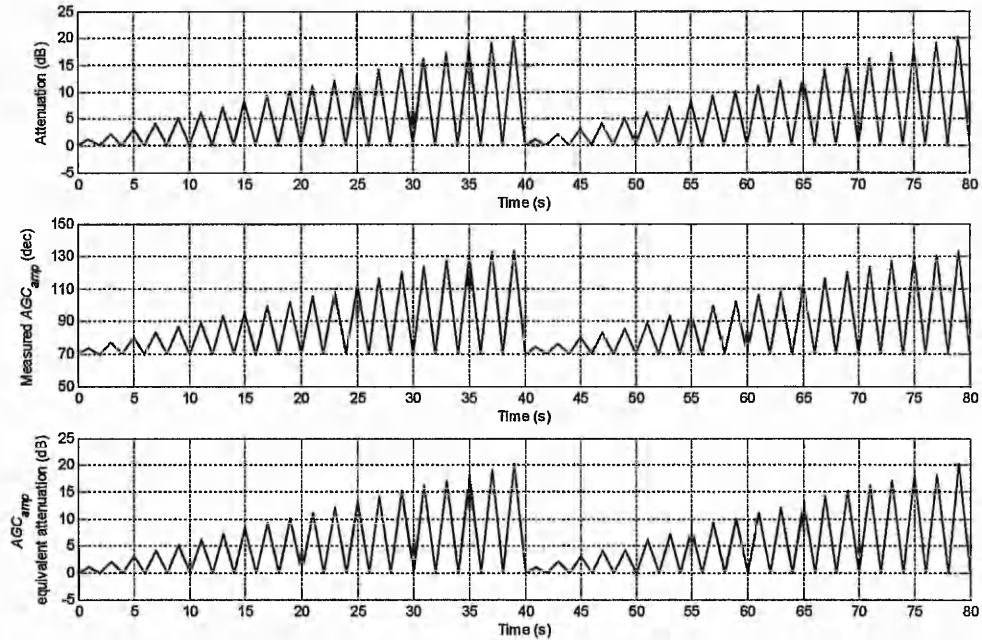


Figure 3-8:  $AGC_{amp}$  range test.

The satellite STB is also tested for its response at measuring rapid fade events. Result for this test is depicted in Figure 3-9.



**Figure 3-9:  $AGC_{amp}$  response test.**

A signal fade profile with an increasing fade slope from 1 to 20 dB/s, in 1 dB/s step, is fed to the satellite STB. The tested upper limit is adequate and much higher than typical recorded fade slope in previous field measurement [81]. Results shown in Figure 3-9 indicate that the satellite STB could effectively track all the different fade slopes.

Combination of all the concluded calibration and test results thus justifies the use of the satellite STB as part of the signal measurement system set up for measuring the received IF signal power.

### 3.2.4 BER Measurement

The SDD chip performs the BER measurement prior to the Viterbi decoder stage inside the FEC block. To obtain this measurement, the signal after Viterbi decoding is coded again using the same coding scheme as in the transmitter, with the aim of producing an estimate of the original coded I and Q sequences. These sequences are then compared at bit level with the signals that are available before Viterbi decoding. Figure 3-10 illustrates the processes involved in this measurement.

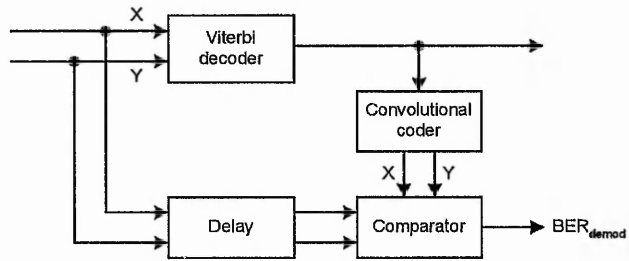


Figure 3-10: Pre-Viterbi BER measurement.

The BER measurement was found to be performed over a count period of  $2^{20}$  bits, with a valid measurement range limited to within  $10^{-2}$  to  $10^{-8}$  [18]. Depending on the selected convolutional code rate, the quasi error free threshold corresponds to a BER before Viterbi decoding in the range  $7 \times 10^{-2}$  to  $7 \times 10^{-3}$ , or a BER after Viterbi decoding of  $2 \times 10^{-4}$  [17].

For the BER measurement to be a useful signal measurement parameter, it needs to be expressed as a function of the ratio of wanted RF/IF signal power to the unwanted noise power ( $C/N$ ). Since  $C/N$  depends on the noise bandwidth, it is common practice to normalise  $C/N$  by using the ratio of energy-per-bit to  $N_0$ , ( $E_b/N_0$ ). The BER measurement from the satellite STB can then be related to  $E_b/N_0$  (or  $C/N$ ) [88] as

$$BER = \frac{1}{2} \times \text{erfc} \sqrt{10^{\left(\frac{1}{10} \times \frac{E_b}{N_0}\right)}} \tag{3-6}$$

However, there is scope for ambiguity as  $E_b/N_0$  can be measured at any arbitrary reference point within the satellite STB receiver chain. In general,  $E_b/N_0$  can be measured *in the channel* and *in the receiver* [88]. There are three filtering processes present in the satellite STB receiver which gives the different possible measurement points for  $E_b/N_0$ , as illustrated in Figure 3-11.

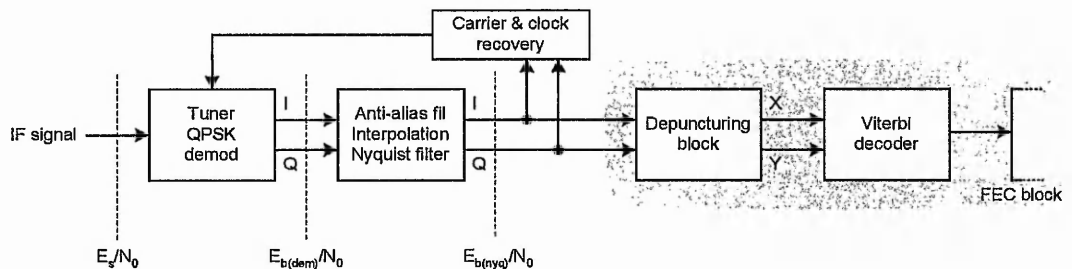


Figure 3-11: Different stages of  $E_b/N_0$  measurement.

The first is a relatively broadband, tuneable, pre-selection filter to reduce the power present to the receiver front-end. A high-order channel selection filter is next, used to extract the desired signal. The third is the root-raised cosine Nyquist filtering, implemented in the low pass filters following I and Q demodulation. This low-pass root-raised cosine filter defines the overall satellite STB receiver's bandwidth and band shape, as the intended purpose of the other filters is only signal pre-selection. Therefore, for *in the receiver* measurement, the modifying effect of the Nyquist filters has to be accounted for.

From Figure 3-11, derivation of the figure of merit for BER as a function of  $C/N$ , and at the various measurement points is given as follow

$$\frac{E_s}{N_0} = \frac{C}{N} - 10 \log_{10} \left( \frac{f_s}{BW_{noise}} \right) \quad (\text{dB}) \quad 3-7$$

$$\frac{E_{b(dem)}}{N_0} = \frac{E_s}{N_0} - 10 \log_{10} (\text{number of bits per symbol}) \quad 3-8$$

$$\frac{E_{b(nyq)}}{N_0} = \frac{E_{b(dem)}}{N_0} + 10 \log_{10} \left( 1 - \frac{\alpha}{4} \right) \quad (\text{dB}) \quad 3-9$$

The BER measurement from the satellite STB is made at the point prior to the Viterbi decoder stage. By manipulating Equation 3-7 to 3-9, this BER measurement can be related to each measurement point and utilised to measure and derive insight into the quality of the received RF/IF signal transmission.

### 3.2.5 Frequency Offset Measurement and Calibration

The phase-frequency loop, which is part of the carrier recovery block, provides a measure of the frequency offset of the input signal to the SDD chip. This loop keeps track of the frequency and phase of the received signal to get a steady constellation diagram and valid I and Q values for the FEC unit. The configuration for the phase-frequency loop is as shown in Figure 3-12.

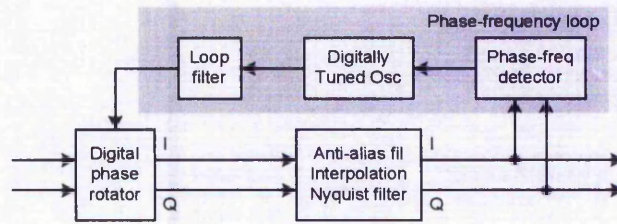


Figure 3-12: Phase-frequency loop block layout.

To determine how well this frequency offset measurement track a real frequency drift, a signal source with a tuneable carrier frequency is fed to the satellite STB. This signal is obtained by using a mixer to appropriately shift the carrier of the mixer product, of the suitable signal and the local oscillator from a signal generator. The resulting signal source has a nominal frequency of 1.66 GHz and can be tuned over the range of  $\pm 5$  MHz. Figure 3-13 shows the frequency measurement result of a signal source incrementing from 1.655 GHz to 1.665 GHz in steps of 1 kHz every 50 ms.

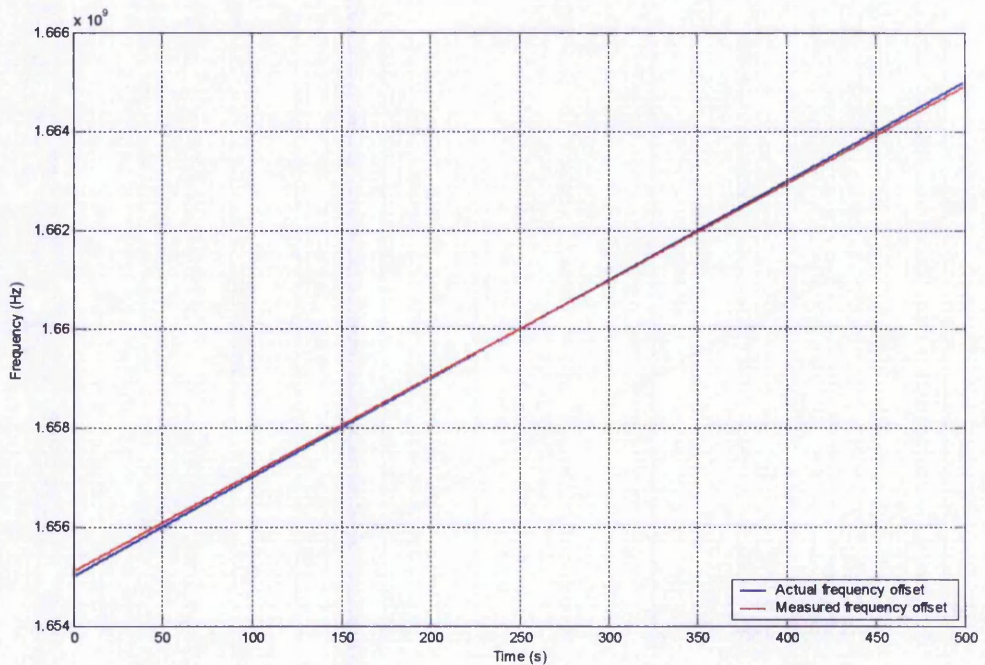


Figure 3-13: Frequency offset measurement calibration result.

The chosen test frequency range is representative of the possible frequency drift of the received IF signal in the measurement campaign, due to the construction and operating specification of the millimetre-wave radio receiver [91]. Across this frequency range, the

satellite STB can be seen to provide adequate tracking of the simulated frequency drift. While the smallest resolvable frequency step is approximately 120 Hz [18], the accuracy of the frequency offset measurement was found to be within  $\pm 3$  kHz. This is depicted in Figure 3-14, as histogram of multiple frequency offset reads taken at several frequency point of interest.

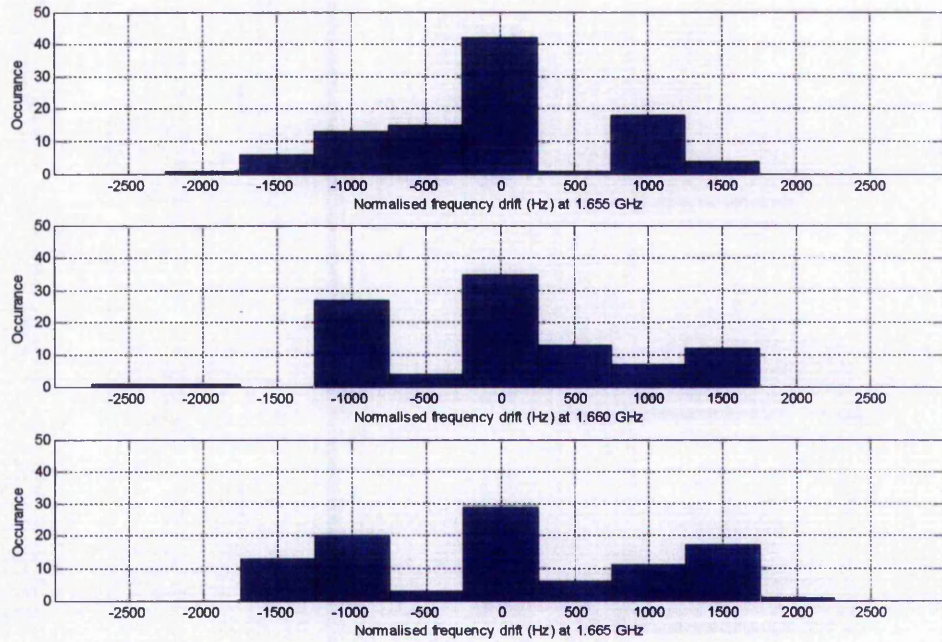


Figure 3-14: Frequency offset measurement accuracy test.

### 3.3 Data Acquisition Module for Satellite STB

The required signal parameter data needed to be acquired and logged in a reliable and cost-effective manner. Due to very specific interface requirement and also the obligatory large memory storage, commercially available data loggers are deemed unsuitable. In order to meet the stated requirements, a custom data acquisition module (DAM) was designed and constructed. The soundness of the DAM design has been demonstrated through operation in the measurement campaign, where numerous units were deployed.

#### 3.3.1 Satellite STB Operation

Understanding the operation of the satellite STB is essential owing to the fact that apart from serving as signal measurement hardware, the satellite STB is also being used in parallel to receive and view digital video broadcast at the user-end. In this latter role, the satellite STB could be in any one of the three operating modes, namely *switch on*, *standby* and *switch off*. Each operating mode could potentially disrupts the DAM from acquiring and logging the required signal parameter data.

When the satellite STB is in *switch on* or normal operating mode, the tuner module will be supplying power to the millimetre-wave radio receiver. The IF signal from the millimetre-wave radio receiver will be continuously demodulated and decoded by the active SDD chip. When the user changes the video channel to one that is on a different broadcast multiplex, the tuner module will tune to this new broadcast multiplex which is at a different IF carrier frequency.

In *standby mode*, power output from the tuner is cut off in order to conserve power consumption. As a consequence, the millimetre-wave radio receiver will be non-functional. In addition, the satellite STB will also put its core ICs, including the SDD chip into sleep mode. The last possible situation is the *switch off mode* in which the mains power to the satellite STB is cut off. In contrast to the previous mode, the power supply unit within the satellite STB is as expected, no longer providing any output when in *switch off mode*.

### 3.3.2 I<sup>2</sup>C Bus Specifications

Given that the required signal parameter data can only be accessed via the satellite STB I<sup>2</sup>C bus, a proper understanding of the bus design and protocols are necessary. This is further compounded by the fact there is a distinct lack of commercially available tools for monitoring the I<sup>2</sup>C interface, which means that a custom interface must be built.

In many electronic systems such as the satellite STB, there are a number of peripheral ICs that have to communicate with each other and the outside world. To maximize hardware efficiency and simplify circuit design, Philips Semiconductors developed a simple bidirectional 2-wire, serial data (SDA) and serial clock (SCL) bus for inter-IC control. With its inherently simple operation coupled with the extremely broad range of I<sup>2</sup>C compatible devices from Philips and other suppliers, the I<sup>2</sup>C bus has become the embedded industry standard proprietary control, data, diagnostic and power management bus.

Each I<sup>2</sup>C compatible device is recognized by a unique address and can operate as either a receiver only or with the capability to both receive and send information. In each instance, the devices can operate in either master or slave mode, depending on whether the device has to initiate a data transfer or is only addressed. Figure 3-15 depicts the master-slave and transmitter-receiver relationship as well as the access protocol.

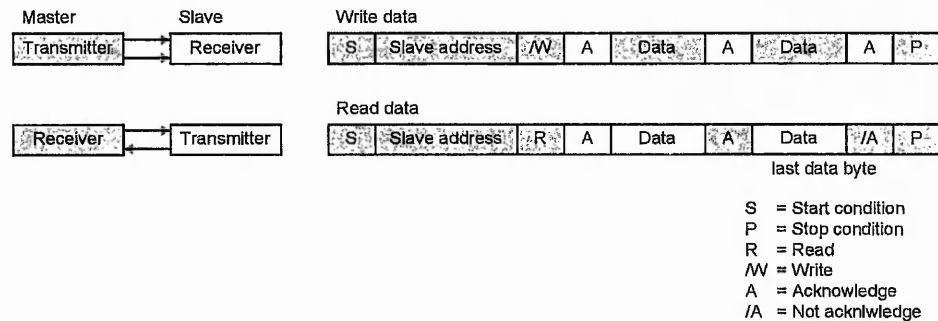


Figure 3-15: I<sup>2</sup>C bus communication protocol.

Detailed signalling procedure for the bus can be obtained from the I<sup>2</sup>C specification [92]. Data transfer on the bus is serial, 8-bit oriented at the standard transfer rate of 100 kbits/s. I<sup>2</sup>C is also a true multi-master bus with collision detection and arbitration to prevent data corruption if two or more masters simultaneously initiate data transfer.

### 3.3.3 DAM Design Requirements

Analysis of the DAM design requirements starts with the essential issue of cost, and to a lesser extent, size. In keeping with the aim for a cost-effective measurement hardware solution, the cost of the DAM must be kept to a minimum. The Humax F1 satellite STB cost of approximately £70 per unit, provides the most logical ceiling components budget for each DAM. In terms of physical dimension, the DAM will need to be sufficiently compact with the aim of incorporating it inside the enclosure of the satellite STB. This necessitates a well thought-out two-layered printed circuit board (PCB) board layout. To minimise both cost and size, the component count must be reduced by ensuring that the DAM is designed to make full use of all available resources on the satellite STB hardware itself.

A top-down method of design was used in developing the DAM. This allows for a clear definition of the overall structure of the interface involved and the flow from one block to the other. This context is illustrated in Figure 3-16.

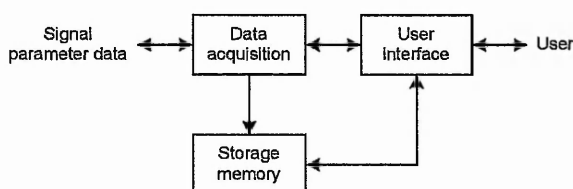


Figure 3-16: DAM top level block diagram.

From this design approach, the DAM presents a simple premise. Essentially, it needs to acquire the signal parameter data and logged it for latter retrieval, with a user interface to communicate externally.

A user interface is necessary to allow communication with and control of the DAM. Requisite control commands include initiating the data acquisition, monitoring the acquisition process and retrieving the logged data. To keep the design simple, a common scheme such as the RS-232 communication protocol can be utilised. Furthermore, the DAM can share the unused lines of the RS-232 port on the satellite STB itself.

Suitable data that is available from the satellite STB covers seven separate signal parameters. Table 3-1 gives the tabulated breakdown of each signal parameter and the physical storage space that it requires.

Signal parameter	Number of bytes
AGC <sub>demod</sub>	1
FEC lock flags	1
Frequency drift	3
CNR estimate	1
BER <sub>demod</sub>	3
RS block corrected	1
RS block lost	1

**Table 3-1: Breakdown of signal parameter data bytes.**

The amount of storage memory required will depend on the number of signal parameters that are to be stored, the rate of data acquisition and ultimately how long the logging process needs to last. For this last factor, a data retrieval of every 2 weeks is deemed a suitable compromise between reducing the frequency of visits to each monitoring site and the risk of losing data in the event of equipment failure. The data also needs to be time-tagged for it to be useful. A suitable real time clock source will be needed, along with a software solution to do away with tagging every single data to reduce the necessary storage memory.

A logic analyser was utilised to tap into the I<sup>2</sup>C bus when the satellite STB is in *switch on mode*. In this mode, the onboard controller (in the MPEG-2 TS decoder IC) was observed to periodically query the same signal parameter data. Captured I<sup>2</sup>C waveforms reveal that the interval between successive queries is approximately 100 ms. While there is no available information on the firmware design of the controller, manual monitoring and testing demonstrated that controller uses this monitoring loop to ensure that none of the carrier recovery or FEC stages have come out of sync. If any stages do become unlocked, the controller will reinitialised the SDD chip and put it through the synchronising programming cycle to lock back on to the IF signal.

By capturing this programming sequence, and further referencing the TDA8044AH data sheet [18], sufficient information is gained in terms of being able to manually reprogram the front-end of the STB. Therefore, the front-end can now be employed to demodulate and decode any DVB-S signal independently of the default setting of the satellite STB. An extract of the captured I<sup>2</sup>C waveform is shown in Figure 3-17.

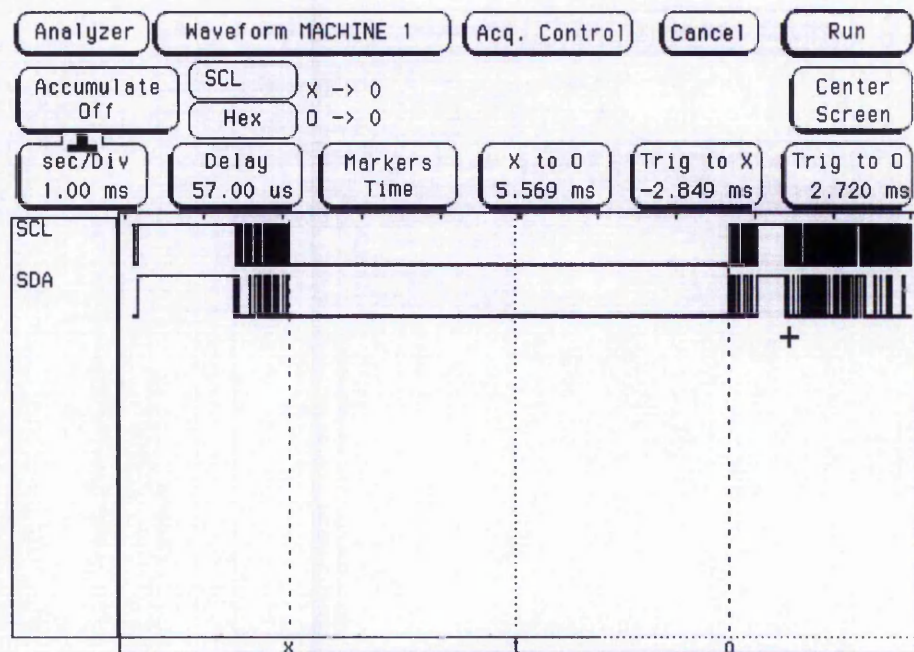


Figure 3-17: I<sup>2</sup>C bus data waveform.

Since the signal parameter data is readily available, the DAM should thus operate as a non-intrusive monitor. The I<sup>2</sup>C bus being monitored will then operate in the same way, whether or not the DAM is attached. Seeing as there are many other communications on the I<sup>2</sup>C bus, the DAM in its passive monitoring mode will need to filter messages on the bus by slave and registry address.

In contrast, when the satellite STB is put into *standby mode*, all the main ICs are disabled and the I<sup>2</sup>C bus goes silent. During this state, the DAM will need to reactivate the tuner module first, followed by the SDD chip. With the controller IC still disabled, the required data will need to be actively queried. In both *switch on mode* and *standby mode*, the DAM could draw its power supply directly from the satellite STB power conversion and rectifying unit.

While all attempts are made to keep the satellite STB continuously powered up, uncontrollable factors such as power failure or user error could completely cut off power to the satellite STB. In this *switch off mode*, the DAM has to be capable of maintaining the validity of the logged data in the storage memory, in the absent of system power. When power supply is resumed, the DAM must be able to automatically recommence acquiring and logging the signal parameter data. Some form of nonvolatile storage memory is thus required to maintain the storage memory address pointer. A nonvolatile real time clock is also necessary to maintain a power-up table to indicate when the new logging begins.

Table 3-2 summarises the DAM design requirements under the various operating modes of the satellite STB.

Satellite STB mode	DAM requirements
<i>Switch on</i>	<ul style="list-style-type: none"> <li>- Passively monitor I<sup>2</sup>C bus for data sequence.</li> <li>- Draw power from satellite STB.</li> </ul>
<i>Standby</i>	<ul style="list-style-type: none"> <li>- Activate tuner module and SDD chip.</li> <li>- Actively query data from SDD chip.</li> <li>- Draw power from satellite STB.</li> </ul>
<i>Switch off</i>	<ul style="list-style-type: none"> <li>- Maintain logged data.</li> <li>- Track power-up time and auto resume data logging when coming out of this mode.</li> </ul>

**Table 3-2: DAM requirements under different satellite STB modes.**

### 3.3.4 SRAM Based DAM

The initial version of the DAM only logged the  $AGC_{amp}$  data which is one byte long. Since the most expensive component of the DAM is the storage memory, the data acquisition was carried out once every 3 s to lessen the storage capacity requirement. With this data rate and a retrieval period of every two weeks, a static random access memory (SRAM) chip can be used as the main storage memory. The chosen SRAM is organised as 524,288 words by 8 bits, giving a total storage capacity of 512 KiB. With this storage capacity, the DAM could run continuous for a maximum of 18 days. Figure 3-18 illustrates the functional block diagram of the SRAM based DAM.

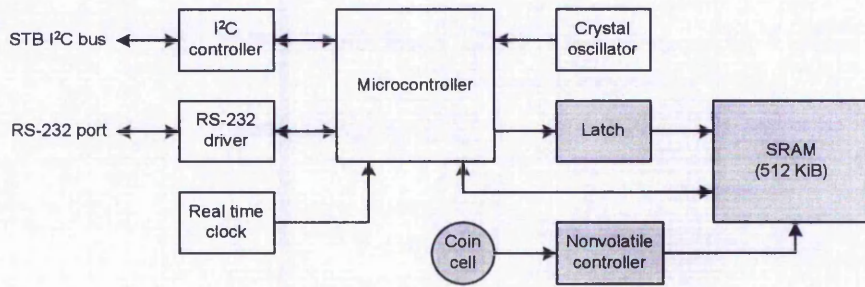


**Figure 3-18: SRAM based DAM components layout.**

Since, the SRAM requires a significant number of input/output (I/O) lines to function, a latch is employed to multiplex the address lines and data lines together to ensure that there will be sufficient I/O lines to access the SRAM.

In the event that the satellite STB is in *switch off mode*, the nonvolatile controller will supply the monitoring and logic required to make the SRAM nonvolatile. Precise voltage sense and comparator circuits monitor the supply voltage for power failure. When the voltage falls out of range, an automatic switch to battery power provided by the lithium coin cell activates. The logged data is thus maintained while power is out of range. A small part of the, now nonvolatile, SRAM is also partitioned off to store the address pointer and power-up table.

All controller tasks related to the data acquisition and logging are performed by a dedicated microcontroller. The microcontroller achieves this by executing a specifically programmed routine to control the onboard devices. Apart from being low-cost, the main criteria for the chosen microcontroller is having sufficient I/O lines and processing speed to cope with the task at hand. In both respects, this microcontroller copes well as it has an adequate well-defined I/O structure and peripherals that limit the need for external components, while featuring a fast core, running single cycle instructions. Furthermore, it enables quick code troubleshooting and optimising via an on-chip in-system programmable Flash memory. The clock source for this microcontroller comes from the crystal oscillator, which is also shared with the I<sup>2</sup>C controller.

The RS-232 driver is designed for RS-232 communication interface where a  $\pm 12$  V supply is not available, using charge-pump capacitors to convert the +5 V input to the required levels. In the case of the microcontroller, this transceiver allows the user to communicate

with it via a PC COM port. At a transfer rate of 57 kbits/s plus overhead, the entire content of the SRAM can be retrieved in approximately 4 minutes transmitted as American Standard Code for Information Interchange (ASCII) formatted string.

With the I<sup>2</sup>C controller, the microcontroller can use the parallel data bus to communicate bidirectionally with the serial I<sup>2</sup>C bus. Communication with the I<sup>2</sup>C bus is carried out on a byte-wise basis using polled handshake. This IC controls all the I<sup>2</sup>C bus specific sequences, protocol, arbitration and timing. For the purpose of data logging from the satellite STB, the I<sup>2</sup>C controller can be configured to act as a passive I<sup>2</sup>C bus monitor. The main feature of this mode is that it allows passive monitoring the I<sup>2</sup>C bus traffic and automatic storing of any received data.

The chosen real-time clock (RTC) provides nonvolatile timekeeping with internal elapsed time counter. This counter constantly maintains real time by counting seconds, whether powered from the external power supply or from its internal battery backup. Output from the counter is binary data that can be read in standard clock and calendar format using a software algorithm. Communication to and from this real-time clock takes place via Dallas Semiconductor 3-wire serial bus interface [93].

Based on the selected components, a two-layered PCB board layout was designed and fabricated in-house. All components including the surface mount devices were then manually soldered onto the PCB board and tested for functionality. A photo of the completed DAM housed inside the satellite STB is shown in Figure 3-19.

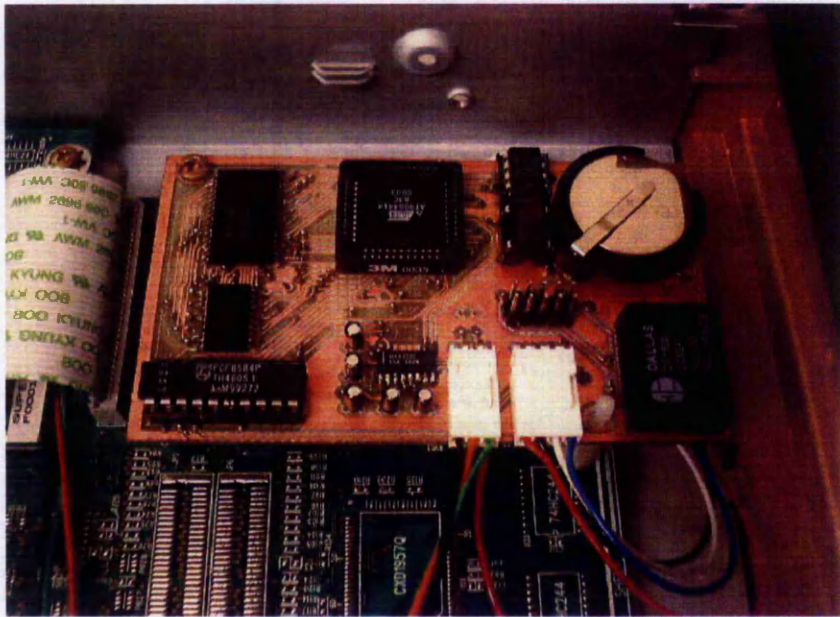


**Figure 3-19: Photo of the SRAM based DAM.**

### **3.3.5 Assembly Language Program for SRAM Based DAM**

In order for the SRAM based DAM to carry out its tasks, an assembly language program is written to the microcontroller to provide it with the necessary intelligence. The final form of the program was achieved after having gone through many iterations of thorough testing and revision. An overview of this program flow is presented in Figure 3-20.

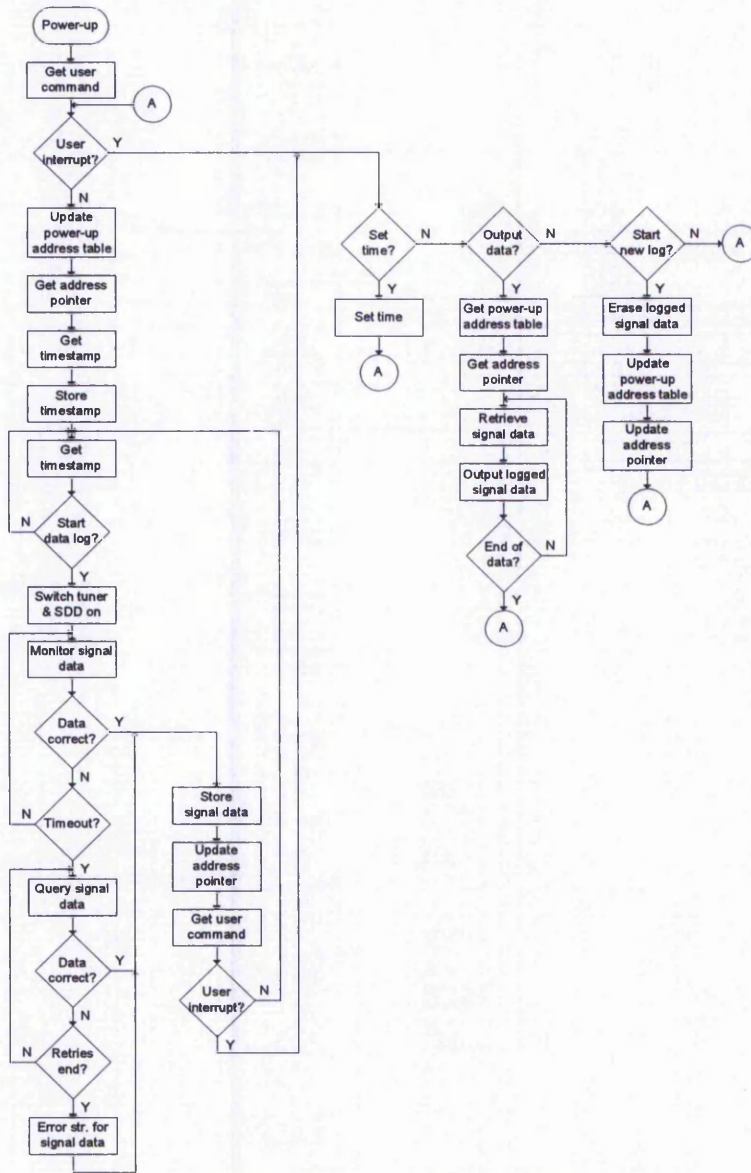


Figure 3-20: SRAM based DAM program flowchart.

Upon start-up, the DAM will either resume or start the data acquisition process, depending on the present of a power-up condition or a user initiated acquisition cycle. The ensuing initiating program flow included routines to support the stated process when the DAM is activated.

Next, a delay loop fixes the acquisition rate. In this application, the delay loop exits after 3 s has elapsed. The program flow then assumes that the satellite STB is in *switch on mode* and attempts to passively monitor and log the required signal parameter data from the I<sup>2</sup>C bus traffic. If this data is not readily available such as when the satellite STB is put into

*standby mode*, the program flow will initiate a write to the SDD chip registers and request for the relevant data readout. A timeout loop is implemented to limit the number of retries. Following timeout, a known error string will be written to the SDRAM memory in place of the data.

During each acquisition cycle, the program polls the RS-232 interface for user input. By adhering to a self-defined command set, the user can execute any of the indicated command routines. The principal activity of the user input routines include; setting the real time clock, retrieving the logged data, and starting a new data acquisition and logging cycle.

To ease troubleshooting and reduce the complexities of the many program routines involved, a modular approach to the coding is adopted. Partitioning the assembly language program flow into modules is intuitively done at the component level. Each one is treated as a separate entity, with well defined interfaces consisting of subroutines to execute the basic tasks specific to the component itself. A higher level program routine which needs to access the component can then simply manipulate these subroutines. Figure 3-21 shows the subroutines involved in the assembly language program for the DAM.

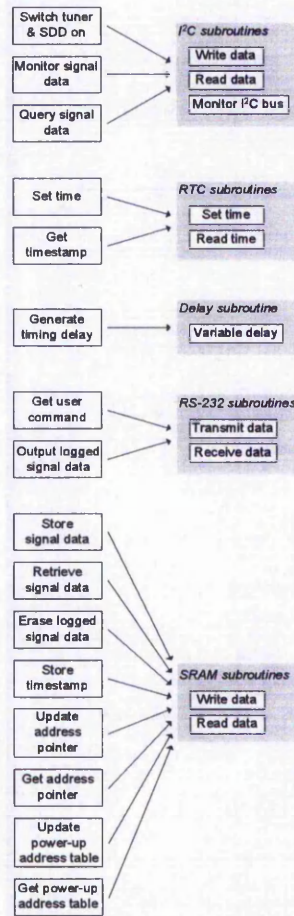


Figure 3-21: SRAM based DAM program subroutines.

This modular design approach also enables simple addition of new module to the overall program flow, or modification to existing module without disruption other portions.

### 3.3.6 SmartMedia Based DAM

In order to log all the available signal parameter data totalling 11 bytes at a faster acquisition of every 1 s, a significantly larger storage memory is required. With the recent price drop in solid state memories, devices such as the SmartMedia memory card prove to be a viable alternative. At the stated data rate, a 32 Mibytes SmartMedia could store up to 35 days worth of data. Yet, the cost for the SmartMedia is similar to the previous chosen SRAM.

The original DAM was therefore updated with the improved storage memory solution. This SmartMedia based DAM still retains many of the previous design and components features, dropping only the SRAM along with its supporting devices. Figure 3-22 depicts the functional block diagram of the modified DAM, with shaded blocks representing the difference compared to the previous version.

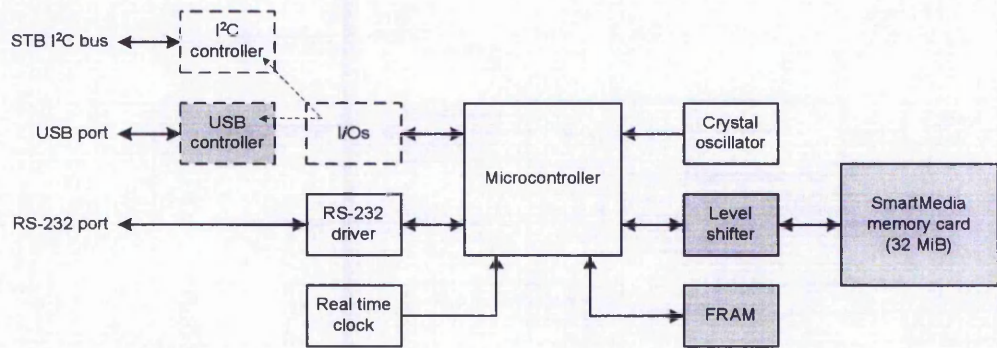


**Figure 3-22: SmartMedia based DAM components layout.**

The SmartMedia memory card is slotted into a compatible socket positioned on the outer side of the satellite STB's enclosure. Collecting the logged data just be simple matter of ejecting the memory card and retrieving the data in a separate dedicated DAM. A ribbon cable connects this socket to the rest of the DAM module located inside the enclosure.

Internally, the SmartMedia is mounted with flash memory that is electrically rewritable and can retain data without the need of external power. Address and data lines for the SmartMedia are multiplexed into its 8 I/O ports. Having a data path of only 8 bits requires that the large addresses be broken up into byte-sized pieces, transferred, and reassembled internally. The format of a small, predetermined command enables the SmartMedia to know what is coming through [94]. A *page*, consisting of 512 bytes plus 16 redundant bytes of flash arrays, is the smallest portion of memory that can be written to the flash memory. The SmartMedia has a page size buffer to cater for this read/write operation. Conversely, the smallest portion of memory that can be erased is in units of 32 pages known as a *block*.

Hardware development based on SmartMedia requires an overhead of invalid block management. Invalid blocks are blocks that contained one or more invalid bits whose reliability are questionable. The SmartMedia may already contain, and further develop

additional invalid blocks over its life time. Another additional complexity involves the different operating voltage of the SmartMedia. To mitigate this, a level shifter is used to interface between the 3.3 V environment of the SmartMedia and the predominantly 5 V environment of the rest of the DAM.

The original microcontroller is no longer adequate for the current DAM. An improved version with a larger internal working SRAM area is chosen to match the SmartMedia data buffering and invalid block management requirement. To augment the invalid block management, a nonvolatile ferroelectric RAM (FRAM) memory is utilised to store a table of invalid blocks. The FRAM also contains the address pointer and power-up table.

A Universal Serial Bus (USB) connection substitutes the relatively slow RS-232 interface for retrieving the large amount of logged data. The USB controller module is designed to be a drop in replacement for the I<sup>2</sup>C controller when the DAM is dedicated to just retrieving the logged data. It automatically handles all USB protocols and offers a first-in-first-out (FIFO)-like design for easy interface to the microcontroller. The USB module comes with a virtual COM port driver that masked the USB port as standard RS-232 port. To maintain a reliable data capture on the PC, the transmission rate is deliberately restricted to 800 kbits/s. Nonetheless, transfer of 32 Mibytes of data from the SmartMedia formatted in ASCII is still completed within a short time of 11 minutes.

All components for the DAM are manually soldered onto the two fabricated dual-layer PCB boards. Each DAM is thoroughly tested for functionality prior to deploying into the field. Figure 3-23 is a photo of the completed SmartMedia based DAM.

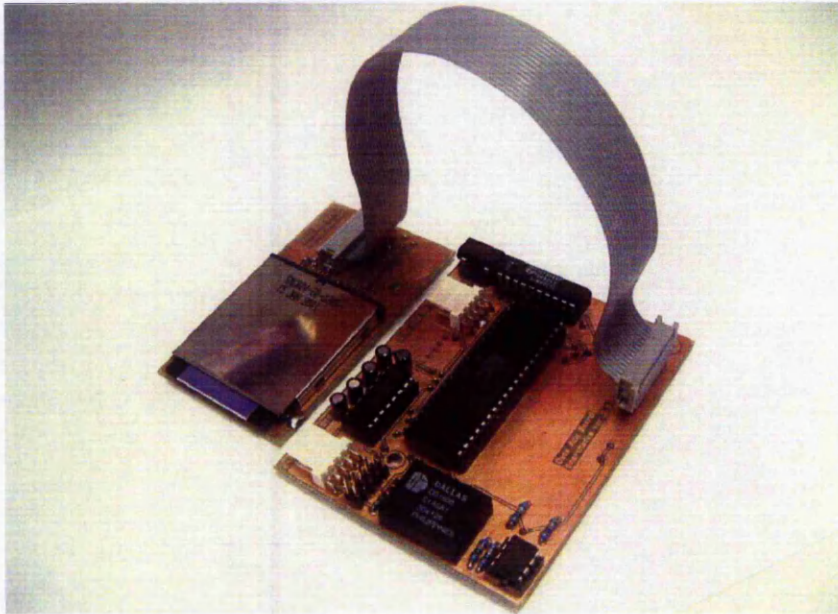


**Figure 3-23: Photo of the SmartMedia based DAM.**

### **3.3.7 Assembly Language Program for SmartMedia Based DAM**

Similar to the hardware, most of the assembly language program written for the previous version of DAM can be reused. This undertaking was fairly straightforward as the earlier program adopted a modular designed approach. Routines and modules related to the SRAM were simply substituted with those for the SmartMedia. Figure 3-24 shows the updated program flow, with shaded blocks representing new routines associated with the SmartMedia.

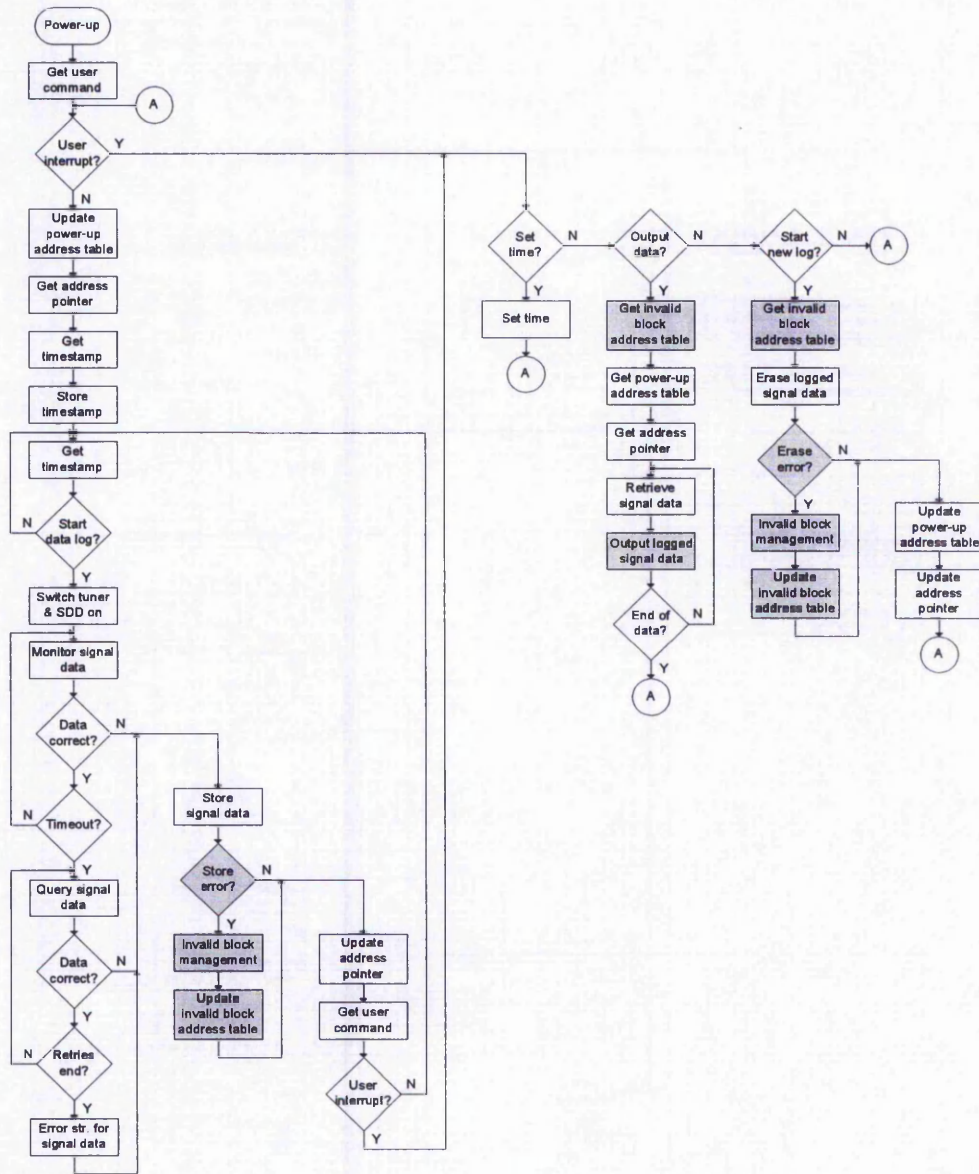
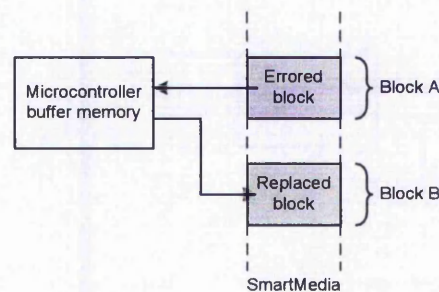


Figure 3-24: SmartMedia based DAM program flowchart.

Two additional invalid block management program routines deal with the need to mask out invalid blocks of the SmartMedia from the storage address mapping. This task is non-trivial as the routines must be made transparent to the overall operation of the program flow. On top of this, the routines must also be made tolerant to the program flow restarting following a power-up cycle.

The first program routine deals with the identifying of initial invalid blocks. Since the invalid block information in the SmartMedia is also erasable in most cases, the program routine recognises invalid block based on the original invalid block information and creates a separate invalid block table.

Management of additional invalid blocks is provided by the second program routine. An error-detection mechanism monitors the status flag of the SmartMedia for failure indication on every erase or write cycle. When an erase failure occurs, future access to the affected block is prevented by updating the invalid block table. If an error occurs after a write operation, the contents of the block in question are rewritten to the next available block by loading to and from an external buffer. Access to the invalid block is similarly prevented by updating the invalid block table. This block replacement procedure is depicted in Figure 3-25.



**Figure 3-25: Block replacements following SmartMedia write failure.**

In the event that the DAM is dedicated towards retrieval of the logged data, the data transmit function is replaced with a USB routine. Access to the user input commands still remains via the RS-232 routines.

Several new subroutines complement all the modified changes to the original assembly language program. These distinct subroutines come from the newly added components and are as shown in Figure 3-26.

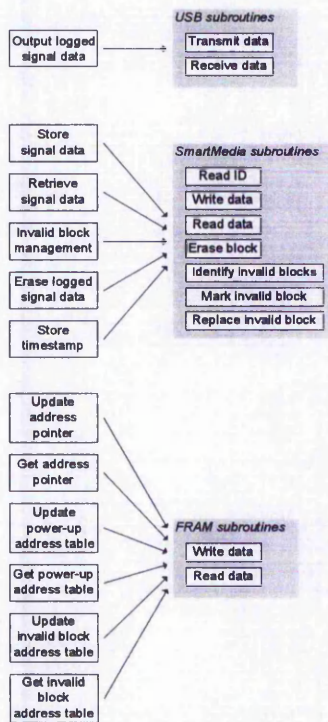


**Figure 3-26: SmartMedia based DAM program subroutines.**

### **3.4 Meteorological Data Measurement**

Study of the millimetre-wave transmission requires supporting meteorological data on which to correlate events on the channel measurement results. An observed fade event on a LOS link can, as an example, be attributed to rain attenuation and scattering only if the presence of rain is recorded during that time. But suitable weather stations that provide an array of weather conditions information including rainfall rate, wind speed and direction and temperature, at the necessary resolution and reasonable accuracy, are typically complex and expensive [95].

A cost-effective solution was found in the form of a weather station that employs an efficient power and data transmission technique. Collection of data from this weather station is automated using a modified version of the developed DAM. This pairing has been deployed in the campus network trial and throughout its operation in the field, proven to be a reliable source of meteorological measurement.

#### **3.4.1 Meteorological Data via 1-Wire Weather Station**

In the design of a conventional weather station, each sensor requires its own wiring and power supply. The sensor must also be signal conditioned before transmission. Adding sensors to an existing weather station will thus require more wires and electronics. These factors contribute to a meteorological instrument system that is inefficient and expensive [95].

The 1-Wire weather station developed by Dallas Semiconductor was determined to be the best option following an extensive search of available commercial offerings. It solves the stated problems by transmitting both power and bidirectional data for all sensors over one single twisted-wire cable. More importantly, the weather station cost only a fraction of professional systems, while closely matching them in accuracy and resolution. Rainfall, wind speed and temperature measurements essential to the campus network trial measurement campaign are provided, along with the less important wind direction measurement. To simplify communication with the sensors, the 1-Wire weather station features a serial-to-1-Wire bridge, thus requiring only a modest RS-232 interface.

In terms of field deployment, a rainfall and temperature sensor has been installed next to the head-end millimetre-wave transceiver at the base station. The wind sensors were not set up given that no related signal measurement requires the data. Apart from that, the high elevation of the site will significantly bias the result. In contrast, a complete 1-Wire weather station has been deployed on the roof apex of a residential house which monitors both clear LOS and through tree transmission. Figure 3-27 is a photo taken during the installation of the weather station.

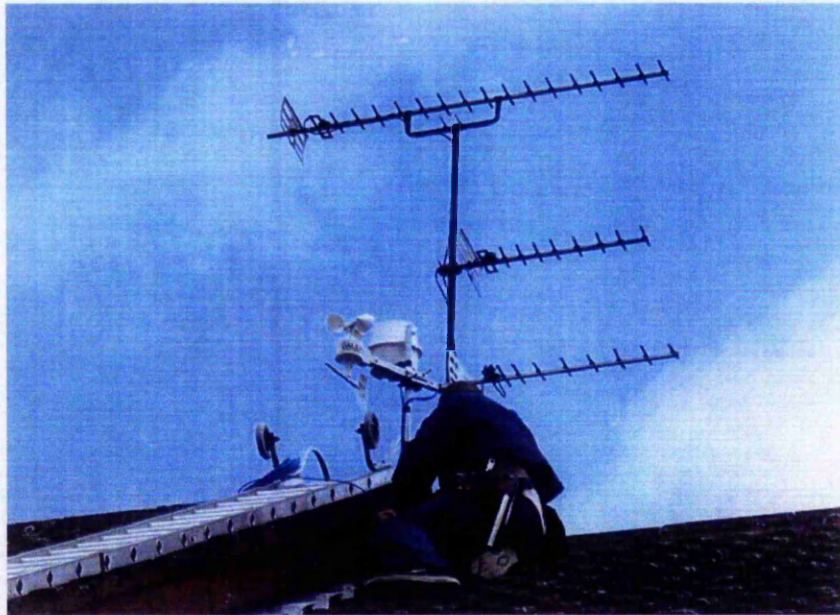


**Figure 3-27: Installation of 1-Wire weather station.**

### **3.4.2 Rainfall Rate Measurement**

As discussed, the predominant cause of fade event on a millimetre-wave LOS link is due to rain. A tipping bucket rain gauge is employed to measure the intensity of the rainfall.

Since the data measured is effectively a single point rainfall rate measurement, factors such as inhomogeneities in the rain rate field will lead to errors in the specific attenuation to rainfall rate relationship. These errors will peak in the present of heavy rainfall which tends to be highly localised or strong wind that is perpendicular to the link. Variability in the drop size distribution will also lead to spread of specific attenuation versus rainfall rate data. Furthermore, this rain gauge is not as sensitive as a specialised rapid-response rain gauge and rain drop-size distrometer used in other measurement experiment for the said

intention [28]. Rather, for the purpose of the campus network trial, the rainfall rate data is primarily used to indicate the occurrences and duration of rain events.

Similar to conventional professional set up, rainfall is measured with the fill-and-tip method. Rain enters the collector, drips through a small hole in its funnel shaped bottom, and falls into one of two identical buckets on either end of a beam which pivots around a central axle. When the upper bucket is full, that end of the beam pivots down, spilling and draining the water away, while raising the other end up. Each time the beam moves, a magnet mounted to it momentarily closes a reed switch, with each closure indicating that a calibrated volume of rain has fallen. The rain gauge incorporates a 1-Wire counter chip with the read switch, which increments on each closure. Rainfall rate can thus be measured by counting the number of tips over the required integration time. The rain gauge is calibrated for a resolution of 0.25 mm per tip.

### **3.4.3 Wind Speed Measurement**

Millimetre-wave transmission through foliage suffers attenuation and scattering. The amount of power variation also exhibits a strong dependency on wind speed. For measurement of wind speed, the 1-Wire weather station uses a rotating wind cups.

The sensor for the measurement consists of two magnets mounted on the edge of a second rotor attached to the wind cup's axle. The magnets operate a reed switch connected to another counter chip and provide two counts per revolution. This two-magnet arrangement improves response at low wind speed while providing rotational balance to the rotor. The counter chip keeps track of the total number of wind cup revolutions and transmits the data on demand. Wind speed is derived by taking the difference between two values stored in the counter, one generated before and the other generated after a clocked interval, with the associated conversion constant. Wind speed measurement with this arrangement is accurate to  $\pm 2\%$  over the range of 5 m/s to 60 m/s. For application in the field measurement campaign, the absolute accuracy of the wind speed measurement within the stated range or lower is not essential, as the measurement is primarily used to indicate period of light air, moderate breeze and strong breeze.

For completeness, the wind direction measurement is briefly discussed. The wind direction sensor consists of eight reed switches mounted radially at equal intervals. These switches connect a voltage divider resistor to the pull-up inputs of a 1-Wire quad ADC. As the wind rotates the wind vane, a magnet mounted on a rotor that tracks the rotation opens and closes one or two of the reed switches. When a reed switch closes, it changes the voltages seen on the input pins of ADC. Since the wind vane produce unique 4-bit signals from the ADC, all 16 compass directions can be measured.

#### **3.4.4 Temperature Measurement**

The millimetre-wave radio receiver tends to be exposed to strong wind and solar loading, which changes the temperature within the radio enclosure. As a result, the gain of the amplifier and mixer stage will vary, thus affecting the measured millimetre-wave signal. Similar to the rainfall rate data, the temperature measurement serves as a site-specific indication of changes in the ambient temperature, and not an absolute reading. This limitation arises due to the fact that the sensor is sited inside the housing of the weather station. It is therefore subjected to similar temperature loading issues, that is likely to be different to that of the radio receiver.

Ambient temperature is measured with a 1-Wire digital thermometer. This self-contained sensor measures temperature as the difference between two oscillators, one of which is temperature dependent. The sensor provides an accuracy of  $\pm 0.5$  °C over  $-10$  °C to  $85$  °C.

### **3.5 Data Acquisition Module for Weather Station**

The DAM that was built for the satellite STB is retained for use with the meteorological measurement. Modification was made to match the 1-Wire weather station interface and enables acquisition of the meteorological data. In use, the DAM reliably carries out what it was designed for.

#### **3.5.1 1-Wire Bus Specifications**

The 1-Wire weather station is a highly cost-effective set up due to among other, its use of the Dallas Semiconductor 1-Wire technology [96]. To access the sensors data, the bus design and protocol need to be understood.

The 1-Wire bus is a simple signalling scheme that performs two-way communications between a single master and peripheral devices over a single connection. Data transfers are half-duplex and bit sequential using short and long time slots to encode the binary ones and zeros. Parasite power is derived by the devices from this single bus line. Each device also has a unique code that identifies it to the bus.

The first part of any communication involves the bus master issuing a reset which synchronizes the entire bus. A slave device is then selected for subsequent communications. Once a device is isolated for bus communication the master can issue device-specific commands to it, send data to it, or read data from it. Because each device type performs different functions and serves a different purpose, each has a unique protocol once it has been selected. This 1-Wire bus protocol, including detailed commands and time slot requirements is provided in the individual device datasheet.

#### **3.5.2 DAM Design Requirement**

Interfacing to the 1-Wire weather station is carried out via a standard RS-232 port. However, this present port is already in use as the user interface to communicate with the DAM. Since the microcontroller only has one UART which handle the RS-232 communication, some means of software emulation will need to be developed in order to create another interface.

The meteorological data that are to be acquired from the weather station consist of a total of 15 bytes, comprising 14 data bytes plus one reply byte indicating proper 1-Wire operation. Breakdown of each meteorological parameter and the physical storage space that it requires is given in Table 3-3.

Meteorological parameter	Number of bytes
Rainfall	4
Wind speed	4
Temperature	2
Wind direction	4

**Table 3-3: Breakdown of meteorological parameter data bytes.**

Due to the typical integration time of 1 minute for rainfall rate measurement, the acquisition rate requirement can be significantly reduced compared to acquiring the received IF signal parameter data. At a chosen acquisition rate of 10 s, the 32 Mibytes SmartMedia used in the DAM could easily store over half a years worth of continuous data. These weather conditions will also need to be automatically logged with a timestamp, so that the signal measurement results can be exactly correlated to the weather conditions under which the measurements were made.

### 3.5.3 Weather Station DAM

The only hardware modification to the SmartMedia based DAM involves a simple extra RS-232 port connection to the RTS and CTS line originating from the I/O pins of microcontroller. These lines will generate the RS-232 transmit and receive signalling through software emulation. The components layout, and the hardware addition indicated by the shaded block, can be seen in Figure 3-28.

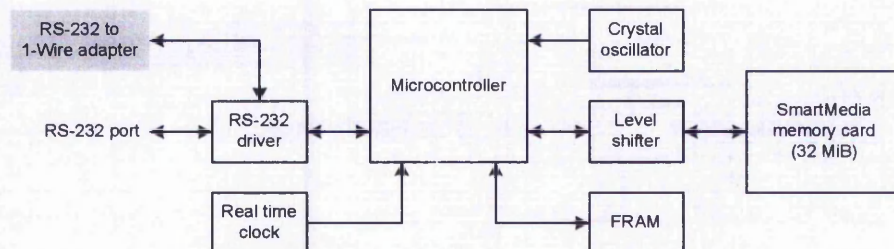


**Figure 3-28: Weather station DAM components layout.**

The RS-232 driver now does the voltage level translation for two RS-232 interfaces. Control and acquisition of the weather station data is carried out via the hardware UART while the software UART handles the user communication.

#### **3.5.4 Assembly Language Program for Weather Station DAM**

The assembly language program flow written for the SmartMedia based DAM is reused by replacing calls to the I<sup>2</sup>C routines with that of the RS-232 to 1-Wire routines. This modified program flow is shown in Figure 3-29, with shaded blocks representing the new subroutines.

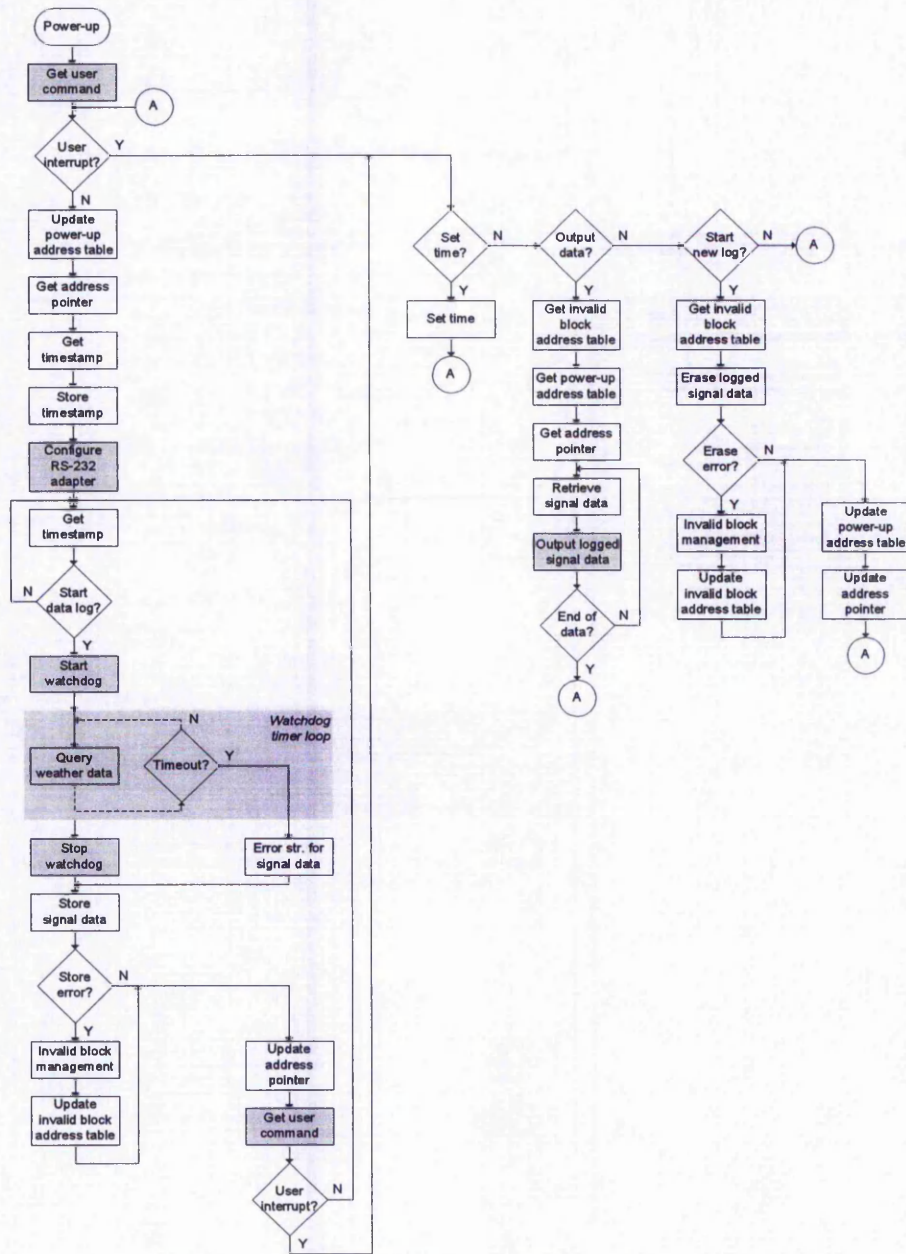


Figure 3-29: Weather station DAM program flowchart.

After start-up, the DAM will go through the initialisation process. This includes configuring the RS-232 to 1-Wire adapter. The following delay loop then generates the 10 s interval between successive data reads.

The routine for acquiring the meteorological data draws on the hardware RS-232 routines to relay the command and data to and from the weather station. This acquisition process is carried out inside a watchdog timer loop that is running concurrently in the background. The loop serves as a fail-safe feature to ensure that in the event the weather station does

not respond, the program flow will not stick in the acquisition phase, but timeout with writing a known error string to the SmartMedia memory.

Other changes include using a software RS-232 routine to replace the occupied hardware version that formerly handles the communication of the user interface. These latest subroutines are as listed in Figure 3-30.

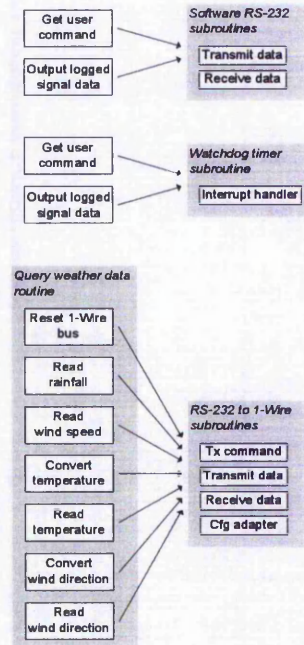


Figure 3-30: Weather station DAM program additional subroutines.

### 3.6 Fade Simulation System

The calibration process for the signal measurement system requires a stable signal source which is similar to what it is meant to measure, and a means of degrading this signal source in a known calibrated way. A fade simulation system was therefore developed to address these requirements. The FSS is envisaged to provide a signal whose power level can be dynamically specified by providing the system with a fade profile to follow. For the calibration purpose, a ramp function can be applied to successively degrade the signal.

Since the FSS enables simulation of any fade profile, it can also be used for hardware testing of potential fade detection and mitigation algorithms. Deep fading on a real link is rare with large inter-event period and each event is different. By recording these events, the FSS can easily simulate them as required, dropping the impractical need to perform such tests on a real link.

#### 3.6.1 FSS Design Requirements

Design of the FSS can be reduced into three functional blocks. The first of these provides the stable signal source. This signal source is then fed to an attenuation block which must allow control over the degree of attenuation. The final functional block consists of the user interface, which is required to receive the user specified fade profile and manipulate the attenuation block. Figure 3-31 depicts the adopted top-down design approach for the FSS.

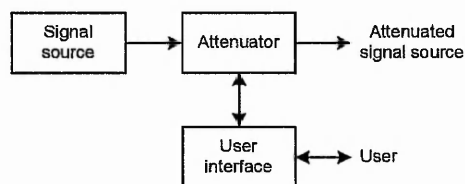
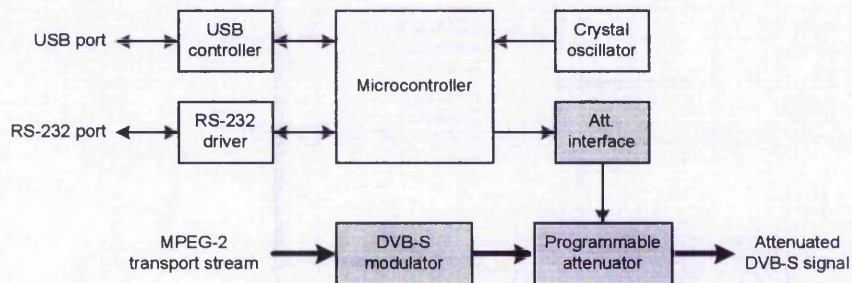


Figure 3-31: FSS top level block diagram.

The stable signal source takes the form of the upconverted digital video multiplex signal, adhering to the DVB-S scheme at a carrier frequency of 1.66 GHz and symbol rate of 17.5 Msymbols/s. Output from the FSS must cover the measurement range of -20 to -80 dBm possible with signal measurement system. Across this range, the accuracy of the power level must be known.

### 3.6.2 FSS Hardware Development

The signal source is obtained by re-modulating an available MPEG-2 TS. The resulting signal is of known, stable amplitude with large C/N. Attenuation of the signal is provided by a pin switched programmable attenuator, with an attenuation range of 63.75 dB in steps of 0.25 dB and a fast maximum switching time of 2  $\mu$ s. The programmable attenuator is supplied with a built-in interface which accepts control signals to activate or deactivates a particular attenuation cell. Figure 3-32 illustrates the layout of these two pieces of equipments in relation to the other components.



**Figure 3-32: FSS components layout.**

Input of the fade profile data is carried out using a PC which interfaces to the FSS via a USB link. This data is in the form of magnitude of attenuation, from 0 to 63.75 dB, and duration of the attenuation from multiples of 10 ms right up to a maximum of 255 s. The combined components are also sufficiently fast to receive and execute the real-time fade profile originating from the PC. Apart from auxiliary I/O header pins, the system also includes a general purpose RS-232 interface. These interfaces are envisaged to provide flexibility for the system in controlling other external hardware such as providing a synchronising signal.

The controller and interfacing components are mounted on a two-layer PCB board fabricated in-house. Figure 3-33 is a photo showing the FSS in use to calibrate the satellite STB on the far right.



Figure 3-33: Photo of satellite STB calibration via the FSS.

### 3.6.3 Assembly Language Program for FSS

The FSS requires a simple assembly language program flow as depicted Figure 3-34.

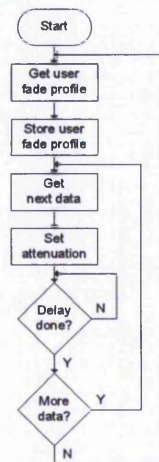


Figure 3-34: FSS program flowchart.

Upon start-up, the FSS will wait for user input of the fade profile data in a predetermined format. Each individual pair of attenuation level and delay data is then retrieved. The attenuation level is set accordingly by manipulating the microcontroller I/Os which fed the programmable attenuator. The program flow then enters a delay loop and maintains the

current attenuation level for the duration required. This process is then repeated until all the available fade profile data has been executed.

### 3.6.4 FSS Calibration Results

The FSS is calibrated to determine the output accuracy of its signal within the range of -20 to -80 dBm. A power meter is used to determine the level accuracy of the incrementing attenuation given by the system. Calibration results for the first half of this range is shown in Figure 3-35. The plot of residuals indicates that the maximum deviation from the expected values is within  $\pm 0.4$  dB. This error will need to be accounted in the event that the FSS is used for calibrating other hardware.

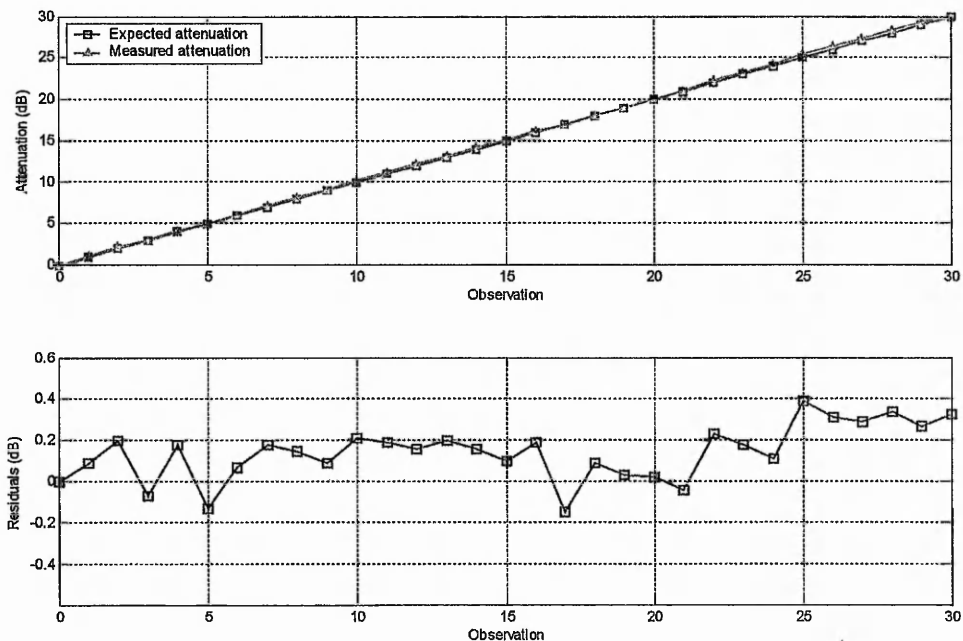
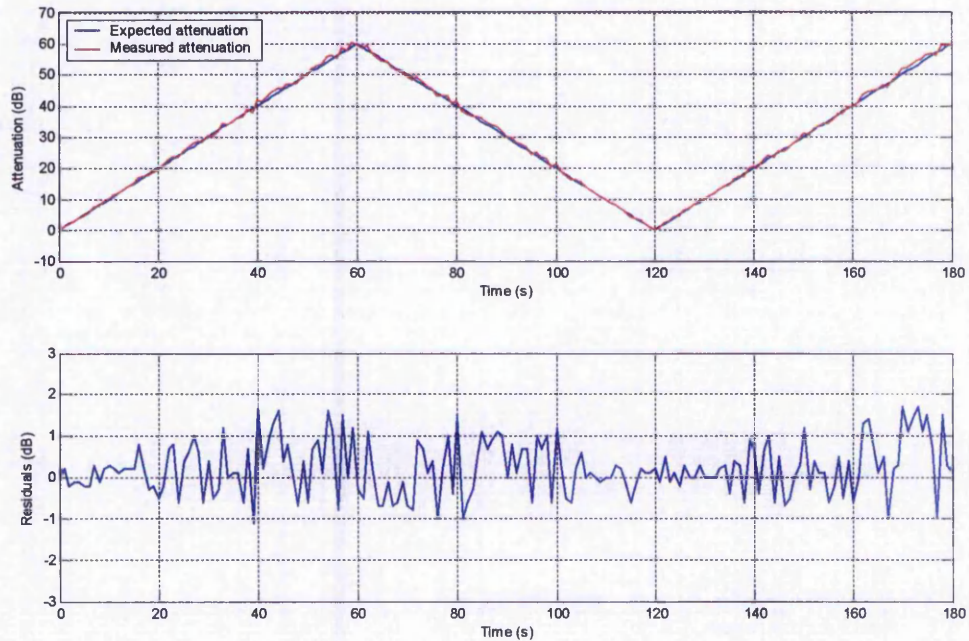


Figure 3-35: FSS calibration result.

Figure 3-36 demonstrates the response of the FSS in generating an up/down-ramp fade profile. Measurement in this instance is done with a spectrum analyser measuring the channel power. Results of the measurement are stored in real-time to a PC via a GBIP interface using a written LabView program. A larger spread is apparent in the residuals but this is to be expected due to the increased measurement inaccuracy of the spectrum

analyser compared to the power meter. Nevertheless, the plot clearly demonstrates that the FSS can generate the necessary fade within the range of interest.



**Figure 3-36: FSS response test.**

### 3.7 Summary

A cost-effective measurement system for both the millimetre-wave signal parameters and weather condition has been developed. This can then allow an extended number of measurement sites. The signal measurement system consists of a custom built DAM which acquires and stores the various measured signal parameters from off-the-shelf satellite STB. Relevant investigation and calibration tasks have been undertaken to determine and verify that measurements via the satellite STB are accurate and (have since been proven in the field to be) reliable. Each developed signal measurement system costs below £130.

The developed meteorological measurement system utilises a low cost weather station to measure rainfall, wind condition, and temperature, along with a modified version of the earlier DAM to acquire and automate logging of the relevant data. The total hardware and components cost is £150.

The feasibility of the FSS system could enable automatic calibration of the numerous signal measurement systems and simulate any fade profile for hardware test of potential fade detection or mitigation algorithm.

## Chapter 4

# Identifying changes in the local mean

The clear-air local mean level of the monitored received signal power varies primarily due to changes in the temperature loading on the millimetre-wave radio ODU. This variation needs to be accounted for when conducting a long-term field measurement, as it alters the baseline level from where the fade statistic is derived. A mitigation method in the form of a novel use of iterative cumulative sum (CUSUM) analysis with associated randomisation test, was developed to detect when these multiples changes in the local mean occur in the monitored data, so that significant local mean levels can be identified and used in place of the baseline level.

Software implementation of the proposed algorithm is then tested on a simulated and actual field measured dataset. Both results indicate that the fundamental changes in local mean can be detected, and statistical analysis using the latter dataset shows a more accurate unbiased derived fade statistic.

## 4.1 Changes of Local Mean in Long-Term Measurement Trial

Long-term fixed wireless measurement trials at millimetre-wave frequencies that are undertaken generally involve a highly controlled environment for the radio subsystem. A typical practise comprises shielding the radio within an environmentally controlled enclosure with the antenna radiating outwards thru clear perspex layer [97].

In contrast to these highly controlled trials, the campus network trial [15] focuses on maximising the deployment of measurement monitoring sites, through the use of off-the-shelf equipment and in a real live network which is providing services. As the aim is to study the millimetre-wave links in an actual deployment scenario, the installed radios are thus not environmentally shielded. In addition to that, the cost involved in doing so will be impractical for the trial purpose. However, any influence that could then arise to bias the trial's measurements itself needs to be properly understood, with the necessary mitigation method analysed in order to ensure that the measurements are as accurate as possible.

### 4.1.1 Radio Subsystem Gain Variation

In order to increase coverage, the millimetre-wave radio ODU is (obliged to be) sited at high elevation, increasing its exposure to strong wind and solar loading. Consequently, the gain of the amplifier and mixer stage varies somewhat as the temperature within the radio enclosure changes. The variation for such a subsystem can be as high as  $-0.035 \text{ dB/}^\circ\text{C}$  [98].

An example of this temperature induced gain deviation is shown in Figure 4-1. The measured temperature is obtained from a locally sited weather station, close to the user-end radio receiver. There is no observed or recorded rainfall (which attenuates the received signal) across the 7 days presented in the example. Thus, the diurnal variation in the millimetre-wave signal which tends to be more attenuated during the latter half of each day can be attributed to the rise in the afternoon temperature.

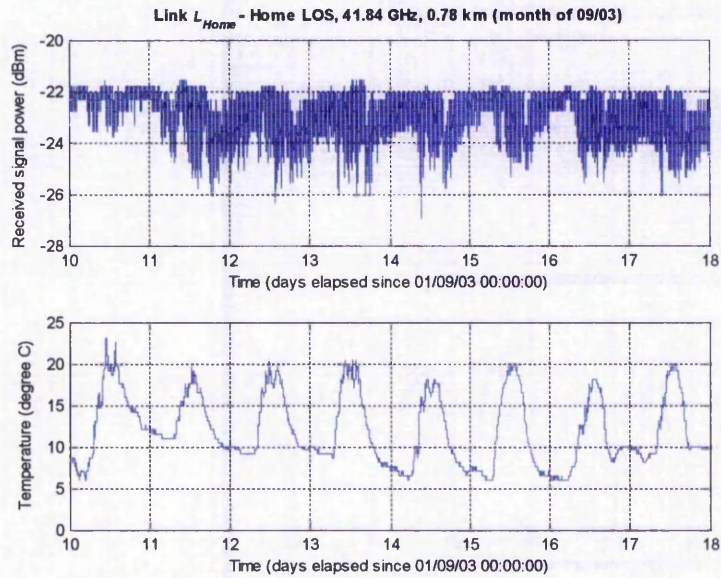


**Figure 4-1: Temperature induced gain variation of user-end radio receiver.**

Figure 4-2 illustrates another probable (and interesting) scenario of a temperature induced gain variation on a relatively more stable user-end radio transceiver on the 19<sup>th</sup> and 20<sup>th</sup>, which is two consecutive clear-air days following heavy snowfall, and shower and snow the day after. During this time, the gradual variation of the received signal power by 2 dB over an interval of 14 hours can be seen to somewhat trace the measured change in ambient temperature at the base station radio transceiver.

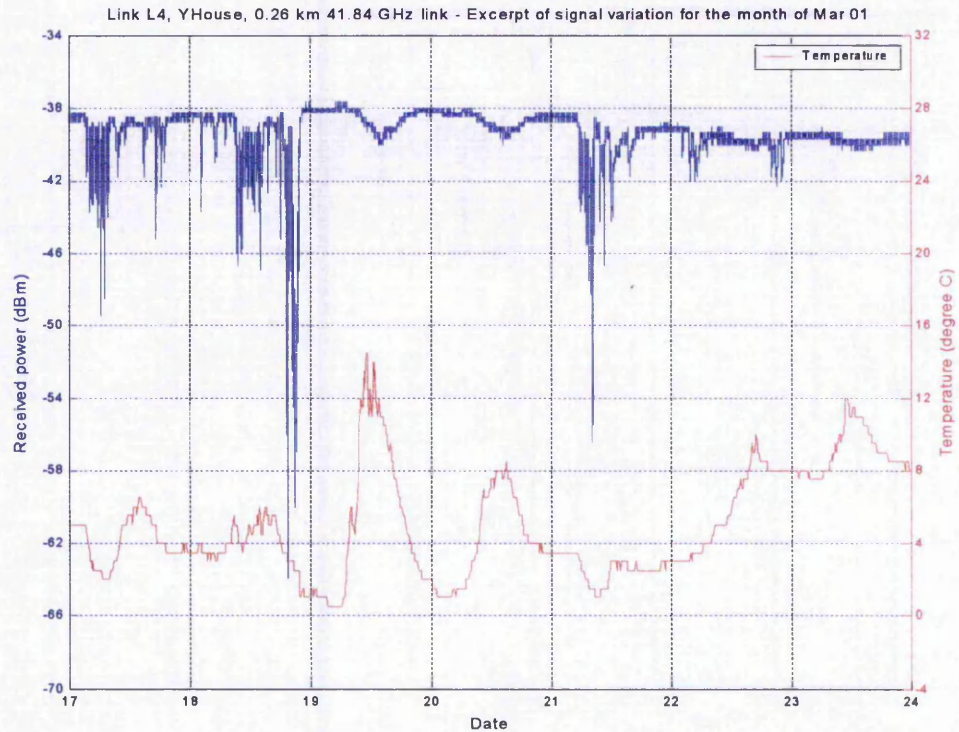


**Figure 4-2: Temperature induced gain variation of user-end radio transceiver.**

Accelerated aging test have shown that constituent components of the millimetre-wave radio such MMIC amplifiers will suffer degradation in RF gain over time [99]. Therefore, apart from the influence of temperature, component aging will also attribute to the change in the millimetre-wave radio overall gain, albeit at a significant slower rate, but typically involving a permanent shift in gain. While the change in gain due to component aging might not be apparent in comparison to the more dominant effect of diurnal temperature variations, its influence will need to be accounted for since the field measurement campaign is carried out over a long-term time period.

#### 4.1.2 Effect of Varying Local Mean

The conventional approach for deriving fade statistic in wireless communication adopts a defined baseline level from which the fade at any time is calculated by taking the difference of the instantaneous received signal power from the said level. This baseline level is the expected average received signal power during clear-air condition, which can be estimated from the link budget and confirmed with an on-site measurement. The final

value settled upon is usually a compromise to ensure that the received signal power during periods where there is no fade event will drift around the chosen level.

However, this approach of deriving fade statistics is not suitable for measurements spanning a sufficiently long duration, such that there could be significant temperature change to influence the gain of the radio subsystem. For example, measurement covering several days will tend to exhibit a lower local mean during the warmer period of the afternoon compared to a higher local mean during the colder period at night. Similarly, on a larger time scale, measurement running for several years will experience a more extreme variation in the local mean with changes in season and components aging.

Furthermore, the primary source of fade event on a LOS terrestrial millimetre-wave radio link is due to precipitation attenuating and scattering the transmitted signal. The onset of rain generally results in colder ambient temperature, which suggests that the gain of the millimetre-wave radio could possibly increase as temperature drops. Consequently, a higher than expected local mean could be present during the precipitation fade event.

Figure 4-3 is the plot of the received signal power during the month of December for a sample data set of a typical site, along with the recorded rainfall rate. The plot from the middle of the 20<sup>th</sup> onwards seems to suggest that the local mean for this particular data segment have shifted upwards. If the originally determined baseline level of -20.5 dBm (from on-site measurement under clear-air condition) is used to derive the fade during this period, the result obtained will underestimate the actual fades that have occurred.

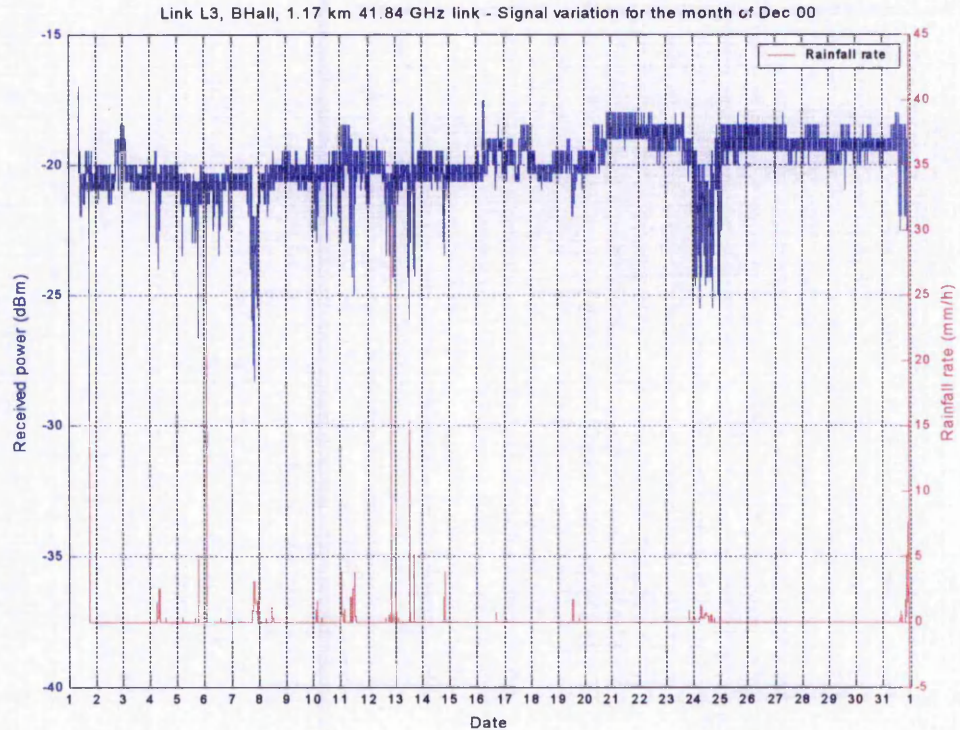


Figure 4-3: Received signal power variation for a typical site.

#### 4.1.3 Characteristic of Measured Data

In order to solve for these changes in the local mean, the characteristics of the observed received signal power data and the varying nature and fade profile that it exhibits need to be understood.

During transmission, the millimetre-wave signal will be modified by the various processes encountered arising from the propagating channel (see Section 2.4), of which the attenuation and scattering from precipitation events being the most dominating factor, in terms of reduction in the received signal power. These precipitation events, along with the effect of varying local mean, will introduce a fade profile to the received signal. In addition, the received signal is further modified by additive noise at the receiver which arises from the environment and radio components [36]. This noise is, under the standard assumption, additive white Gaussian noise (AWGN) [100]. The down-converted received IF signal that reaches the measurement system is therefore characteristically noisy, with a varying fade trend.

The final dataset is obtained by converting the logged AGC values from the satellite STB with reference to a calibrated look-up table. Usage of a look-up table implies that the actual continuous signal is quantised, first by the discrete AGC steps and followed by the calibration step size.

All these stated factors contribute to a measured received signal power data that intermittently fluctuate between the calibrated step sizes. These fluctuations need to be acknowledged as they are essentially noise and do not contribute any extra information to the data itself. If the measured received signal power is the only available information, any fade profile that is shown cannot be assumed to be attributed to precipitation fade event. The correct approach necessitates correlating this data with the recorded rainfall and measured fade profile data at different sites. Without these ancillary data, any fade profile that appears will have to be dismissed as possible random glitches.

#### 4.1.4 Local Mean Problem Statement

The problem statement for the changes in the local mean is defined using an extract of a rain fade event on the 24<sup>th</sup> from the dataset in Figure 4-3. A more accurate fade statistic can be obtained by suitably splitting the data into separate segments characterised by its own local mean. Fade derivation is then via a similar manner, but with reference to the local mean instead of the baseline level. Figure 4-4 illustrates the data in the span of interest that have been divided into three segments, with the segment boundaries around the precipitation fade event.

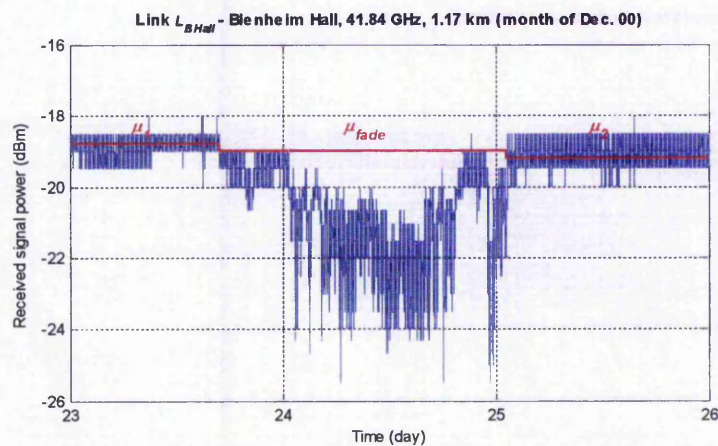


Figure 4-4: Data segmentation of a fade event.

The local mean of the fade precipitation event,  $\mu_{fade}$ , is given as

$$\mu_{fade} = \frac{\mu_1 + \mu_2}{2} \quad (\text{dBm}) \quad 4-1$$

where  $\mu_1$  is the average of the local mean prior  $\mu_{fade}$ , and,  $\mu_2$  is the local mean after.

The problem statement essentially equates to the identification of the points at which the change in the local mean occurs, which then allows the data to be suitably segmented at these points, and the local mean calculated. These points and local mean segments will then serve as a very powerful aid, in identifying and deciding on significant local mean levels that will be used to derive the final fade statistic.

While it is plausible to visually inspect and manually segment the data, the amount of work in carrying this out on the large collection of field trial data will be extremely tedious. More importantly, the decisions made visually will tend to be highly subjective and therefore unlikely to be repeatable. The solution to identifying these changes in local mean thus necessitates an algorithm that can be automated and highly repeatable.

## 4.2 CUSUM Analysis of a Single Change in the Local Mean

The occurrence of multiple changes in the local mean within the long time series of monitored received signal power data can be resolved by looking first at the simplest fraction, that which consists of a range of data which undergoes a single change in the local mean.

There are various methods available for detecting this single change in the time series. These can be loosely categorised into three classes; namely (i) gradient techniques, such as filtered derivatives, (ii) statistical techniques, such as generalised likelihood ratio test, and (iii) signal modelling techniques, such as autoregressive (AR) and autoregressive moving average (ARMA) based methods [101, 102]. The ordinary gradient techniques are fastest, but tend to be less reliable in the presence of random noise. Both statistical and signal modelling techniques on the other hand, deliver better performance, but at the expense of significant computational overhead.

However, the problem is by no means solved since the majority of change-detection algorithms developed are parametric based. In other words, these algorithms employ a design or stopping rule based on knowledge of the underlying statistical distribution of the data, knowledge which is not readily available for the observed received signal power data.

A promising distribution free approach, in the form of the CUSUM algorithm, can be used to analyse the data, by detecting a departure in the mean from its initial condition, as used in industrial process monitoring [103]. The point where the mean changes, or change-point, can then be statistically inferred from the CUSUM using likelihood-type estimates [104]. Alternatively, the application of resampling methods using bootstrapping to solve for the change-point has been demonstrated [105]. A further resampling method approach via randomisation, has also been described [106] for detecting trends in the distribution of a variable in environmental monitoring.

Building on these ideas, the change in the local mean can be identified through combining the use of the CUSUM algorithm to infer the change-point, and the associated randomisation test to determine its significance. An overview of the proposed algorithm to detect and identify this single change in the local mean is presented in Figure 4-5. Detailed explanation for each relevant stage is covered in the following few sections.

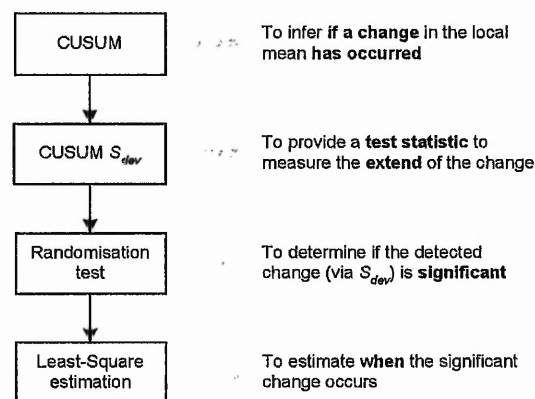


**Figure 4-5: Overview algorithm flowchart for single local mean change identification.**

### 4.2.1 Monitored Data as Mean-Shift Model

This local mean change in the dataset can best be modelled based on the notion of splitting the data into two segments at the change-point. One suitable choice is the mean-shift model.

Let the observed received signal power data be represented by the time sequence  $x_1, x_2, \dots, x_n$ . The monitored data can then be represented by the mean-shift equation

$$x_t = \begin{cases} \mu_1 + \varepsilon_t & (t = 1, \dots, \tau) \\ \mu_2 + \varepsilon_t & (t = \tau + 1, \dots, n) \end{cases} \quad 4-2$$

The data segment of time 1 to  $\tau$ , and  $\tau+1$  to  $n$ , is the index that represents the data points prior to and after the mean has changed. Each data segment is in turn characterised by its own local mean,  $\mu$ . In the mean-shift equation, the local mean of the two data segments,  $\mu_1$  and  $\mu_2$ , are defined as

$$\begin{aligned} \mu_1 &= \frac{\sum_{t=1}^{\tau} x_t}{\tau} \\ \mu_2 &= \frac{\sum_{t=\tau+1}^n x_t}{n - \tau} \end{aligned} \quad 4-3$$

From Equation 4-2,  $\varepsilon_t$  is the random error associated with the time  $t$ -th value, and is independent and identically distributed (i.i.d.). This assumption is supported by the data itself [100] and is essential for justifying the latter statistical inference. Thus, at each sampling interval, the received signal power data,  $x_t$ , is statistically independent, has a local mean  $\mu$  and an associated i.i.d. error  $\varepsilon$  due to noise.

### 4.2.2 CUSUM Method

CUSUM schemes were initially developed for industrial process control [107], and have since become a standard tool in that area [103]. The basic idea is that if the deviation of the monitored data from a baseline level are accumulated over time and plotted, then any systematic differences from the baseline level will be more (visually) apparent than would be the case if the deviation is plotted individually. The CUSUM method has been shown to be sensitive to small shifts in the monitored mean and reasonably robust to outliers [103], which is suitable for the time-varying nature of the data local mean.

The CUSUM is the cumulative sums of differences between the data values and their overall mean. Construction of the CUSUM chart involves calculating the summation of the difference between the current data point,  $x_t$ , and the overall mean,  $\mu$ , over the entire data range,  $n$ , as given by the following equation

$$S_t = \sum_{t=1}^n (x_t - \mu) \quad 4-4$$

where

$$\mu = \frac{\sum_{t=1}^n x_t}{n} \quad 4-5$$

Equation 4-4 can be written in a recursive form as

$$\begin{aligned} S_0 &= 0 \\ S_t &= S_{t-1} + (x_t - \mu) \end{aligned} \quad 4-6$$

which lends itself to easier algorithm implementation. The CUSUM chart is then a plot of  $S_t$  against  $t$ .

The theoretical background and statistical properties of the CUSUM algorithm have already been thoroughly covered in previous literature [103], and as such will not be repeated here. Instead, Figure 4-6 is used to illustrate some possible CUSUM patterns that might be obtained and their interpretations.

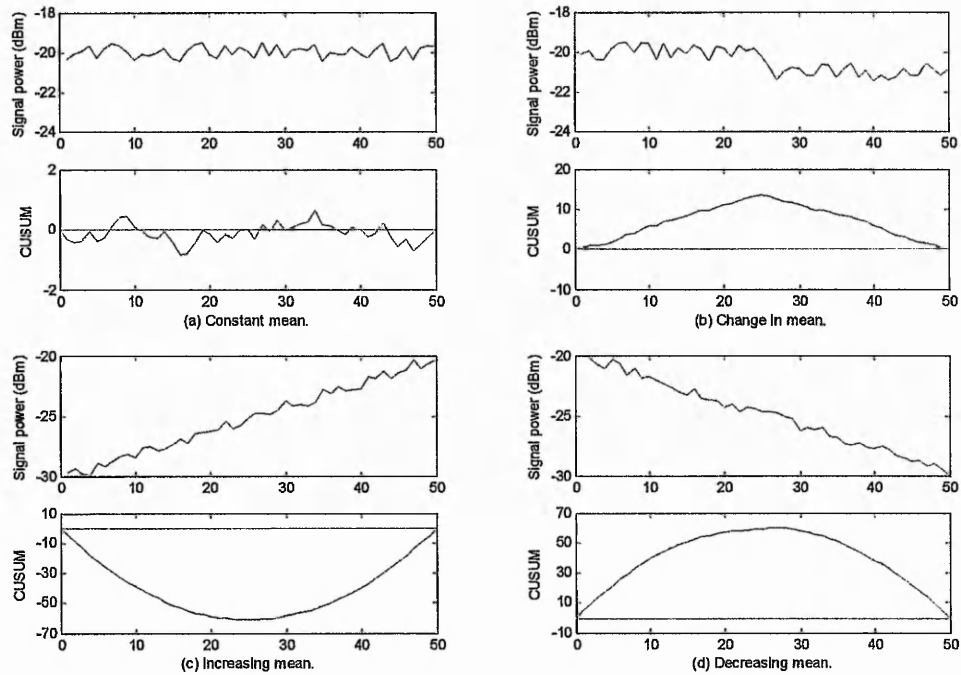


**Figure 4-6: Possible CUSUM chart variations.**

Visualisation of trends or changes in mean in the data is amplified by the CUSUM function as the chart indicates the manner in which the monitored data differs from the overall mean. As  $x_t$  is statistically independent, Equation 4-6 clearly shows that the process  $S_t$  will randomly wander about the mean. Hence, periods where the local mean of the data did not change will result in a CUSUM that follows a relative straight path during that period, as indicated in Figure 4-6 (a).

If there is a step change  $\delta$  increase in the mean, there will be a step shift upwards of  $\delta$  in the quantity added to the CUSUM for each additional data point. Thus, an increase in mean is identified on the CUSUM chart as an upward slope, where the values for that time period tend to be above the overall mean.

Data sequence with a monotonically increasing local mean will thus produce CUSUM defined by a positive parabolic curve. Conversely, a negative parabolic curve is true for a monotonically decreasing sequence. Figure 4-6 (c) and (d) gives the respective plots for each of these states.

The property of interest is when a sudden change in direction of the CUSUM chart occurs, as this indicates a sudden shift or change in the local mean. If the mean shift downwards, the corresponding change-point will appear as a peak on the chart, as depicted in Figure 4-6 (b) (or as dip if the reverse is true).

The disadvantage of using the CUSUM method is that the CUSUM chart requires considerable skill to interpret visually, even with aids such as V-Mask [103]. A CUSUM data analyst essentially learns by experience and by developing case laws. Therefore, to facilitate the automation of interpreting the CUSUM chart, it is helpful to have an idea whether it is significant in the sense that the chart obtained is unlikely to have occurred by chance alone. A change in mean that is detected by a CUSUM that tested significant will, by implication, be significant itself.

#### 4.2.3 Randomisation Test

A randomisation test assesses the hypothesis that a given pattern that appears in a sequence of data is random versus the null hypothesis that the pattern occurs by chance. A test statistic  $S_{test}$  is chosen to measure the extent to which the data shows the pattern in question.

The result of  $S_{test}$  for the observed data in its original time series sequence, denoted here as  $s$ , is then compared with the distribution of  $S_{test}$  that is obtained by performing many random permutations on the data. The argument made is that if the null hypothesis is true, then all possible orders of the data were equally likely to have occurred [108]. Hence, the observed data pattern will just be one of the equally likely patterns and  $s$  should appear as a typical value from the distribution of  $S_{test}$ . If this does not seem to be the case then the null hypothesis is discredited to some extent and, by implication, the alternative hypothesis is considered more reasonable.

Therefore, in this instance,  $s$  is significant. The significance level of  $s$  is the proportion of values equal to or more extreme than  $s$  from the randomisation distribution. For 1000 random permutations, a level of 5 % or less is typically adopted to interpret that the null hypothesis is not true [108].

Justification for using randomisation test lies in the assumption that the mechanism generating the logged data needs to be such as to make the observed value equally likely to have occurred at any position in the time series. For the intended application of monitoring the received signal power, the use of randomisation is thus justified since the data being analysed is statistically independent, as each data has an associated random value due to noise [100].

#### 4.2.4 Significance of CUSUM Plots

The usual estimate of point of change in mean is the index of the maximum deviation of the CUSUM from zero [104]. This maximum deviation, defined as

$$S_{dev} = \max_{t=0, \dots, n} |S_t| \quad 4-7$$

will form the test statistic used in the randomisation test to determine the significance of the CUSUM chart.

The test for significance involves constructing a large number of randomised CUSUM charts, where for each one of these the received signal power data are randomly permuted. For each random sample,  $S_{dev}$  is obtained.

The significance of the original CUSUM chart with the data in the correct order, is indicated by the percentage of time its test statistic is exceeded with the randomised data. As previously stated, if the original CUSUM  $S_{dev}$  value is exceeded by 5 % or less of randomisation, then this is an indication that there is a real significant change in the mean level that can't be easily attributed to chance.

### 4.2.5 Least-Square Estimation of Change-Point

Following the detection of a significant change, an estimate of when the change occurs can be made. From the mean-shift modelling of Equation 4-2, the received signal power data is essentially split into two segments, one on each side of the change-point. The choice of where to split the data is based on how well the mean of each newly created segment fits the mean-shift model.

The required change-point estimator,  $\hat{\tau}$ , is consequently a least-square estimator, which is to say that

$$\hat{\tau} = \min \left\{ t : \sum_{t=1}^{\tau} (x_t - \mu_1)^2 + \sum_{t=\tau+1}^n (x_t - \mu_2)^2 \right\} \quad 4-8$$

Value of  $t$  that minimises  $\hat{\tau}$ , is the best estimator of the last point before the change in mean,  $\tau$ . It follows then that the point  $\tau + 1$  estimates the first point after the change.

## 4.3 Iterative CUSUM Analysis of Multiple Changes in Local Mean

Available literature [102, 104-106] on detecting change in mean are restricted to the problem of detecting a single change. The proposed iterative approach builds on the previous CUSUM algorithm, to detect multiple changes in the local mean of the received signal power data by repeating the same analysis for each newly created segment. This approach further introduces robustness to false change detection through the reassessment of all change-points detected. For this reason, there are two steps involved, namely detection and assessment.

### 4.3.1 Detection of Potential Change-Points

Change is detected as before, but the CUSUM analysis is then repeated for each segment. Multiple changes can then be detected by continuously splitting each segment into two new ones for any additional significant change found. However, a change that tested significant in its original segment might no longer prove significant if this segment is modified when a more significant change is detected latter on. In order to account for this possibility, all points found at this step are treated as potential change-points.

### 4.3.2 Reassessment of Change-Points

These change-points are then reassessed to eliminate those that test insignificant. The first and last point in the data are considered as significant change-points. Commencing from the first point, three successive potential change-points are obtained, with the aim of reassessing the significance of the middle change-point. Therefore, each potential change-point is assessed in the segment between the two nearest-neighbour potential change-points, including the first and last points as necessary.

The significance level of the change-point of interest is determined as before, within the constraint of the stated data segment. If the current change-point tests significant, the assessment continues on to the next potential change-point in the identification sequence. However, if a point no longer tests significant, the point is eliminated. Since this point was included in the previous evaluation, the apparent significance of the previous change-point is reassessed.

### 4.3.3 Local Mean Data Segmentation

Once all the significant change-points are identified, the original data can then be split up into multiple segments. As a consequence of the analysis done to obtain these segments, each segment is characterised by having a local mean which is significantly different from the neighbouring segments. Following segmentation of the data sequence, the next step will therefore be the derivation of the local mean value of each segment.

Depending on the length of the analysed data sequence, the number of local mean segments found can be potentially very large, as a consequence of the noisy nature of the measured received signal power which manifests as additional local mean levels of comparable magnitude. Therefore, as a first-order filtering exercise, any local mean segments that drop below a predefined threshold level can simply be replaced by the average of the local mean before and after the drop. The justification for this (and the choice of the threshold level) is that there is an absolute limit to the magnitude of drop in the local mean of the monitored signal due to temperature change. Under typical millimetre-wave transmission, only the occurrence of a fade event will bring the received IF signal below the defined threshold level.

### 4.3.4 Software Implementation of Proposed Algorithm

A custom software application is written in the Java programming language to perform the iterative CUSUM analysis on the collected measurement data. The program flow for the written software is summarised in Figure 4-7.

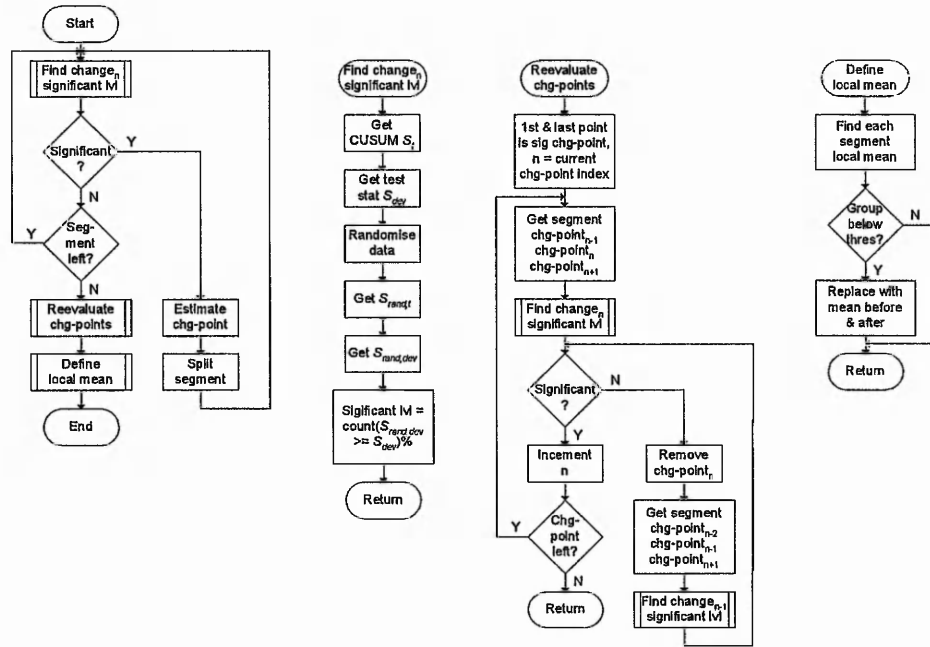


Figure 4-7: Iterative CUSUM analysis algorithm flowchart.

The change-points and local mean segments obtained from executing the implemented algorithm will aid towards identifying local mean levels that are significant, which is then eventually used in deriving the fade level of the processed data.

Due to the huge number of repetitive computations involved, the proposed iterative CUSUM analysis is highly computer-intensive. Running on a 2 GHz processor, a typical analysis cycle for a day long data sequence comprising of 86,400 data points takes approximately 7 minutes. For this reason, it is more practical to only use the analysis on data segments where manual distinction of significant change in the local mean is difficult or needs verifying.

#### 4.4 Hardware Test of Proposed Algorithm

The iterative CUSUM analysis is performed on a test dataset to examine how accurate the algorithm is in signalling a change in the local mean of the monitored data. This test data is obtained from the converted logged data of a satellite STB which is measuring the power of a real signal. The signal source in turn comes from the fade simulation system (FSS) that is provided with a mean profile to simulate shifts in the local mean of the signal. In order to keep the test as close as possible to the deployed signal measurement system in the campus network trial, the stable DVB-S signal source for the FSS is replaced with one that is received over the radio link. Figure 4-8 illustrates the hardware set up to generate the required test data.

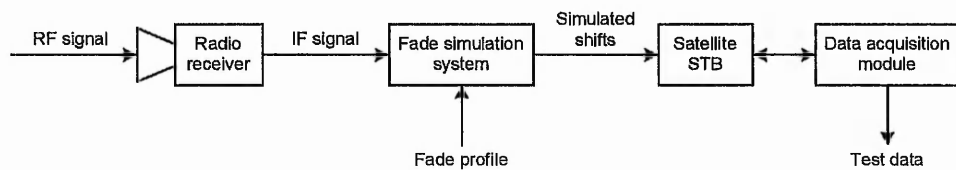


**Figure 4-8: Hardware test for iterative CUSUM analysis.**

The first set of test data simulates a signal under clear-air conditions which is experiencing minor shift in the local mean. Result of the iterative CUSUM analysis on this data shown in Figure 4-9.

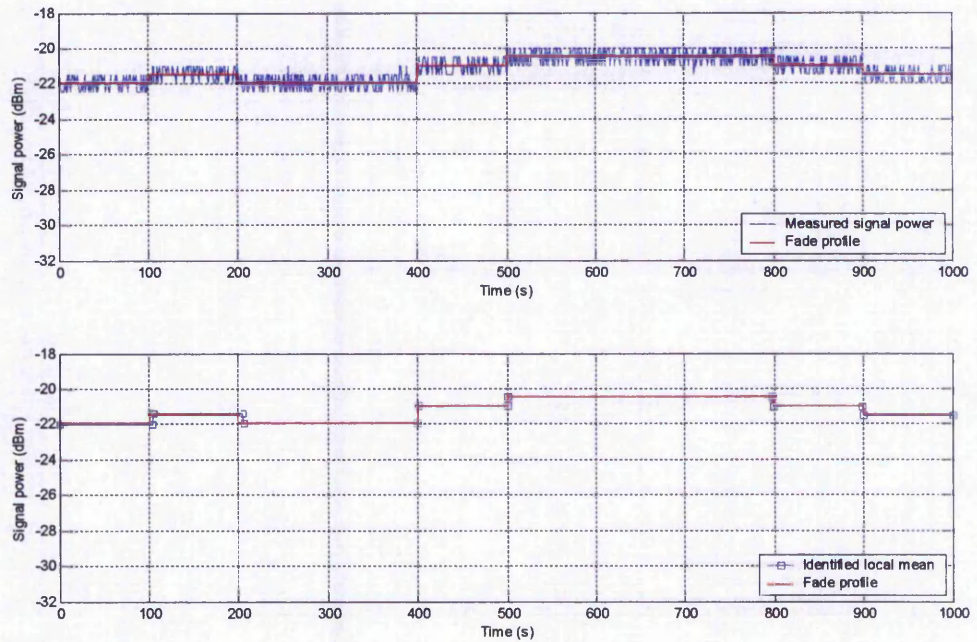


**Figure 4-9: Local mean detection test.**

Overall, the proposed algorithm could identify all the onset of change in the local mean of the simulated signal. The position of the detected change-points for each instant does not vary by more than 5 samples, in relation to the setting provided by the mean profile.

The second test involves reusing the same mean profile to maintain the fundamental local mean shifts of the previous test. However, both a fast deep fade and a shallow long fade event are introduced into the signal. The resulting measured signal is shown in Figure 4-10.

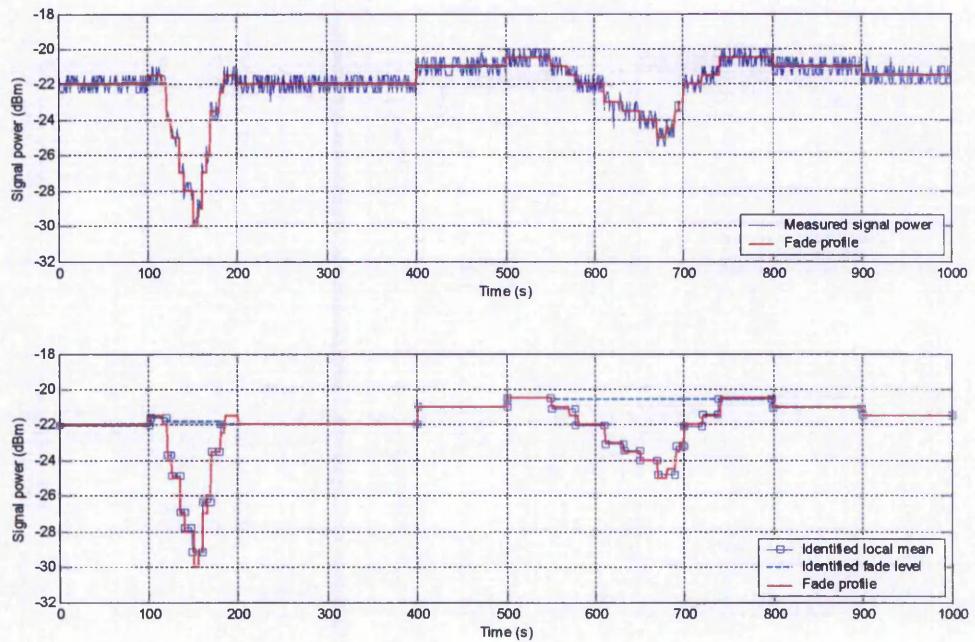


Figure 4-10: Local mean detection test in the presence of fade events.

These fundamental local mean changes were again identified by the developed algorithm. The plot of Figure 4-10 is also used to demonstrate that the change-points prior to and after a fade event can be employed unambiguously to specify the baseline level from which the depth of the fade can be derived.

#### 4.5 Power of Iterative CUSUM Analysis

While the developed algorithm has been demonstrated to be capable in identifying potential multiple changes in the local mean of the monitored data, the benefit and improvement offered to the actual derivation of fade statistics have yet to be assessed. To accomplish this, the statistical measure of fade non-exceedance is evaluated for the sample dataset reference in Section 4.1.2, using both the single baseline approach, and the multiple local baseline levels approach made possible with the algorithm. For the latter approach, changes in the local mean of the monitored signal that are significant need to be identified first. Figure 4-11 illustrates the detected local mean segments.

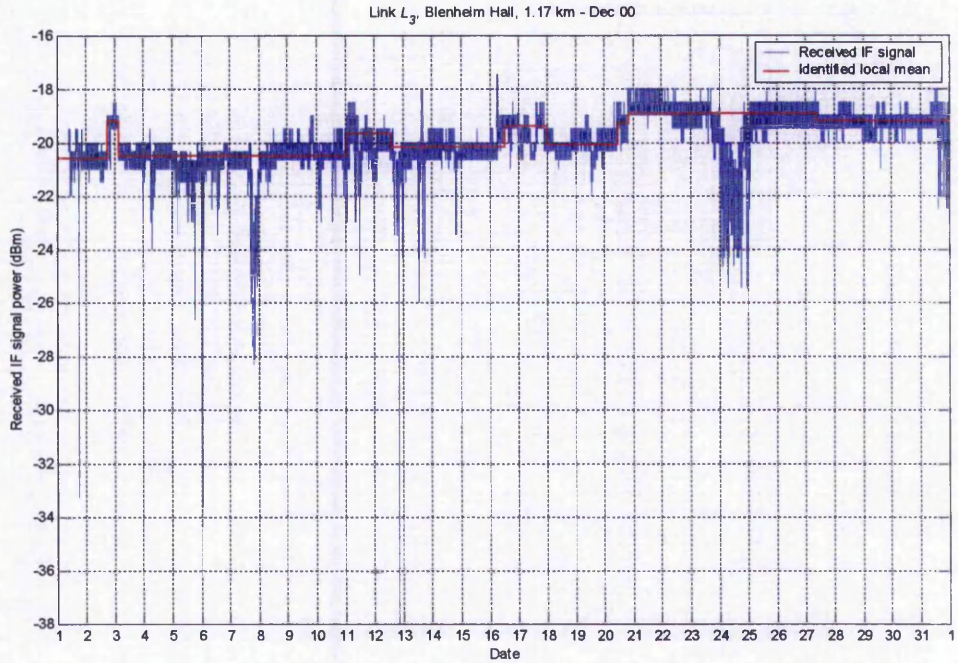


Figure 4-11: Identified local means from iterative CUSUM analysis.

The resulting fade depth cumulative distribution plots are shown in Figure 4-12.

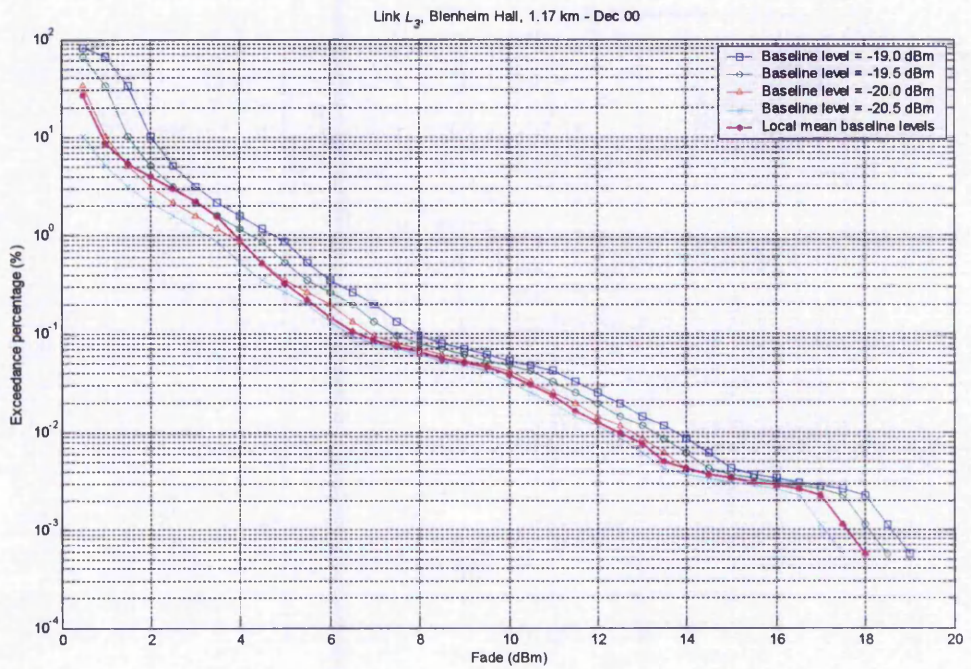


Figure 4-12: Variation of non-exceedance curves with baseline level.

Having acknowledged, from arguments put forward in the earlier section, that the multiple local baseline levels is the best representation of the data, the discussion need to be then focuses on the issue of inaccuracies in the fade non-exceedance statistic when derived with the single baseline approach.

For this particular millimetre-wave radio link from which the sample data set is obtained from, the link budget calculation indicates that the clear-air received IF signal power is approximately -18 dBm, whereas measurement conducted during installation of the receiver site yields a clear-air received IF signal power of -20.5 dBm. The fade non-exceedance curve using the link budget value as its baseline level is shown to overestimate the fade depth for all time. When the measured value is employed, the more crucial and rare deep fades were found to be underestimated by over 0.5 dBm. This plot also underestimates the many occurrences of small fades, which is expected as the local mean for a large segment of the sample data have shifted upwards relative to the used baseline level.

The non-exceedance curves for the in-between baseline level values are also plotted out. All these curves highlight the fact that the single baseline approach is not suitable for the form of monitored data, as the choice of baseline level values to use will greatly vary the resulting statistic. Therefore, in order to mitigate the effect of changes in the local mean of the monitored received IF signal power data, the iterative CUSUM analysis will be used in the ensuing analysis of the field measurement results.

## 4.6 Summary

The novel application of an iterative CUSUM analysis with associated randomisation test is implemented to mitigate the dominant effect of temperature loading on the millimetre-wave radio ODU, which varies the long-term local mean level of the monitored received signal power. This proposed algorithm provides an estimate of significant local mean levels that can be used to derive a more accurate fade values, in place of the conventional use of a single baseline level.

When the proposed algorithm is tested on a hardware-based simulated data, all the underlying local mean segments are effectively found. The proposed algorithm is further

verified through testing using actual field measurement data, where a more accurate derived fade non-exceedance statistic is shown to be achievable.

However, practical use of the iterative CUSUM analysis might need to be limited to data segments that are difficult to interpret manually, as analysing the entire (or a long) sequence of data increases the number of detected local mean due to noise, and incurs significant computational time.

## Chapter 5

# Analysis of Field Measurement Results

The extensive amount of field trial data accumulated from the long-term field measurement campaign of the modulated 42 GHz wideband millimetre-wave signal and supporting meteorological data, are analysed and presented, with the aim of addressing the lack of available long-term statistics and propagation information of the actual measured signal, and comparing the obtained results to prevailing measurements, predictions and models where available in the literature. Analysis of the field measured data was carried out within the specific context of long-term precipitation fade, propagation through foliage and spatial correlation in the distribution of precipitation fade.

Results for the long-term fade statistic of LOS links, uniquely covering consecutive years and multiple sites, indicate that the availability prediction given by the prevailing ITU-R model is not adequate and needs further improvement. Work has also been undertaken to compare and verify the available fade duration prediction model, and it has found the prediction model is reliable for the 42 GHz radio link. Prior to this, no known verification of this prediction model, apart from the author's own work, is in publication.

Study of the 42 GHz wideband signal propagating through foliage is also presented, under different combinations of meteorological conditions. The collected field data encompass a long-term measurement duration covering 6 months, of which over 100 days involve the in-leaf period. The statistical results and empirical modelling from this study are themselves unique as the measurement is conducted over a long-time scale previously unavailable.

In addition, the measured fade from two spatially separated radio links, in the study of spatial correlation in the precipitation fade distribution, shows the potential for diversity improvement.

## 5.1 Long-Term Fade Statistic

The literature review in Section 2.4.5 identified precipitation as the predominant attenuating factor for millimetre-wave transmission. Propagation through such a medium is characterised by considerable absorption and scattering of the millimetre-wave signal by raindrop particles, which result in an overall excess attenuation to the signal. An excerpt of the measured signal data taken from the monitored link  $L_{BHall}$  is presented in Figure 5-1, illustrating the effect of precipitation on a 1.17 km long, 42 GHz millimetre-wave link. Strong signal fade is evident during the intense rain event on the 7<sup>th</sup>, while sustained fade can be seen during the extended rain events on the 29<sup>th</sup> and 30<sup>th</sup>.

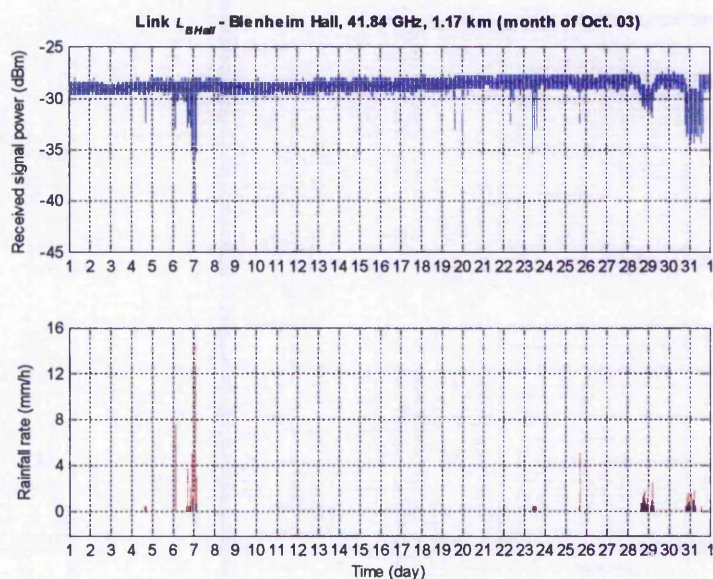


Figure 5-1: Effect of precipitation on the received signal power.

In the provision of services via MWS, a fade margin is typically allocated to mitigate the precipitation attenuation up to a certain threshold. Larger precipitation attenuation will thus result in outages in the service provision. Estimation of average annual system unavailability, due to precipitation attenuation, is generally determined from precipitation prediction models which reference a long-term statistical source of local rainfall rates [43].

While the attenuation effects of precipitation on radio wave propagation have been studied extensively, there is a lack of any long-term measurement of the millimetre-wave signal itself as it experiences fade due to precipitation. In particular, there is inadequate

measurement data to permit a proper comparison between the actual measured 42 GHz millimetre-wave wideband signal, and the available prediction models. Suitable long-term measurement campaigns are thus necessary in order to both validate and, if possible, improve on the prediction models.

### 5.1.1 Fade Non-Exceedance Statistic

Path profiles and details of the millimetre-wave radio links referenced in the ensuing analysis are given in Figure 2-12 and Table 2-1. The predicted annual statistics of precipitation attenuation for the each radio link are obtained according to the ITU-R P.530-9 [43] prediction model procedures highlighted in Section 2.5.2, which is then scaled to cover the percentage of time from 0.001 % to 1 %. Both ITU-R and RAL path reduction factor [72, 73] are included in the derivation using the prediction model. Results from the model are then overlaid over the measured data in order to verify the model's accuracy.

The long-term fade non-exceedance cumulative distribution (NECD) for link  $L_{BHall}$  spanning two consecutive complete years of 2002 and 2003, have been derived and compared with the predicted fade for all events, as shown in Figure 5-2 and Figure 5-3 respectively. The cumulative time recorded when the time series of fade data exceeds the determined threshold is normalised to the total sample time of the entire measured fade data time series.

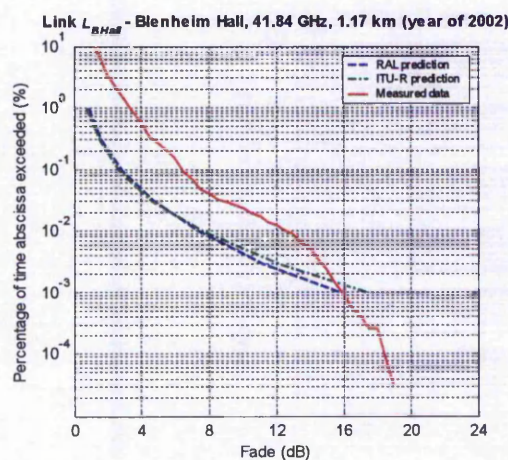


Figure 5-2: Link  $L_{BHall}$  fade NECD for year of 2002.

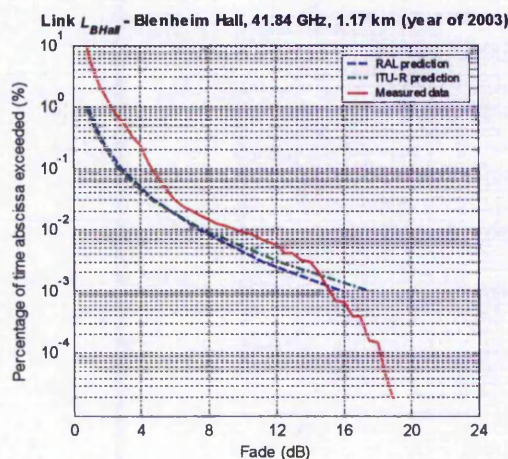


Figure 5-3: Link  $L_{BHall}$  fade NECD for year of 2003.

Comparison between both plots indicates that the overall fade experienced in year 2003 is slightly lower than the preceding year. This difference highlights the variability of the year to year statistic. If year 2003 is taken to be a typical year, then the previous year can be assumed to be a wetter year with more rainfall.

From Figure 5-3, an increase in fade margin of 5 dB from 4.5 dB is needed to decrease the system unavailability of  $10^{-1}$  % (525.6 minutes of an average year) to  $10^{-2}$  % (52.56 minutes of an average year). This equates to an improvement of the system availability at 99.9 % by an order of magnitude to 99.99 %. A similar improvement for year 2002 requires an additional 6 dB on top of the current 6 dB fade margin.

The ITU-R availability prediction model can be seen to underestimate the fade of link  $L_{HomeLOS}$  over the scaled time percentages of  $10^{-3}$  % to  $10^0$  %. However, extrapolation of the prediction model along the same curve for the smaller time percentages seems to indicate an overestimation of fade when compared to the actual measured value. This discrepancy is also evident in the plots of in Figure 5-4, which is the fade non-exceedance statistic for a shorter radio link path, using the long-term measured fade data of link  $L_{HomeLOS}$  of an average year. The extrapolation of the predicted curve is valid as the prediction model appears to be limited by the power law function [43] that is used to deduce the fade over the stated scaled time percentages.

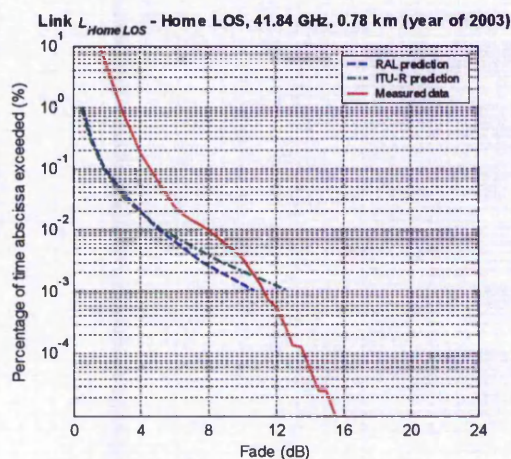


Figure 5-4: Link  $L_{Home\ LOS}$  fade NECD for year of 2003.

For the ITU-R prediction, the only meteorological input parameter used is the long-term statistic of point rainfall rate obtained from rain gauge measurement. Since only the precipitation attenuation component is considered in the prediction model, whilst the measured fade likely includes attenuation due to all hydrometeors such as hail, snow and fog, the fade statistic derived from the measured data is thus expected to be greater than the ITU-R prediction. Furthermore, the effect of wetting due to precipitation, and built up of frozen precipitation [28], on the antenna of the millimetre-wave radio could potentially account for a few dB additional attenuation. Between the two different ITU-R and RAL path reduction factor, the latter one seems to provide a better approximation to the measured fade of link  $L_{BHall}$ .

However, there does not appear to be an obvious reason as to the overestimation of fade given by the prediction model for the smaller time percentages (from 10<sup>-3</sup> % onwards), which is apparent in all the presented results. What it does suggest, is that, the ITU-R prediction model will need to be improved to reflect these under- and overestimation of the fade for the two time percentage range.

### 5.1.2 Fade Duration Statistic

Fade duration is defined as the period of time between two consecutive crossings of the received signal power on the same given fade threshold. In other words, the duration of a given fade event is the period between the time at which the received signal power crosses the said fade threshold with positive slope, to the time at which the received signal power level falls below the same fade threshold, with negative slope.

The fade duration statistic is an important parameter to be taken into account in MWS design and deployment, as it provides an insight into the statistical distribution of a fade event which may then be used to determine system unavailability, define compensation duration for fade mitigation techniques, and impact on the choice of improved coding schemes [109]. Results from fade duration analysis are generally presented as a statistic of the number of fade events above a given fade threshold (see Section 2.5.2)

A prediction model for fade duration due to precipitation events has been developed based on statistics of the duration of point rainfall rates and analysis of fade durations of a 38 GHz link over a 9 km path [73, 74]. This prediction model has only been tested on a 3.3 km, 39 GHz link, which seems, in general, to underestimate the number of events for any given duration.

In order to use the prediction model, the rainfall rate  $R_A$  (mm/h) which gives rise to a given fade depth,  $A$  (dB), is required along with the RAL path reduction factor. Deriving the latter requires the simultaneous solving of the expression for both the precipitation specific attenuation from Equation 2-10, and the RAL path reduction factor from Equation 2-13. For link  $L_{BH_{all}}$ , the derived rainfall rate for a required fade threshold of 2 to 20 dB in steps of 2 dB is as tabulated in Table 5-1.

<b>A (dB)</b>	2	4	6	8	10	12	14	16	18	20
<b><math>R_A</math> (mm/h)</b>	5.02	10.61	16.45	22.73	29.97	37.61	45.60	53.92	62.54	71.45

**Table 5-1: Tabulated  $R_A$  for link  $L_{BH_{all}}$ .**

Figure 5-5 gives the fade duration NECD curves for the dataset of measured fade from link  $L_{BHall}$  covering the year of 2003. Each distribution curve is a plot of the duration statistics as a function of fade threshold, in steps of 2 dB to 18 dB. The predicted statistic for each curve, obtained from the fade duration prediction model, is also included, and is represented by the corresponding smooth line plot.

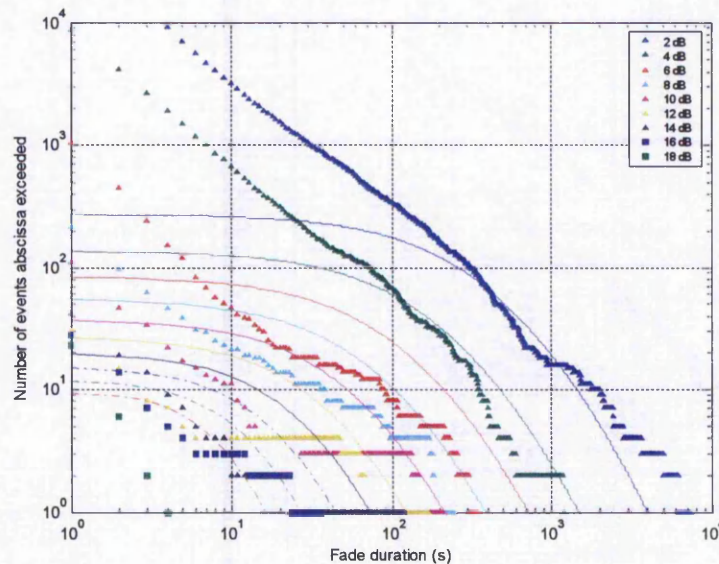


Figure 5-5: Link  $L_{BHall}$  fade duration NECD for year of 2003 (prediction given as smooth line plot).

The effect of increasing fade margin for a given MWS can be clearly seen from the fade duration distribution curves. For example, for a fade margin of 4 dB, there were 68 events where the received signal fade duration exceeded 100 s. If the fade margin is increased to 8 dB, the corresponding number of cases reduces significantly to 4 events.

Comparison of the measured and predicted fade duration statistic yields promising results. For the lower number of fade events from 100 and below, the prediction model gives increasingly good approximation as the fade threshold increases. As an example, at fade threshold of 2, 4, 6 and 8 dB, the difference in measured and predicted fade duration exceeded by 10 events is 317, 126, 121 and 66 s respectively.

Discrepancies in the predicted fade duration statistic are to be expected as the prediction model is derived from point rainfall rate. Previous studies have shown that actual rain events are spatially distributed and vary as the rain cell moves (see Section 2.5.4). Thus, a

rain cell that travels along a radio link in comparison to the same rain cell that passes transversely across same radio link, will give rise to durations of events with the same level of attenuation that are somewhat longer than in the transverse case, depending on the length of the link and the speed with which the rain cell travels.

From the level of 100 fade events and above, the measured fade duration statistic starts to deviate extensively from the predicted value. This increase in the number of events is characterised by events having increasingly smaller duration. Consequently, at least part of these events can be attributed to quantisation noise (arising from the signal measurement system) in the measured, received signal, which produces many fluctuating fade events with short duration.

There is no known published work comparing and verifying the fade duration prediction model to actual measured data, apart from the one undertaken during development of the prediction model. The results shown here confirm that the fade duration prediction model can reliably predict the said statistic for any similar 1.17 km long, 42 GHz wideband millimetre-wave radio link.

## 5.2 Dynamics of Foliage Blockage

Coverage measurement, highlighted in the literature review, indicates that blockage due to foliage in a typical MWS deployment can be as high as a quarter of the target service area (see Section 2.5.1). However, depending on the type and depth of foliage, and environmental conditions, a receiver site where foliage encroaches on the signal path may not suffer sufficient mean attenuation so as to take the received signal level below the system margin. In such instances, the provision of services is still, and has been shown to be possible [83]. This is especially true for receiver sites near the head-end base station where the system margin is greatest.

When considering the effects of foliage blockage, it is clear that the signal propagating environment will not remain static. While the foliage itself is undergoing change due to seasonal growth, its leaves and branches are subjected to movement disturbances due primarily to wind, and to a lesser extent rainfall. Coupled with the further effect of wetness as a result of precipitation, the foliage emerges as randomly distributed scatterers for the millimetre-wave signal. Apart from absorption loss due to moisture within the foliage, the millimetre-wave signal propagating through the foliage will also likely suffer multipath fading due to scattering, leading to rapid amplitude variations with deep nulls that can render the signal useless with conventional coding. Under such circumstances, even the best radio receiver position at point of installation may change over time.

In order to facilitate and enhance the provision of services for 42 GHz wideband signal propagating through foliage with sufficient system margin, the long-term performance and temporal statistic need to be understood. A measurement campaign covering a duration of 6 months has been undertaken to address the said statistic and lack of any published material on long-term measurement.

### 5.2.1 Measurement Set Up

Two (locally sited) millimetre-wave radio receivers and the associated signal measurement system were set up for the measurement campaign. The first of these radio receivers was placed behind a tree forming a through tree link,  $L_{Tree+path}$ , while the other forms a LOS link,  $L_{Home\ LOS}$ , running horizontally in parallel to the first. Figure 5-6 depicts the path layout of the two spatial diversity links.

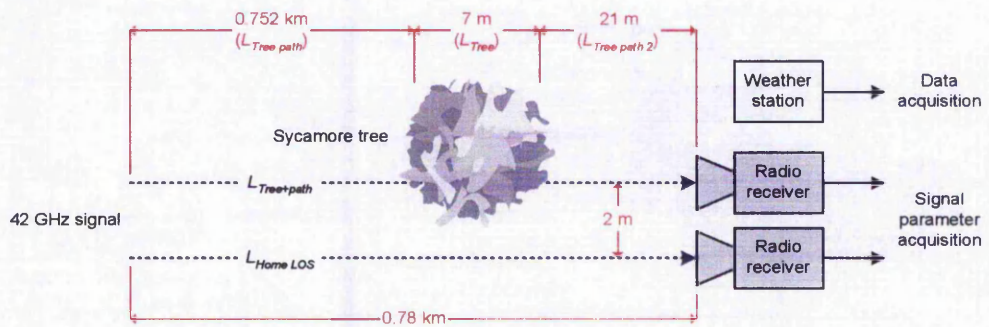


Figure 5-6: Aerial view of the spatial diversity links path profile.

Measurement of the 42 GHz wideband transmitted digital video signal is carried out at a time resolution of 1 s. A complete weather station measurement system is also installed to provide local, site-specific measurement of wind speed, rainfall rate and temperature for correlation with the logged signal parameters data.

The chosen tree type in the measurement path is a Sycamore tree (*Acer pseudoplatanus*), as shown in Figure 5-7 during the autumn season. This is a deciduous tree, approximately 10 m high with spreading branches and oval crown. The leaves of the Sycamore tree are typically around 7.5 cm wide with 5 lobes.

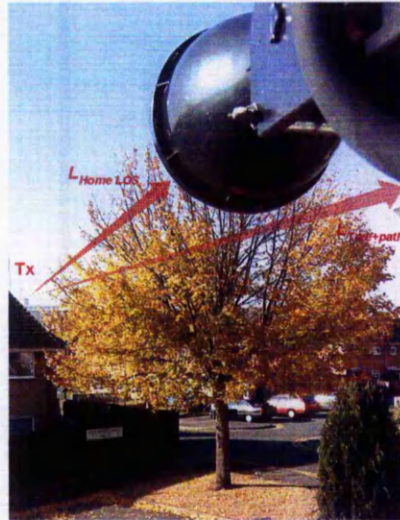


Figure 5-7: Photo of the spatial diversity link set up.

Several considerations prompt the installation of the second link,  $L_{Home\ LOS}$ . The radio subsystem gain of the millimetre-wave receiver is shown to vary with ambient temperature (and to a lesser degree, with aging) (see Section 4.1.1). The extent of variation is fairly significant when conducting long-term measurement as both diurnal and seasonal temperature changes alter the local mean baseline level from which the fade statistic is derived.

While the proposed iterative CUSUM analysis is a valid mitigation technique for a typical LOS link (see Section 4.3), its effectiveness in discerning changes in the local mean of a through tree link with an expected highly varying signal level is in doubt. Therefore, link  $L_{Home\ LOS}$  in conjunction with the iterative CUSUM analysis is used as the reference local mean level for the link  $L_{Tree+path}$ , as both radio receivers experience similar ambient temperature condition due to their close proximity.

Apart from that, link  $L_{Home\ LOS}$  is also required to isolate fade events caused by the through air link,  $L_{Tree\ path}$  and  $L_{Tree\ path\ 2}$ , from link  $L_{Tree+path}$ , leaving only fade events that are due solely to signal propagation through the tree. This through tree link is denoted as,  $L_{Tree}$ . If the fade,  $F$ , is given as a function of link type, the previously stated relationship can then be expressed as

$$F_{L_{Tree+path}} = F_{L_{Tree\ path}} + F_{L_{Tree}} + F_{L_{Tree\ path\ 2}} \quad (\text{dB}) \quad 5-1$$

where, due to the insignificant path length of link  $L_{Tree\ path\ 2}$  relative to link  $L_{Tree\ path}$ ,

$$F_{L_{Tree\ path\ 2}} \approx 0 \quad (\text{dB}) \quad 5-2$$

and, as a result of comparable path length and close proximity of link  $L_{Tree\ path}$  and  $L_{Home\ LOS}$ ,

$$F_{L_{Tree\ path}} \approx F_{L_{Home\ LOS}} \quad (\text{dB}) \quad 5-3$$

Hence, the fade that arises from just the actual through tree link  $L_{Tree}$  at sample time  $t$ , from the time series of measurements of the spatial diversity links is obtained by solving Equation 5-1, 5-2 and 5-3, yielding

$$F_{L_{Tree}}(t) = F_{L_{Tree+path}}(t) - F_{L_{Home\ LOS}}(t) \quad (\text{dB}) \quad 5-4$$

Any fade statistic of link  $L_{Tree}$  that is derived from Equation 5-4 will be independent of the effect of the preceding propagating path, which in turn enables a stand-alone through tree signal propagation model to be obtained. Such a model is highly relevant to the design and planning of MWS deployment. In view of this, most of the statistical analysis will be carried out on the actual through tree link  $L_{Tree}$ , based on the definition given in Equation 5-4.

### 5.2.2 Through Tree Signal Power Variation Characteristics

The temporal variation of the received signal propagating through the in-leaf tree of link  $L_{Tree+path}$ , is evident in the received signal power plot of the spatial diversity link in Figure 5-8.

Through tree signal power variation over the range of -42 to -22 dBm has been observed, as measured at the IF output of the millimetre-wave radio receiver. The latter range of -42 dBm also appears to be fairly constant, representing the received IF signal level following maximum attenuation by a Sycamore tree with a foliage depth of approximately 7 m.

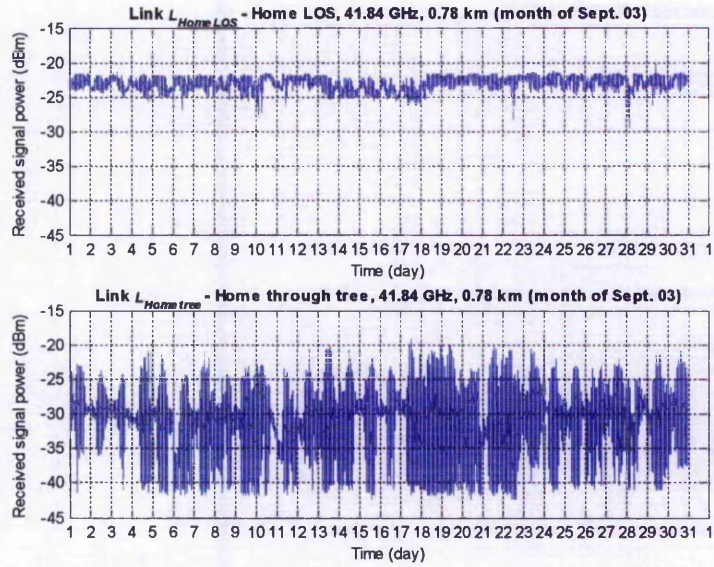
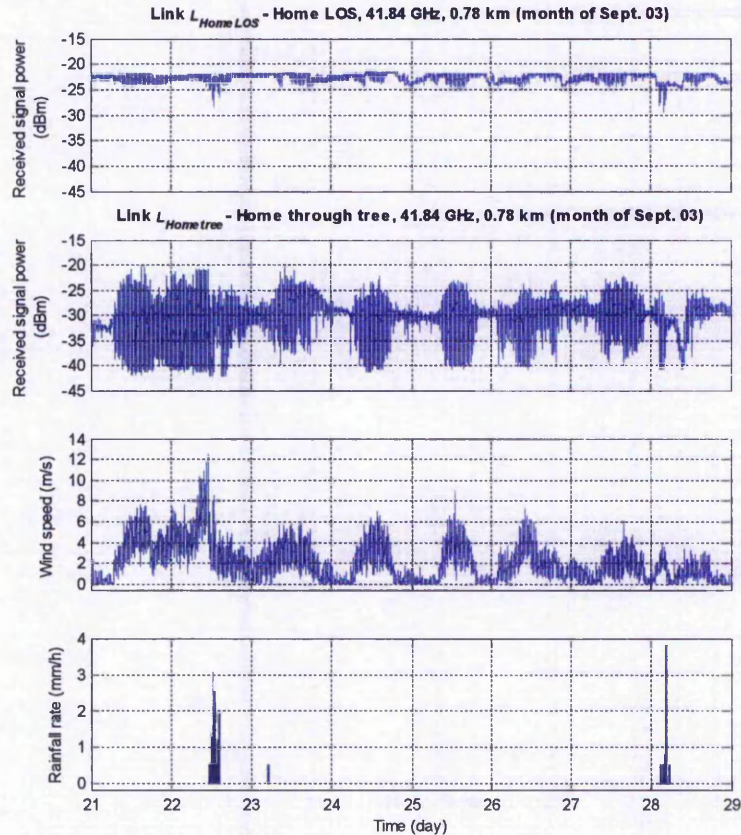


Figure 5-8: Measured received signal power from spatial diversity link.

In contrast, the received signal power variation of link  $L_{Home\ LOS}$  is very conservative, with variation typically from -25 to -23 dBm. Correlation of the received signal power to the measured temperature shows that the slow fluctuation in the local mean of the signal is due to diurnal temperature changes. Except for the identified rain event period on the 10<sup>th</sup>, 22<sup>nd</sup> and 28<sup>th</sup>, the excess signal variation in link  $L_{Tree+path}$  can be attributed to movement in the leaves and branches of the tree that is very likely caused by wind.

A time expanded view of Figure 5-8 encompassing the rain events on the 22<sup>nd</sup> and 28<sup>th</sup>, along with the measured wind speed and rainfall rate is presented in Figure 5-9. The influence of wind speed on the through tree signal variation is evident by observing the time period where the wind speed,  $w_s$ , is minimal ( $w_s < 2$  m/s), at the start of the day on the 24<sup>th</sup>, 25<sup>th</sup> and 26<sup>th</sup>, during which the through tree signal variation is also at its minimum. The corresponding received signal power level during these times provides a rough indication of the mean attenuation provided by the near static Sycamore tree. As the wind speed starts to increase and peak in the middle of each respective day, the through tree signal variation also significantly increases.

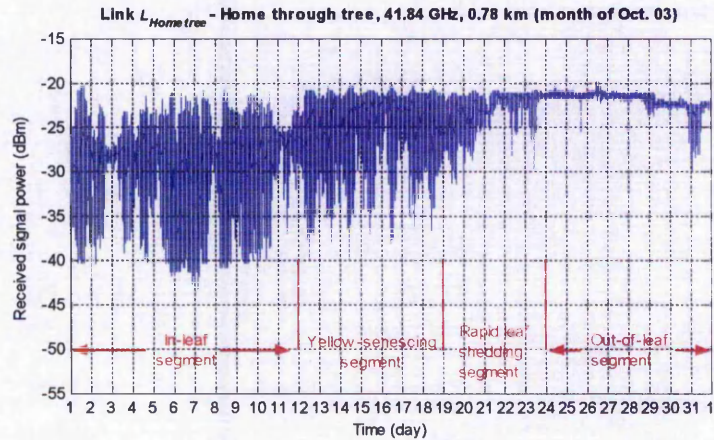


**Figure 5-9: Influence of wind speed and rain on signal variation.**

The effects of excess attenuation due rain events on the through tree signal variation, does not appear to be perceptible in this initial inspection of the chosen data set of Figure 5-9. A plausible explanation could lie in the fact that the influence of rain could have been masked by the influence of increase in wind speed during those periods.

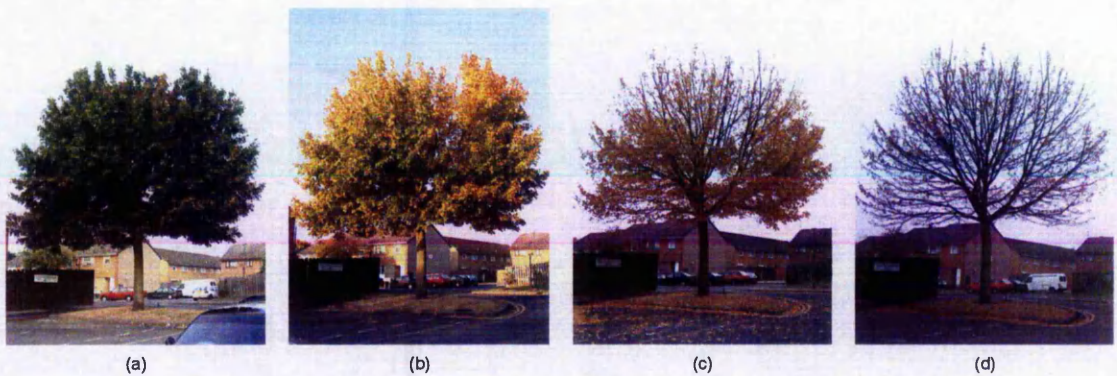
Apart from wind speed and rain condition, the seasonal growth and senescing state undergone by the Sycamore tree, in transiting from in-leaf to out-of-leaf and vice versa, also influences the through tree signal variation. The long-term measurement campaign has enabled the unique observation of the effect of this seasonal transition. Analysis of the measured signal parameters data has been carried out by first, splitting the data into different segments according to the senescing state of the tree, and analysing each independently.

Figure 5-10 depicts the through tree signal variation across several defined senescing states of the Sycamore tree, during the month of October, 2003. Both signal variation and maximum attenuation decreases in transiting from the in-leaf to out-of-leaf segment. The local mean of the received signal power can also be seen to increase from the initial approximate level of -28 dBm to -22 dBm. Based on these observations, segmentation of the measured signal parameter data is necessary, so as not to bias the statistical analysis.



**Figure 5-10: Influence of seasonal transition from in-leaf to out-of-leaf on through tree signal variation.**

The decision for the region to segment is subjectively chosen based on the combination of visual inspection and referencing the measured through tree signal power. Representative photos of the Sycamore tree taken approximately in the middle of each defined segment are shown in Figure 5-11.



**Figure 5-11: Photos of the sycamore tree covering the time period of (a) in-leaf-segment, (b) yellow-senescing, (c) rapid leaf shedding, and (d) out-of-leaf.**

The influences of both wind speed and rain on the through tree signal variation for the same month of October, 2003, is given in Figure 5-12. For the time period of the 1<sup>st</sup> to 23<sup>rd</sup>, which covers the in-leaf, yellow-senescing and rapid leaf shedding segment, variation in the through tree signal is shown to be strongly correlated to wind speed. The yellow-senescing segment continues to exhibit signal variation albeit to a lesser extent, both in dynamic range and frequency of occurrence as compared to the in-leaf segment. The corresponding photos from Figure 5-11 indicate that while the volume of leaves is still comparable to the in-leaf case, the lack of moisture in the yellow-senescing leaves is likely to contribute to the observed decrease in signal attenuation.

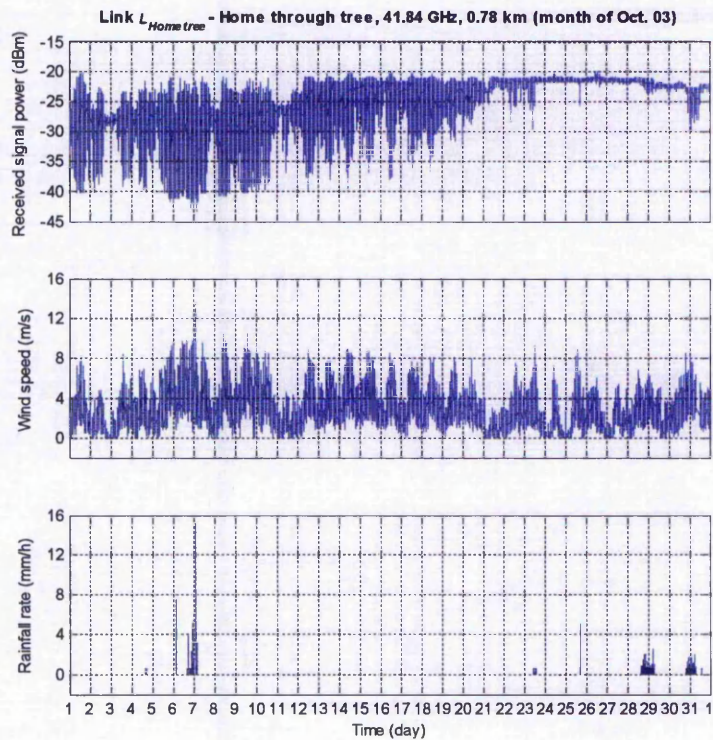


**Figure 5-12: Influence of wind speed and rain on the through tree signal variation.**

Figure 5-11 also shows that the decreases in signal variation towards the middle of the rapid leaf shedding segment may be attributed to the lost in leaf volume, (which previously serves as random scatterers to the propagating millimetre-wave signal). The influences of wind speed on the through tree signal variation during the out-of-leaf segment is not perceivable.

Aspects of end-user service quality, in the reception of the broadcasted digital TV on link  $L_{Home\ tree}$ , are indicated in Figure 5-13, via the plot of pre-Viterbi BER, and scatter plots of the number of RS packets corrected and lost. The quality of the through tree received broadcast service can be seen to deteriorate under the similar influences of the observed weather conditions, in particular during the period of in-leaf. A huge improvement to this broadcast service is observed when the tree eventually goes into the out-of-leaf state.

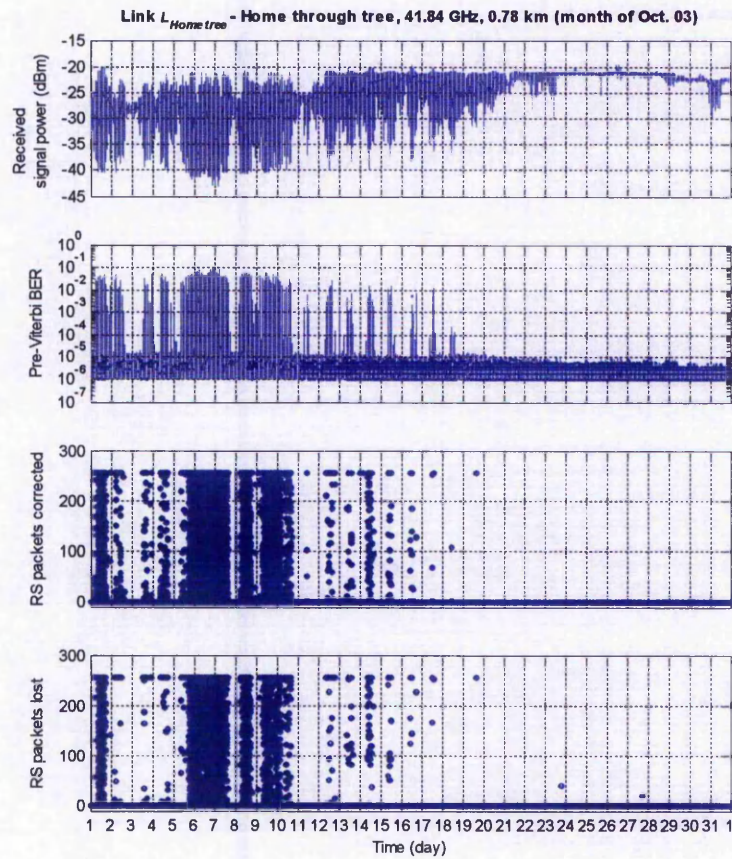


Figure 5-13: Service quality of the through tree broadcast signal.

Table 5-2 lists the time period over which the measurement campaign was conducted. The available measured signal parameter data for the in-leaf time segment encompasses over 100 days. Statistical analysis of the measured data will focus primary on these in-leaf data, under the influence of different wind speed threshold, with comparison made between arid and rain conditions.

Senescing state	Segment start time	Segment end time
In-leaf	01/07/03 00:00:00	11/10/03 23:59:59
Yellow-senescing	12/10/03 00:00:00	18/10/03 23:59:59
Rapid leaf shedding	19/10/03 00:00:00	23/10/03 23:59:59
Out-of-leaf	24/07/03 00:00:00	31/12/03 23:59:59

Table 5-2: Segmentation of the through tree signal variation measurement period.

### Fade Variation Statistic

The time series fade data for link  $L_{Tree}$ , is determined according to Equation 5-4. Having accounted for free space path loss and the issues of changes in the local mean baseline level, the derived through tree fade data is representative of the attenuation caused solely by the Sycamore tree, on the 42 GHz millimetre-wave wideband signal propagating through it.

Variation of the through tree fade on a daily basis for the first ten days of October, 2003, is depicted in Figure 5-14. With the exception of the 6<sup>th</sup> and 7<sup>th</sup> which experiences outbreak of rain, the higher occurrences of variation and magnitude in the through tree fade tend to be concentrated in the middle of the day.

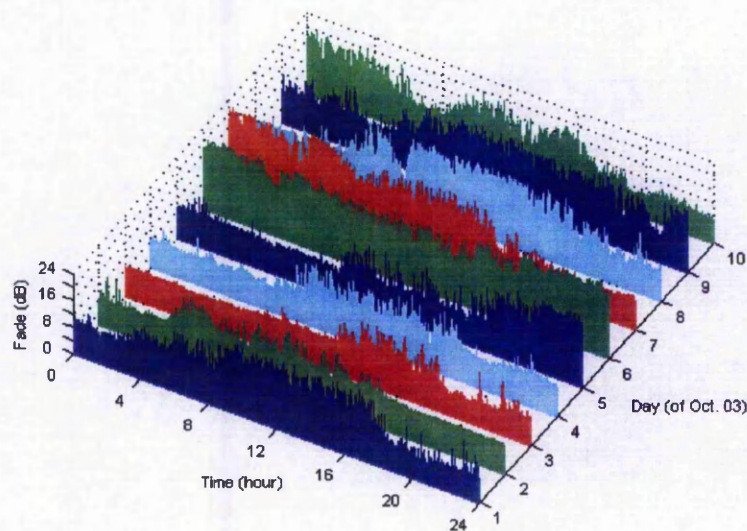
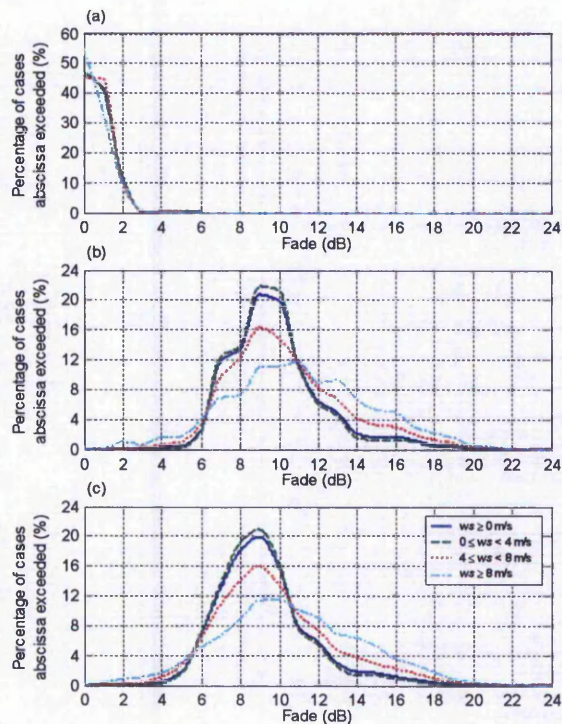


Figure 5-14: Fade diurnal variation.

To facilitate a better understanding of the fade variation statistic, a larger set of through tree fade data is examined. Using fade data from link  $L_{Home\ LOS}$ ,  $L_{Tree+path}$ , and  $L_{Tree}$ , an analysis of the fade variation non-exceedance distribution (NED) at various fade thresholds is carried out. For each link, the influence of wind speed is also accounted for. Figure 5-15 shows the resulting fade variation distribution curves for the in-leaf data segment, under arid conditions.



**Figure 5-15: Influence of wind speed on fade variation NED for in-leaf, arid condition, for (a) link  $L_{Home\ LOS}$ , (b) Link  $L_{Tree+path}$ , and (c) link  $L_{Tree}$**

Link  $L_{Home\ LOS}$  exhibits a distribution where the bulk of fade variations are concentrated in the region of 0 to 1 dB. In the derivation of link  $L_{Tree}$ , removing the effect of link  $L_{Home\ LOS}$  appears to produce a link  $L_{Tree}$ , that is a shift of the curve of link  $L_{Tree+path}$  by -1 dB. The derived link  $L_{Tree}$  is also shown to maintain a similar shaped fade variation curve as link  $L_{Tree+path}$ . Thus, it can be inferred that the effect of adding any path length to millimetre-wave signal propagating through tree generalises to shift in the through tree fade variation distribution by an equivalent of the predominant fade due to the path.

The majority of fade for link  $L_{Tree}$  can be seen to converge at the threshold of 9 dB, which is justified if this level is the mean attenuation for the through tree signal when it is static. In order to determine where the through tree mean attenuation lies, all the recorded cases of fade during period of no wind is averaged. The obtained fade will then be the best estimate of the required level, as the absence of wind during these times indicates that the attenuation suffered is a direct result of absorption and scattering by static leaves and branches of the tree.

This through tree mean attenuation level,  $F_{Tree, mean}$ , was eventually found to be

$$F_{Tree, mean} = 9.7 \text{ dB} \quad 5-5$$

Hence, the incidence of more fades near the threshold of 9 dB is to be expected as this is the level of which through tree fades will tend to rise from and fall to. The existence of fades above 9 dB indicates activities of enhancement in which random movement of the leaves and branches of the tree combine in such a way as to permit a less attenuating propagation path for the millimetre-wave signal.

Figure 5-15 (a) also indicates that wind has negligible influence on link  $L_{Home LOS}$ . In contrast, as wind speed increases, the through tree fade variation curve becomes flatter and wider. These changes in the curve indicate more variation in the fades, with increase in occurrence of higher magnitude fades.

The plots in Figure 5-16 shows the fade variation NED curves, covering fade data during rain instead of arid conditions. The derived link  $L_{Tree}$  is also shown to have a comparable shaped fade variation curve as link  $L_{Tree+path}$ , and is, in essence, a shifted version of link  $L_{Tree+path}$  curve. The magnitude of the shift is approximately by -2 dB, which matches the concentration of fades for link  $L_{Home LOS}$ .

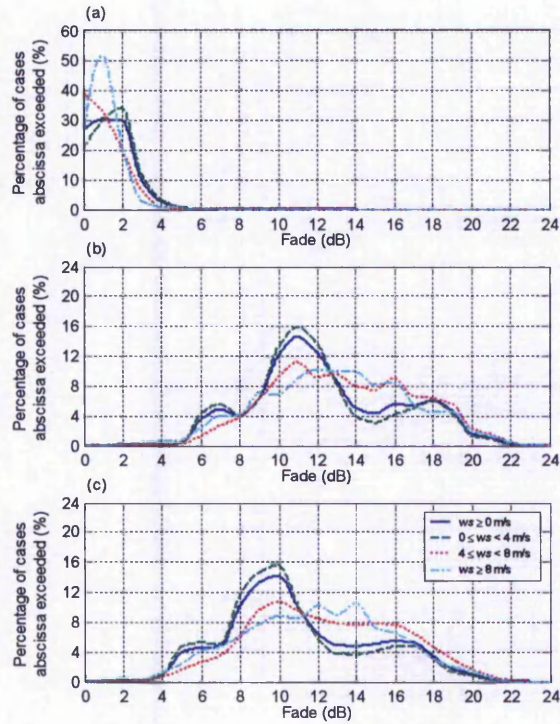


**Figure 5-16: Influence of wind speed on fade variation NED for in-leaf, rain condition, for (a) link  $L_{Home\ LOS}$ , (b) Link  $L_{Tree+path}$ , and (c) link  $L_{Tree}$**

In comparison to arid conditions, rain is shown to give rise to excess attenuation with a significant increase of fade in the region of 14 to 18 dB. Furthermore, the rain seems to cause the distribution to degenerate into a bimodal curve, with a possible second peak at a fade of 17 dB. The effect of increase in wind speed shows a similar increase in fade variation as in the case of arid conditions. However, the difference in influence of medium and high wind speed is negligible.

A set of fade variation NED curves for link  $L_{Tree}$ , obtained using the dataset from both yellow-senescing and rapid leaf shedding segment, under arid conditions, is given in Figure 5-17. The fade variation for the yellow-senescing segment is significantly reduced compared to the in-leaf segment from Figure 5-15 (c). This observation can be attributed to the lack of moisture in yellow-senescing leaves as highlighted in Section 5.2.2. Further reduction in fade variation is apparent for the rapid leaf shedding segment in Figure 5-17 (b), as it experiences significant loss in leaf volume.

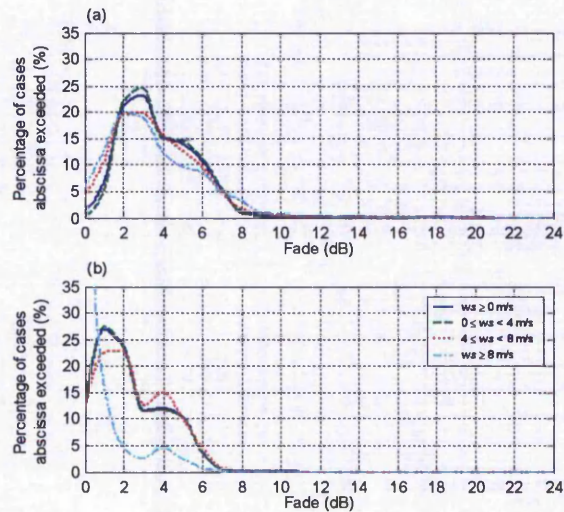


**Figure 5-17: Influence of wind speed on fade variation NED for arid condition and link  $L_{Trees}$  for (a) yellow-senescing, and (b) rapid leaf shedding.**

The fade variation NED curves for the in-leaf data segment, for the different wind speed range and arid condition, are fitted with the selected relevant Gamma and Lognormal distribution [110], and the Extreme Value distribution that was used in similar work [81]. Of these three distributions, the former two are common in the domain of RF propagation modelling, whereas the latter is typically used to describe extreme meteorological events such as the size of floods [81].

To test the goodness-of-fit (GOF) of a particular distribution to the studied fade data, the Kolmogorov-Smirnov (K-S) test and Anderson-Darling (A-D) test [111] is utilised, instead of the more conventional Chi-squared ( $\chi^2$ ) test. Omission of the  $\chi^2$  test is due to the fact that this test requires partition of the test data and as such introduces ambiguity as the interpretation is dependent on the selected partitioning [112].

The use of two GOF tests is motivated by the tendency of the GOF test to reject the chosen distribution fit, as a consequence of the large number of fade data that is to be tested [112]. The GOF test is thus taken as a guide, in which a smaller test static value indicates a better fit.

Figure 5-18 illustrates the distribution fitting analysis undertaken, with the best fit distribution overlaid onto the fade variation NED curves. The result of the K-S and A-D GOF test for all the different wind speed range is summarised in Table 5-3. It is observed that curves of the fade variation NED for the in-leaf data segment under arid condition, can be appropriately represented by the Extreme Value distribution for all wind speed condition, with the exception of the high wind speed range, which is better fit by the Gamma distribution. The suitability of the Extreme Value distribution is in agreement with other work [81].

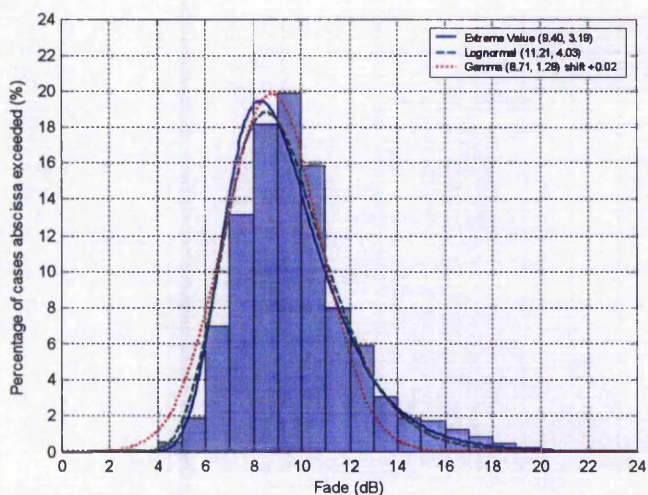


Figure 5-18: Distribution fitting of link  $L_{Tree}$  fade variation NED for  $w_s \geq 0$  m/s, arid condition.

Wind Speed, $s$ (m/s)	Fitted distribution	K-S test	A-D test
$s \geq 0$	Extreme Value	<b>0.0472</b>	7.4272e3
	Lognormal	0.0500	<b>6.6454e3</b>
	Gamma	0.0633	1.1793e4
$0 \leq s < 4$	Extreme Value	<b>0.0444</b>	4.8398e3
	Lognormal	0.0482	<b>4.1917e3</b>
	Gamma	0.0601	8.0030e3
$4 \leq s < 8$	Extreme Value	<b>0.0399</b>	<b>1.0447e3</b>
	Lognormal	0.0438	1.0987e3
	Gamma	0.0452	1.2658e3
$s \geq 8$	Extreme Value	0.0703	1.3596e2
	Lognormal	0.1007	2.8967e2
	Gamma	<b>0.0233</b>	<b>7.4532e0</b>

Table 5-3: GOF test for distribution fitting of link  $L_{Tree}$  fade variation NED for different wind speed range, under arid condition.

Similar distribution fitting analysis is carried out for the through tree fade variation NED for in-leaf data segment under rain condition. Example of the fitted distribution is shown in Figure 5-19. The result of the analysis for all the different wind speed range is summarised in Table 5-4. The Extreme Value distribution is again found to best represent the fade variation curves for the low wind speed range, while the medium and high wind speed range is better represented by the Gamma distribution.

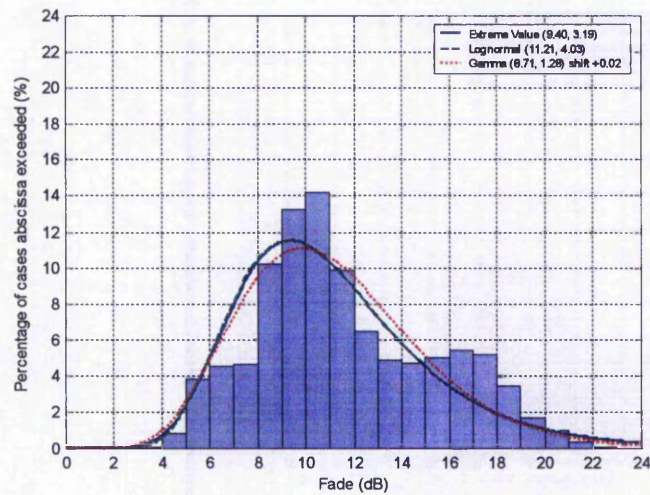


Figure 5-19: Distribution fitting of link  $L_{Tree}$  fade variation NED for  $w_s \geq 0$  m/s, rain condition.

Wind Speed, $s$ (m/s)	Fitted distribution	K-S GOF test	A-D GOF test
$s \geq 0$	Extreme Value	<b>0.0443</b>	<b>3.5710e2</b>
	Lognormal	0.0467	3.8452e2
	Gamma	0.0503	4.0424e2
$0 \leq s < 4$	Extreme Value	<b>0.0536</b>	<b>3.1107e2</b>
	Lognormal	0.0550	3.2803e2
	Gamma	0.0602	3.7410e2
$4 \leq s < 8$	Extreme Value	0.0546	1.4164e2
	Lognormal	0.0605	1.4668e2
	Gamma	<b>0.0466</b>	<b>7.5765e1</b>
$s \geq 8$	Extreme Value	0.0544	1.5452e1
	Lognormal	0.0893	3.3949e1
	Gamma	<b>0.0509</b>	<b>4.6951e0</b>

Table 5-4: GOF test for distribution fitting of link  $L_{Tree}$  fade variation NED for different wind speed range, under rain condition.

The Extreme Value distribution is defined by two parameters, denoted as *mode*,  $m$ , and *scale*,  $s$ . Its probability distribution function (PDF) is given as [113]

$$f(x) = \frac{1}{s} \cdot z \cdot e^{-z} \quad \text{for} \quad -\infty < x < \infty, \quad -\infty < m < \infty, \quad s > 0 \quad 5-6$$

where  $z = e^{\left(\frac{x-m}{s}\right)}$ .

For the case of the Gamma distribution, it is defined by three parameters, namely, *location*,  $L$ , *scale*,  $s$ , and *shape*,  $\beta$ . The PDF for the gamma distribution is given as [113]

$$f(x) = \frac{s}{\Gamma(\beta)s} \cdot (x-L)^{\beta-1} \cdot e^{-\left(\frac{x-L}{s}\right)} \quad \text{if} \quad x > L, \quad -\infty < \beta < \infty, \quad -\infty < s < \infty, \quad 5-7$$

$$f(x) = 0 \quad \text{if} \quad x \leq L$$

where  $\Gamma$  is the Gamma function.

From Equation 5-6 and 5-7, the relevant parameters for the best empirical fitted distribution from Table 5-3 and Table 5-4, is detailed in the following Table 5-5 and Table 5-6 respectively.

Wind Speed, $s$ (m/s)	Fitted distribution	$m$	$s$	$L$	$\beta$
$s \geq 0$	Extreme Value	8.16	2.07		
$0 \leq s < 4$	Extreme Value	8.10	1.86		
$4 \leq s < 8$	Extreme Value	8.41	2.66		
$s \geq 8$	Gamma		0.42	-22.06	77.64

**Table 5-5: Parameters for best empirical fitted distribution of link  $L_{Tree}$  fade variation NED for different wind speed range, under arid condition.**

Wind Speed, $s$ (m/s)	Fitted distribution	$m$	$s$	$L$	$\beta$
$s \geq 0$	Extreme Value	9.40	3.19		
$0 \leq s < 4$	Extreme Value	9.03	3.01		
$4 \leq s < 8$	Gamma		0.42	-21.53	81.79
$s \geq 8$	Gamma		0.46	-20.31	70.30

**Table 5-6: Parameters for best empirical fitted distribution of link  $L_{Tree}$  fade variation NED for different wind speed range, under rain condition.**

The tabulated values in Table 5-5 and Table 5-6 enable a stand-alone, through tree signal propagating model for 42 GHz millimetre-wave radio link that accounts for different weather conditions, to be obtained. Such a model is highly relevant towards the deployment of MWS, as it serves as an important input parameter for MWS planning and simulation tools such as ray-tracing software, or as model for testing through tree fade mitigation algorithm.

### 5.2.3 Fade Non-Exceedance Statistic

Figure 5-20 presents the through tree fade NECD as a function of the chosen wind speed range. The period covered is the in-leaf data segment. For a given percentage of time, the fade exceeded is shown to increase with rise in wind speed. In the case of the arid conditions, the fade for the three different wind speed range at 1% of time is 16.5, 18.5 and 19 dB respectively. If this latter fade of 19 dB is adopted as the fade margin for service provision in a MWS network, the service time unavailability will not exceed 1% (or approximately 7 hours for a typical month of 30 days) regardless of wind speed.

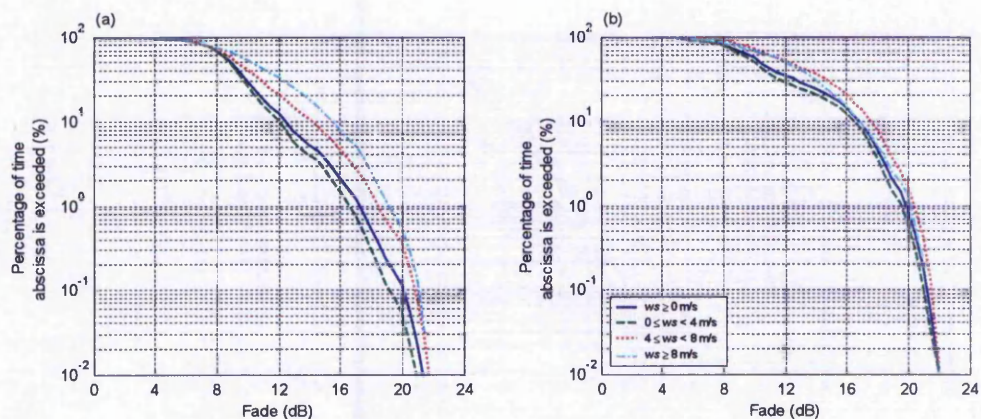


**Figure 5-20: Influence of wind speed on fade NECD for in-leaf, (a) arid, and (b) rain condition.**

However, this dependence on wind speed is not significant for rain condition. At the same time percentage, the difference in fade is within 1 dB. Excess attenuation caused by the rainfall itself could likely mask the effect of wind, which in turn manifest into the obtained result.

The slope of the distribution curve can be seen to fall rapidly for the smaller time percentage. In terms of providing services this outcome is beneficial as the increase in fade margin is heavily offset by the gain in service time availability. As an example, in the distribution curve of all wind speed range of Figure 5-20 (a), an increase of 3 dB in fade margin improves the service time availability from 99 % to 99.9 %. From that point onwards, only a maximum increase of 1 dB or less is required for an additional magnitude improvement in service time availability.

### 5.3 Route Diversity Improvement

Precipitation varies considerably in space and time. The spatial distribution of rain depends on the type of cell; convective events are typically localised whereas stratiform events tend to be widespread [28]. During periods of intense rain, severe precipitation attenuation will be experienced. In order to provide and maintain high system availability, some form of fade mitigation techniques will be necessary.

Studies on rain field databases have demonstrated that angular and route diversity (see Section 2.5.4) may be used as a way of exploiting the non-uniform spatial and temporal distribution of rain in improving system availability. There has been much research carried out into earth-space site diversity, with recent work starting to focus on the application of diversity for millimetre-wave terrestrial LOS site systems [77, 79]. However, most of these studies are based on widespread rainfall rate measurement, and not on the actual long-term measured millimetre-wave signal itself.

To address this, the available measurement data of link  $L_{Home\ LOS}$  and  $L_{BHall}$  for the year of 2003 is used to study the long-term effect of route diversity improvement. Due to the inhomogeneous nature of the precipitation event, the horizontal structure may well be such that, if a receiver site can be served by more than one transmitter, it is likely that connecting to the transmitter with the strongest signal at any instant can offer considerable improvement in availability.

Figure 5-21 illustrates the details of the path used in the route diversity study, in which the actual role of link  $L_{Home\ LOS}$  and  $L_{BHall}$  is reversed to simulate two base stations, denoted as  $Tx_1$  and  $Tx_2$ , servicing the user end,  $Rx_1$ . No attempt is made to normalise the fade statistic in terms of path length. Instead, it is assumed that the present configuration is a reasonable representation of a realistic MWS deployment scenario.

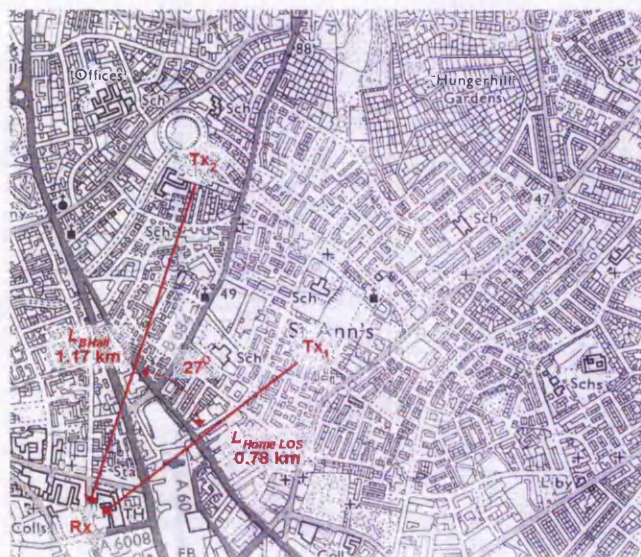


Figure 5-21: Path details for route diversity analysis using link  $L_{Home\ LOS}$  and  $L_{BHall}$ .

#### 5.4 Inhomogeneity of Precipitation Event

For a simple diversity scheme, such as switching between two base stations in order to receive the signal which suffers less fade, to function, variation in the rain cell, and hence fade experienced between the two links must be present. In order to demonstrate the occurrence of such a scenario, an excerpt, as shown in Figure 5-22, from the time series of measured signal parameter data for link  $L_{Home\ LOS}$  and  $L_{BHall}$  during the month of June, 2003, is examined.

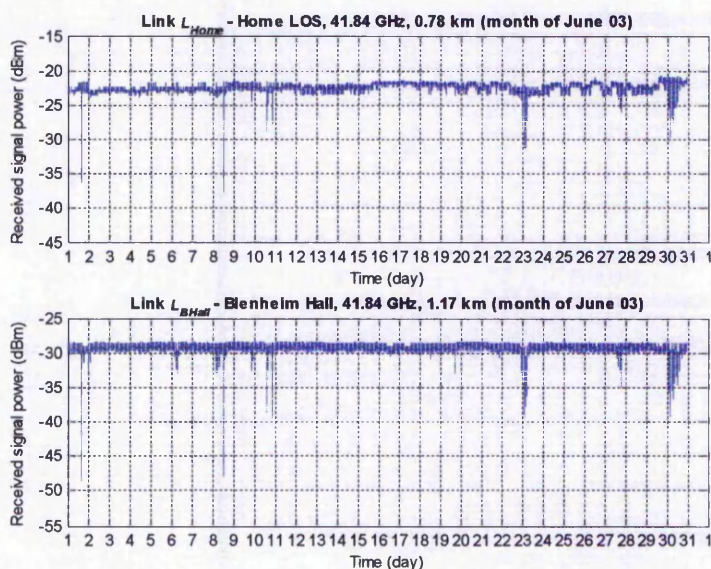


Figure 5-22: Received signal power of link  $L_{Home\ LOS}$  and  $L_{BHall}$  for the month of June.

During this particular summer month, both links experience numerous fade events which vary in intensity and duration, and have been identified as caused by precipitation. Of interest are the two deep precipitation fade events, on the 1<sup>st</sup> and 8<sup>th</sup> of the month. Figure 5-23 and Figure 5-24 provide an enlarged time scale view of these two events.

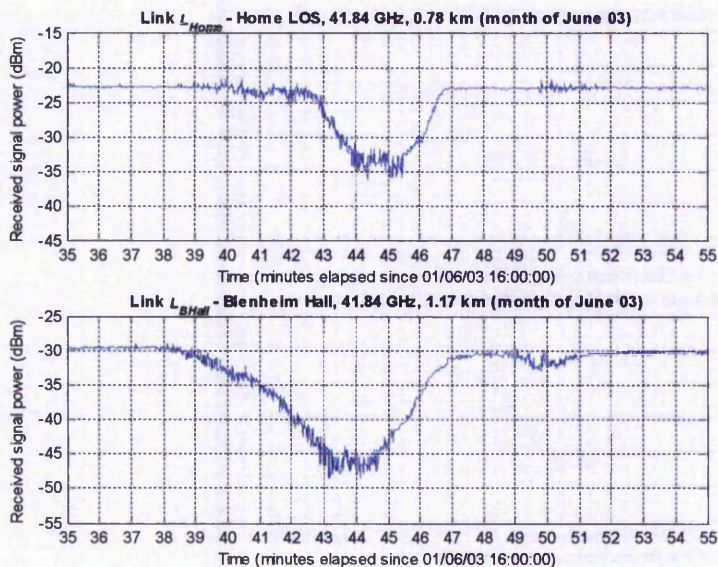


Figure 5-23: Received signal power of link  $L_{Home\ LOS}$  and  $L_{BHall}$  during rain event on 01/06/03.

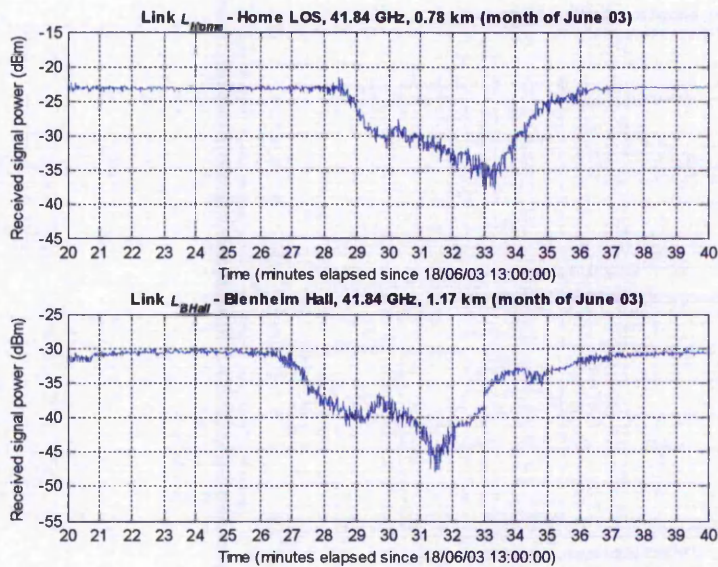


Figure 5-24: Received signal power of link  $L_{Home\ LOS}$  and  $L_{BHall}$  during rain event on 18/06/03.

In the first instance, the shorter link,  $L_{Home\ LOS}$ , experiences a smaller and shorter duration fade event, lasting only half as long as link  $L_{BHall}$ . As the fade event for link  $L_{BHall}$  completely envelopes link  $L_{Home\ LOS}$ , the receiver site will thus benefit from maximum system availability by receiving from the latter link.

In Figure 5-24, the fade suffered by both links, appears to traverse; starting from link  $L_{BHall}$ , and moving over to link  $L_{Home\ LOS}$ . Thus, in order to maintain maximum system availability, the receiver site  $Rx_1$  which started receiving from base station  $Tx_1$  should switch over to  $Tx_2$  from the reference time of 32 minutes.

#### 5.4.1 Diversity Statistic

The fade NECD for both link  $L_{BHall}$  and  $L_{Home\ LOS}$  is obtained, along with that of the maximum signal time series data as obtained from the two route diversity links. These results are then plotted out, as shown in Figure 5-25. The combined route diversity distribution curve indicates an overall improvement in time availability and increase in gain.

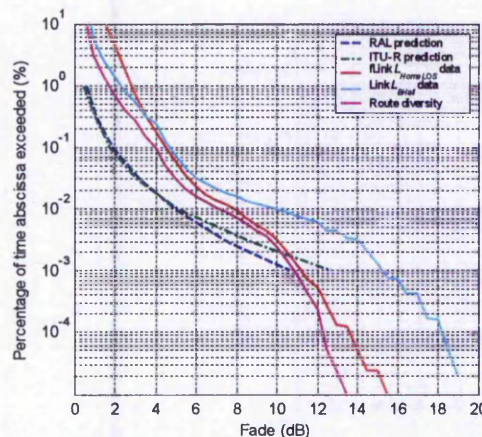


Figure 5-25: Route diversity improvement to fade NECD for year of 2003.

In order to quantify the effect of diversity, two forms of measures can be used [76]. First of this is the diversity gain,  $G(A)$ , which gives a measure of the reduction in the fade margin or an increase in the average signal value. It is defined as the difference, between the attenuation exceeded at a certain percentage of time for a single link and the attenuation exceeded at a certain percentage of time for a joint link, given as

$$G(A) = A(t) - A_d(t) \quad (\text{dB}) \quad 5-8$$

where,  $A_d(t)$  is the fade depth in the combined diversity path, occurring in time percentage  $t$ , and  $A(t)$  is the fade depth for the unprotected path. The other is diversity improvement,  $I(A)$ , which gives a measure of the increase in system availability. It is defined as the ratio of the single link to the joint link probabilities for a given fade depth, and can be expressed as

$$I(A) = \frac{P(A)}{P_d(A)} \quad 5-9$$

Similar to diversity gain,  $P_d(A)$  is the percentage of time in the combined diversity path with a fade depth larger than  $A$  dB while  $P(A)$  is the time percentage for the unprotected path. The diversity improvement, using the shorter link  $L_{Home\ LOS}$  as the unprotected link, is derived and presented in Figure 5-26.

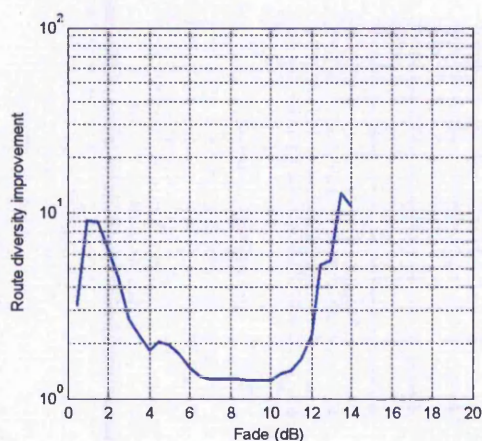


**Figure 5-26: Route diversity improvement factor for year of 2003.**

Diversity improvement from 2 to over 6 times is observed during the low time availability period of high fade of 12 and 13 dB respectively. Even for a moderate spatially distributed links used in this analysis, the long-term measured data still indicates that diversity improvement is achievable.

## 5.5 Summary

Statistics on the performance of a realistic 42 GHz MWS have been obtained from analysis of the results, obtained during the long-term field measurement campaign. The analyses encompass the three different areas of long-term precipitation fade, propagation through foliage, and spatial correlation in the distribution of precipitation fade.

The ITU-R availability prediction model is found to overestimate the fade for the smaller time percentages in the region of up to  $10^{-3}$  %, but underestimate for all ensuing larger time percentages. In the case of the fade duration prediction model, it gives a reliable estimate. The former includes the first ever verification using measured data from consecutive years, while the latter is the only confirmation of the model independent of the originating published work.

Analysis of the effects of weather and seasonal variation on the through foliage signal, measured over a 6-month period, has for the first time shown the contributing influence of seasonal change and weather conditions, and has also permitted isolation of the effect of path loss due to precipitation.

The availability of a two-year long monitored radio links was also found to be effected by the spatial distribution of precipitation event. Improvement to this availability is shown to be possible through the use of route diversity.

## **Chapter 6**

# **Conclusions**

This research concludes with summary of the work done. Further issues deserving more study and work are indicated.

## 6.1 Summary and Conclusion from Work Done

The research detailed within this thesis focuses on the investigation and development of the relevant infrastructure and hardware necessary to establish a long-term, widespread, field measurement campaign on a live 42 GHz MWS, and analysis of the collected field trial data.

A review of broadband access trends shows the adoption and advantages of millimetre-wave BFWA technology such as 42 GHz MWS, in providing high capacity broadcast, data and telecommunication services from the service provider to the end user. However, various signal propagation impairments, and MWS implementation and deployment issues still need to be resolved. The 42 GHz MWS campus network trial was undertaken to demonstrate the viability of the access technology and facilitate such investigation.

Investigation into relevant equipment integration issues and calibration tasks has resulted in a hybrid radio network employing technologies from diverse media. Provision of reliable digital video source was found using low cost DVB-T front-end modules, costing £300 each, in place of (an order of magnitude more expensive) professional terrestrial IRD. For interactive service, a DVB-RC cable network system was adapted for use with the radio network. The resulting 42 GHz MWS demonstrates interoperability with DVB terrestrial, satellite and cable services, being able to deliver digital TV and high-speed IP based data into the local trial area. Through the investigation conducted, the limitation of the radio system in terms of stability and saturation, which could effect signal measurement, was also made known. With the integrated equipment and radio in place, appropriate spatially diverse, remote sites, encompassing both LOS and through foliage links representing different types of propagation measurement scenario were deployed.

In order to determine the type of channel measurement that needed to be addressed, a thorough literature review on the background and progress of research work on BFWA, with attention specifically to millimetre-wave propagation and MWS was carried out. It was found that available results lack measurement of; (i) the actual 42 GHz signal, (ii) a wideband signal, and (iii) long-term time period. Measurements of specific interest that are

seen to be important include long-term precipitation fade, propagation through foliage and spatial distribution of precipitation fade.

A cost-effective signal measurement system utilising off-the-shelf satellite STB and custom built DAM, was developed to monitor and acquire various signal parameters of the millimetre-wave radio link from the ODU. Signal measurements via the satellite STB have been shown to be reliable, following a thorough exploration of the satellite STB architecture and conducted calibration work. The fabricated DAM integrates a reliable acquisition, logging and retrieval mechanism that works transparently to the normal operation of the satellite STB. This feature facilitated measurements in a live broadcast system. The combined cost for the satellite STB and DAM is low and does not exceed £130 for each measurement site. This work has thus proven the concept for a very low cost signal measurement system, and has facilitated the deployment of numerous measurement sites within the long-term field trial measurement campaign, with further potential to scale up without significant cost constraint.

Supporting meteorological data, sourced from a sub-£150 developed meteorological measurement system, consisting of the pairing of a low-cost weather station with automated data logging using a modified version of the developed DAM, has been used to correlate with the measured signal parameters. In addition, the development of a hardware fade simulation system has enabled reliable automated calibration of the signal measurement system, and also simulation of any fade profile for other hardware and algorithm tests.

Mitigation of the variation in the long-term local mean level of the monitored received signal power, which is primarily due to temperature loading on the millimetre-wave radio ODU, is realised through the novel implementation of an iterative CUSUM analysis with associated randomisation test. The proposed algorithm identifies significant local mean levels that can be used for a more accurate derivation of fade values, in place of the conventional use of a single baseline level. Implementation of the algorithm has been tested on data sets from both a hardware-based simulated fade, and from actual field measurement. Results indicate that the fundamental changes in local mean from which the fade value is derived, can be detected, and statistical analysis using the latter data set shows a more accurate unbiased derived fade statistic. The adopted randomisation test is

highly computer-intensive, which suggests a more pragmatic approach of applying the iterative CUSUM analysis to data segments that are difficult to interpret manually, instead of analysing the entire (or a long) sequence.

Different subsets of data of relevant length, extracted from the long-term field measurement campaign that span over 3 years, have been analysed using appropriate statistical approaches. The ITU-R availability prediction model is found to overestimate fade for the smaller time percentages of up to  $10^{-3}$  %, but underestimate for all following larger time percentages, when compared to actual measured fade of LOS links covering consecutive years and also from different sites. Evaluation of the measured fade data against the fade duration prediction model, which has never been tested with other measured data, appears to indicate that the model is reliable for 42 GHz radio link. Measured data of the signal propagating through foliage is also analysed to show the influence of different foliage senescing states and meteorological condition on the derived statistics. The results and empirical modelling presented are new, as there is no known published work covering the continuous measurement period of 6 months, and is statistically reliable due to the long-term measurement involved. Other analysis includes study of spatial correlation in the distribution of precipitation fade, using the year long measured data from two different radio links. Outcome of the analysis corroborates the use of different radio paths for diversity improvement. These results combine to provide accurate statistics and insight on the performance of a realistic 42 GHz MWS that corroborate or supplement prevailing published work.

## 6.2 Further Research Work

The framework presented in this research will serve, hopefully, for further rigorous research work. Three such areas are suggested.

An increase in the sampling resolution of the signal measurement system could be beneficial in terms of monitoring rapid fade events. Likely application includes measurement of through foliage signal. The present data acquisition module hardware caps the fastest possible logging to above 50 ms due to the time required in the SmartMedia bad block management routine. Possible solution could be the use of other much faster storage media.

The occurrence of diversity improvement even from moderately separated links indicates significant variation of fade within a cell. In order to determine the extent of this variation, a wider distribution of remote sites will be necessary, in order to facilitate a more elaborate collection of field measurement data of sites with varying spatial and range distribution. Increasing the number of sites within the service area will allow a more complete representation of events occurring within the entire cell. The measurement systems developed in this research could facilitate such work.

Actual practical implementation of route diversity to mitigate precipitation fade is non-trivial. Even simple diversity scheme that involves switching between two base stations in order to receive the least attenuated signal will require the proper combination of robust fade detection, control algorithm to handle the initiation and handover of data traffic to the secondary link, and efficient communication protocol to minimise capacity overhead. All these issues will need to be addressed by testing any proposed implementation with actual measured fade data.

Accuracy of the ITU-R availability prediction model can be further investigated by conducting, in parallel to a signal measurement, a precipitation measurement campaign using several rain gauges along the propagation path to collect path averaged rainfall rates. This precipitation data can then be analysed together the measured signal fade and prediction model.

**LIST OF PUBLICATIONS**

W. Y. Mun, E. B. Lam, R. Germon, "Multimedia wireless system for broadband access", Science, Engineering and Technology for Britain (SET for Britain), London, U.K., 2003.

R. Germon, E. B. Lam, "42 GHz MWS campus network trial", European Microwave Week 2001, Broadband Wireless Workshop, London, U.K., Sept. 2001.

E. B. Lam, R. Germon, "Deployment of a 42 GHz broadband fixed wireless access campus network trial," 3rd. Conf. on Postgraduate Research in Electronics, Photonics, Communications and Software (PREP2001), University of Keele, U.K., Apr. 2001.

R. Germon, D. Downes, E. B. Lam, C. Oswald, K. Williams, "42 GHz multimedia wireless system campus trial," IEE Seminar New Access Network Technologies, London, U.K., 2000, pp. 6/1-5.

## REFERENCES

- [1] A. Nordbotten, "LMDS systems and their application", *IEEE Comms. Magazine*, Jun. 2000.
- [2] C. Smith, "LMDS", McGraw-Hill Professional Telecom Publication, Aug. 2000.
- [3] European Radiocommunications Committee, "ERC Decision of 1 June 1999 on the designation of the harmonised frequency band 40.5 to 43.5 GHz for the introduction of Multimedia Wireless Systems (MWS), including Multipoint Video Distribution Systems (MVDS)", Jun. 1999.
- [4] ARC Group, "Broadband access 2002", Feb. 2002, at <http://www.arcgroup.com>.
- [5] W. Honchanrenko, J. PP. Kruys, D. V. Lee, N. J. Shah, "Broadband wireless access", *IEEE Comms. Magazine*, Jan. 1997, pp. 20-26.
- [6] ETSI ETS 300 802, "Digital Video Broadcasting (DVB): Network-independent protocols for DVB interactive services", Nov. 1997.
- [7] H. Loktu, (Ed.) ACTS Project 215, deliverable report D2P1B, "Specification of next-generation of LMDS architecture", Feb. 1999, pp. 1-2.
- [8] O. Grondalen, (Ed) ACTS Project 215, deliverable report D4P4, "Interactive broadband technology trials", Jan. 1999.
- [9] H. R. Anderson, "Simulations of channel capacity and frequency reuse in multipoint LMDS systems", 1999 IEEE Radio and Wireless Conf. (RAWCON 99), Aug. 1999, pp. 9-12.
- [10] V. I. Roman, "Frequency reuse and system deployment in local multipoint distribution service", *IEEE Personal Comms.*, Dec. 1999, vol. 6, no. 6, pp. 20-27.

- [11] C. A. Balanis, "Antenna theory: Analysis and design", 2nd. ed., Wiley, New York, 1997.
- [12] D. M. Pozar, "Microwave and RF design of Wireless Systems", Wiley, New York, 2001, pp. 19, 87, 114.
- [13] International Engineering Consortium, "Local multipoint distribution system (LMDS) tutorial", at <http://www.iec.org/online/tutorials/lmds/>.
- [14] R. Germon, D. Downes, E. B. Lam, C. Oswald, K. Williams, "42 GHz multimedia wireless system campus trial", IEE Seminar New Access Network Techs., IEE, 2000, pp. 6/1-5.
- [15] E. B. Lam, R. Germon, "Deployment of a 42 GHz broadband fixed wireless access campus network trial", 3rd. Conf. on Postgrad. Research in Electronics, Photonics, Comms. and Software (PREP2001), University of Keele, U.K., Apr. 2001.
- [16] R. Germon, E. B. Lam, "42 GHz MWS campus network trial", European Microwave Week 2001, Broadband Wireless Workshop, London, U.K., Sept. 2001.
- [17] ETSI EN 300 421 v010102p, "Digital Video Broadcasting (DVB): Framing structure, channel coding and modulation for 11/12 GHz satellite services", Oct. 1997.
- [18] Philips Semiconductors data sheet, "TDA8044AH satellite demodulator and decoder", Feb. 2000, at [www.semiconductors.philips.com/pip/TDA8044H.html](http://www.semiconductors.philips.com/pip/TDA8044H.html).
- [19] SES ASTRA "ASTRA free available TV channels", at [http://www.ses-astra.com/tv-radio/guide/lineup/markets/UK\\_digitalfree.htm](http://www.ses-astra.com/tv-radio/guide/lineup/markets/UK_digitalfree.htm).
- [20] The Digital TV Group "DTT Channel Allocation – The Midlands", at [http://www.dtg.org.uk/retailer/tx\\_details/tx\\_midlands.htm](http://www.dtg.org.uk/retailer/tx_details/tx_midlands.htm).

- [21] International Organisation for Standardization, "Generic Coding of Moving Picture and Associated Audio Information: Systems", ISO/IEC DIS 13818-1, International Organisation for Standardization, Geneva, Jun. 1994.
- [22] G. D. Plumb, I. R. Pullen, B. Tait, "UK DVB-T network planning and coverage verifications", Int. Broadcasting Conv. (IBC 99), Amsterdam, Netherlands, Sept. 1999.
- [23] ETSI ETS 300 800, "Digital Video Broadcasting (DVB): Interaction channel for Cable TV distribution systems (CATV)", Jul. 1998.
- [24] COCOM A/S, "INA HFC headend CC1014 - Operator and service manual", 1999.
- [25] C. M. Buch, P. Lombardelli, M. J. Pomeroy, "GaAs MMICs for cellular broadband wireless infrastructure: A system perspective", Proc. on IEEE-CAS Region 8 Workshop on Analog and Mixed IC Design, Oct. 1997, pp. 267-270.
- [26] G. Redoelli, S. Marsili, G. Coppola, G. Girola, "Performance evaluation and link budget analysis for 42 GHz local multipoint distribution systems", IEEE Global Telecomms. Conf. (GLOBECOM'99), vol. 5, 1999, pp. 2630-2636.
- [27] A. Nordbotten, "A presentation of the ACTS Project AC215 CRABS: Cellular radio access for broadband services", Int. Zurich Seminar on Digital Comms., Broadband Comms., 1998, pp. 155-158.
- [28] K. H. Craig, (Ed) ACTS Project 215, deliverable report D3P1B, "Propagation planning procedures for LMDS", Jan. 1999, pp. 15-18, 19-22, 39-43, 48-51, 55-58, 61-66.
- [29] D. Penny, "CABSINET", Central Research Laboratories, at <http://www.crl.co.uk/pdfs/cabsinet.pdf>.

- [30] J. P. P. Martínez, "The Madrid multi-access LMDS (28-31 GHz) trial system", at <http://www.cableaml.com/madridtrialsystem.html>.
- [31] Virginia Tech, "LMDS at Virginia Tech", at <http://www.lmds.vt.edu/>
- [32] D. Grace, N. E. Daly, T. C. Tozer, A. G. Burr, "LMDS from high altitude aeronautical platforms", IEEE Global Telecomms. Conf. (GLOBECOM 99), Dec. 1999, vol. 5, pp. 2625-2629.
- [33] T. C. Tozer and D. Grace, "High-altitude platforms for wireless communications", Electronics and Comm. Eng. Jour., June. 2001, vol. 13, no. 3, pp. 127-137.
- [34] HeliNet, at <http://www.helinet.polito.it/>
- [35] CAPANINA project, at <http://www.capanina.org/>
- [36] S. R. Saunders, "Antennas and propagation for wireless communication systems", John Wiley and Sons, Dec. 1999, pp. 2-3, 40-42, 45-55, 104-106.
- [37] T. S. Rappaport, "Wireless Communications Principles and Practice", Prentice Hall, 1996.
- [38] W. Rummler, "Multipath fading channel models for microwave digital radio", IEEE Com. Mag., Nov. 1986, vol. 24, pp. 30-42.
- [39] D. A. Kapp, G. S. Brown, "Effect of correlation between shadowing and shadowed points in rough surface scattering", IEEE Trans. on Ant. and Propag., Aug. 1994, vol. 42, pp. 1154-1160.
- [40] D. A. Kapp, G. S. Brown, "A new numerical method for rough-surface scattering calculations", IEEE Trans. on Ant. Propag., May 1996, vol. 44, pp. 711-721.

- [41] E. J. Violette, R. H. Espeland, R. O. DeBolt, F. Schwering, "Millimeter-wave propagation at street level in urban environment", *IEEE Trans. on Geosci. and Remote Sensing*, May 1988, vol. 26, pp. 368-380.
- [42] B. Langen, G. Lober, W. Herzig, "Reflection and transmission behaviour of building materials at 60 GHz", 5th IEEE Int. Symp. on Personal, Indoor and Mobile Radio Comms (PIMRC'94), Amsterdam, Netherlands, Sept. 1994. pp. 505-509.
- [43] Recommendation ITU-R P.530-9, "Propagation data and prediction methods required for the design of terrestrial line-of-sight systems", May 2001.
- [44] F. K. Schwering, E. J. Violette, R. H. Espeland, "Millimeter-wave propagation in vegetation: Experiments and theory", *IEEE Trans. on Geosci. and Remote Sensing*, May 1988, vol. 26, pp. 355-367.
- [45] F. T. Ulaby, T. A. V. Deventer, J. R. East, M. E. Coluzzi, "Millimeter-wave bistatic scattering from ground vegetation target", *IEEE Trans. on Geosci. and Remote Sensing*, May 1988, vol. 26, no. 3, pp. 329-243.
- [46] P. B. Papazian, G. A. Hufford, R. J. Achatz, R. Hoffman, "Study of the local multipoint distribution service radio channel", *IEEE Trans. on Broadcasting*, June 1997, vol. 43, no. 2, pp. 175-184.
- [47] G. M. Whitman, F. K. Schwering, A. A. Triolo, "A transport theory of pulse propagation in a strongly forward scattering random medium", *IEEE Trans. on Ant. and Propag.*, Jan. 1996, vol. 44, no. 1, pp. 118-128.
- [48] F. T. Ulaby, T. E. Van Deventer, J. R. East, T. F. Haddock, and M. E. Coluzzi, "MM-wave bistatic scattering from ground and vegetation targets", *IEEE Trans. on Geosci. Remote Sensing*, May 1988, vol. 26, pp. 229-242.

- [49] A. Lopes, E. Mougín, T. Le Toan, M. A. Karam, and A. K. Fung, "A simulation study on the influence of leaf orientation on elliptically polarized microwave propagation in a coniferous forest", *J. Electromag. Waves Applicat.*, 1991, vol. 5, no. 7, pp. 753-776.
- [50] S. A. Torrico, H. L. Bertoni, and R. H. Lang, "Modeling tree effects on path loss in a residential environment", *IEEE Trans. Ants. Propagat.*, Jun. 1998, vol. 46, pp. 872-880.
- [51] Y.-C. Lin and K. Sarabandi, "A Monte Carlo coherent scattering model for forest canopies using fractal-generated trees", *IEEE Trans. on Geosci. Remote Sensing*, Jan. 1999, vol. 37, pp. 440-451.
- [52] COST Action 235, "Radiowave propagation effects on next-generation fixed-services terrestrial telecommunications systems - Final report", *Eur. Cooperation Field Sci. Tech. Res.*, Eur. Commission, Luxembourg, 1996.
- [53] A. Seville, K. H. Craig, "Semi-empirical model for millimetre-wave vegetation attenuation rates", *Elec. Letters*, Aug. 1995, vol. 31, no. 17, pp. 1507-1508.
- [54] A. Seville, "Vegetation attenuation: Modelling and measurements at millimetric frequencies", 10th. Int. Conf. on Ant. and Propg., 14-17 Apr. 1997.
- [55] A. Kajiwara, "LMDS radio channel obstructed by foliage", *IEEE Int. Conf. on Comms. (ICC 2000) Global Conv. Through Comms.*, 2000, vol. 3, pp. 1583-1587.
- [56] A. Ishimaru, "Wave propagation and scattering in random media", Academic Press, 1978, vol. 1, chap. 7.

- [57] R. F. S. Caldeirinha, M. O. Al-Nuaimi, "Propagation modelling of bistatic scattering of isolated trees for micro- and millimeter wave urban microcells", Proc. of 13th IEEE Int. Symp. on Personal Indoor and Mobile Radio Comms. (PIMRC 2002), Lisbon, Portugal, Sept. 2002.
- [58] D. Didascalou, M. Younis and W. Wiesbeck, "Millimeter-wave scattering and penetration in isolated vegetation structures", IEEE Trans. on Geosc. and Remote Sensing, Sept. 2000, vol. 38, no. 5, pp. 2106-2113.
- [59] A. Seville, P. G. V. Charriere, N. Powell, K. H. Craig, "Building scatter and vegetation attenuation measurements at 38 GHz", 9th Int. Conf. on Ants. and Propag., IEE. 1995, Part vol. 2, pp. 46-50.
- [60] Recommendation ITU-R P.833-3, "Attenuation in vegetation", Feb. 2001.
- [61] I. J. Dilworth, "Millimetre wave attenuation and cross-polarisation scattering from foliage and building structures", Int. Conf. on Ant. and Propag., Eindhoven, Holland, Apr. 1995, pp. 51-53.
- [62] I. J. Dilworth, "Attenuation and cross-polarisation caused by trees at millimetre wavelengths", IEE Electronics Letters, Feb. 1996, vol. 32, no. 5, pp. 488-489.
- [63] R. L. Olsen, D. V. Rogers, D. B. Hodge, "The  $aR^b$  relation in the calculation of rain attenuation", IEEE Trans. on Antennas and Propagation, March 1978, vol. AP-26, pp. 318-329.
- [64] R. K. Crane, "Prediction of attenuation by rain", IEEE Trans. on Communications, Sept. 1980, vol. COM-28, pp. 1717-1733.
- [65] D. D. Wolf, L. Lighthart, "Multipath effects due to rain at 30-50 GHz frequency communication links", IEEE Trans. Ant. Propag., Aug. 1993, pp. 1132-1138.

- [66] S. O. Ajose, M. N. Sadiku, U. Goni, "Computation of attenuation, phase rotation, and cross-polarisation of radio waves due to rainfall in tropical regions", *IEEE Trans. Ant. Propag.*, Jan. 1995, pp. 1-5.
- [67] R. K. Crane, "Electromagnetic Wave Propagation Through Rain", John Wiley and Sons, 1996.
- [68] S. Y. Seidel, H. W. Arnold, "Propagation measurements at 28 GHz to investigate the performance of local multipoint distribution service (LMDS)", *IEEE Global Telecomms. Conf.*, vol. 1, 1995, pp. 754-757.
- [69] H. Fukuchi, P. A. Watson, "Statistical stability of cumulative distributions of rainfall rate in the UK", *IEE Procs on Microwaves Ants. and Propag.*, Apr. 1989, vol. 136, no. 2, pp. 105-109.
- [70] Recommendation ITU-R P.838-1, "Specific attenuation model for rain for use in prediction methods", Nov. 1999.
- [71] Recommendation ITU-R P.837-3, "Characteristics of precipitation for propagation modelling", Mar. 2001.
- [72] J. W. F. Goddard, M. Thurai, "Radar-derived path reduction factors for terrestrial systems", 10th Int. Conf. on Ants. and Propag., IEE. 1997, vol. 2, pp. 218-221.
- [73] K. S. Paulson, C. J. Gibbins, "Rain models for the prediction of fade durations at millimetre wavelengths", *IEE Proc. on Microwaves Ants and Propag.*, Dec. 2000, vol. 147, no. 6, pp.431-436.
- [74] C. J. Gibbins, M. Thurai, K. S. Paulson, "Durations of rain events and rain attenuations at millimetric wavelengths", AP2000 Millenium Conf. on Ant. and Propag., Switzerland, April 2000.

- [75] Recommendation ITU-R P.676-5, "Attenuation by atmospheric gases", Feb. 2001.
- [76] D. C. Hogg, "Path diversity in propagation of millimetre waves through rain", *IEEE Trans. Ant. Propag.*, May 1967, vol. AP-15, pp. 410-415.
- [77] C. Enjamio, E. Vilar, F. PP. Fontan, "Spatial distribution of rainfall rate: Benefits of the site diversity as a dynamic fade mitigation technique", COST 280 1st Int. Workshop, Malvern, U.K., Jul. 2002.
- [78] S. Callaghan, E. Vilar, "Spatial variation of rain fields in the south of England", COST 280 1st Int. Workshop, Malvern, U.K., Jul. 2002.
- [79] I. Usman, M. Willis, R. Watson, "Route diversity analysis and modelling for millimeter-wave point to multi-point systems", COST 280 1st Int. Workshop, Malvern, U.K., Jul. 2002.
- [80] N. Naz, D. Falconer, "Temporal variations characterization for fixed wireless at 29.5 GHz", *IEEE 51st Vehicular Tech. Conf. Procs. 2000 (VTC2000)*, May 2000, pt. 3, vol. 3, pp. 2178-2182.
- [81] S. Perras, L. Bouchard, "Fading characteristics of RF signals due to foliage in frequency bands from 2 to 60 GHz", 5th. Int. Symp. on Wireless Personal Multimedia Comms. (WPMC 2002), Oct. 2002.
- [82] A. Paulsen, P. Lindholm, T. Tjelta, K. Craig, M. J, Willis, I. Usman, "Antenna diversity as a means of overcoming vegetation fading at 42 GHz", COST 280 1st Int. Workshop, Malvern, U.K., Jul. 2002.
- [83] J. Maurer, D. Didascalou, V. Engels, W. Wiesbeck, "Wideband wave propagation measurements for local multipoint distribution services (LMDS) at 26 GHz", 52nd. *IEEE Vehicular Tech. Conf.*, 2000, pp. 1902-1908.

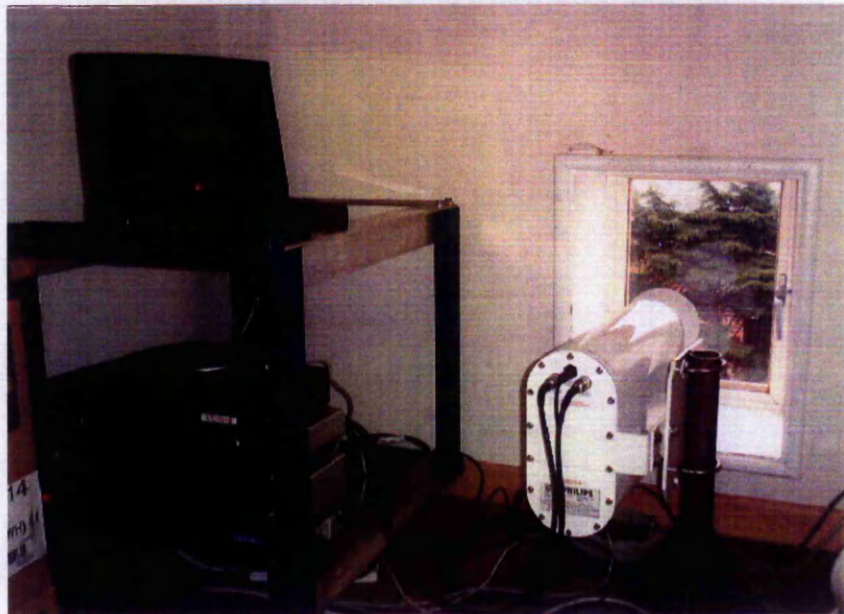
- [84] S. Y. Seidel, "Radio propagation and planning at 28 GHz for local multipoint distribution service (LMDS)", IEEE Ants. and Propag. Soc. Int. Symp., 1998, pp. 622-625.
- [85] P. Forni, "Millimetre wave propagation: A measurement expert system for the millimetre wave propagation modelling validation", 10th. Int. Conf. on Ant. and Propag., Edinburgh, U.K., Apr. 1997.
- [86] A. Hayn, R. Bose, R. Jakoby, "Multipath propagation and LOS interference studies for LMDS architecture", 11th Int. Conf. on Ant. and Propag., Manchester, U.K., Apr. 2001, pp. 686-690.
- [87] I. Glover, P. Grant, "Digital Communications", Prentice Hall, 1998.
- [88] European Telecommunication Standards Institute, TR 101 290, "DVB: Measurement guidelines for DVB systems", May 2001.
- [89] HUMAX, "Humax F1-FOX operating manual",  
at <http://www.humaxdigital.com/HCSA/usersmanual.asp>.
- [90] Philips Semiconductors product specification, "OM5721 - STB5660 (set-top box) STB concept", May 1999.
- [91] C. M. Buck, R. Germon, R. Pitt, D. Roulston, "Millimetre wave components for MVDS", IEE Colloquium on MM-Wave Circuits and Tech. for Commercial Apps., 1999, pp. 1/1-4.
- [92] Philips Semiconductor, "The I<sup>2</sup>C bus specification version 2.1", Jan 2000,  
at <http://www.semiconductors.philips.com/buses/i2c/>

- [93] Dallas Semiconductor application note, "AN619 - Using maxim RTCs with 3-wire interface", Jun. 2001,  
at [http://www.maxim-ic.com/appnotes.cfm/appnote\\_number/619/ln/en](http://www.maxim-ic.com/appnotes.cfm/appnote_number/619/ln/en).
- [94] Samsung Semiconductor datasheet, "K9S5608V0A-SSB0 - 32M x 8 Bit SmartMedia Card", Nov. 2000, at <http://www.samsung.com/Products/Semiconductor/Flash/>
- [95] D. Awtrey, "The 1-wire weather station", Sensors, Jun. 1998,  
at <http://www.ibutton.com/weather/>
- [96] D. Awtrey, "Transmitting data and power over a one-wire bus", Sensors, Feb. 1977,  
pp. 48-51.
- [97] N. Merryweather-Clarke, C. J. Gibbins, D. N. Ladd, "The statistics of propagation on the 500 m millimetre wave experiment at Chilbolton", 10th. Int. Conf. on Ants. and Propag. 1997, pt. 2, vol. 2, pp. 374-377.
- [98] T. Brabetz, N.B. Buchanan, V.F. Fusco, "Temperature dependence of millimetre-wave MMICs," IEE Electronics Letters, Sept. 2000, vol. 36, no. 23,  
pp. 1976-1977.
- [99] R. Esfandiari, T. J. O'Neill, T. S. Lin, R. K. Kono, "Accelerated aging and long-term reliability study of ion-implanted GaAs MMIC IF amplifier", Apr. 1990, vol. 37,  
no. 4, pp. 1174-1177.
- [100] D. Tse, P. Viswanath, "Fundamentals of wireless communication", Jan. 2004, pp. 36,  
at <http://www-inst.eecs.berkeley.edu/~ee224b/sp04/>
- [101] M. Basseville, I. V. Nikofof, "Detection of abrupt changes: Theory and application", Prentice-Hall, 1993.

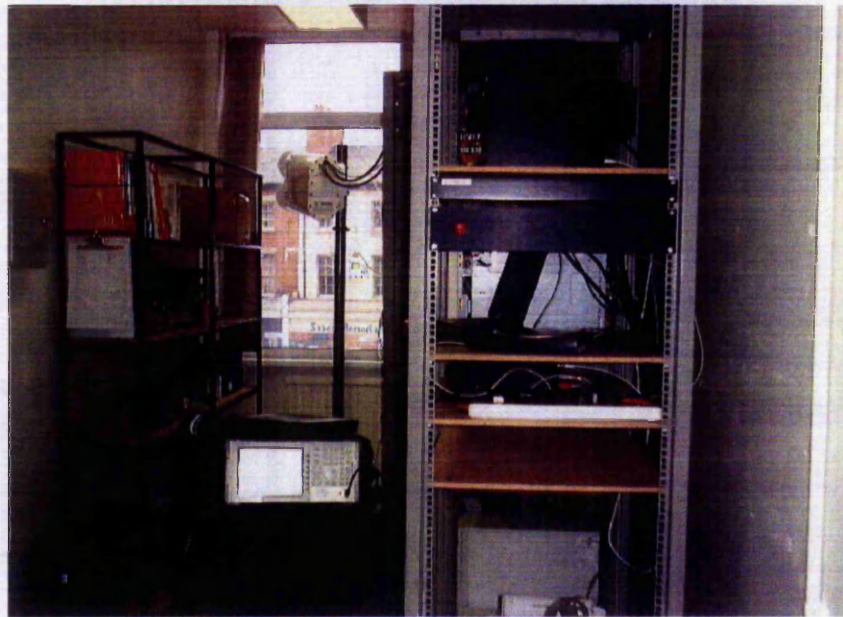
- [102] M. Das, A. Coopriker, "New techniques for detection of changes in the local mean of a signal", Midwest Symp. on Circuits and Systems, 1997, vol. 2, pp. 849-852.
- [103] D. M. Hawkins, D. H. Olwell, "Cumulative sum charts and charting for quality improvement", Springer-Verlag, 1997.
- [104] D. Hinkley, "Inference about the change-point from cumulative sum tests", *Biometrika*, Dec. 1971, vol. 58, iss. 3, pp. 509-523.
- [105] D. Hinkley, E. Schechtman, "Conditional bootstrap methods in the mean-shift model", *Biometrika*, Mar. 1987, vol. 74, iss. 1, pp. 85-93.
- [106] B. F. J. Manly, D. MacKenzie, "A cumulative sum type of method for environmental monitoring", *Environmetrics*, 2000, iss. 11, pp. 151-166.
- [107] E.S. Page, "Continuous inspection schemes", *Biometrika*, Jun. 1954, vol. 21, iss. 1/2, pp. 100-115.
- [108] B. F. J. Manly, "Randomization, bootstrap and Monte Carlo methods in biology", Chapman and Hall, 1997, 2nd ed., pp. 1-23, 79-90, 225-258.
- [109] M. Kamp, L. Castanet, "Fade dynamics review", COST 280 1st Int. Workshop, Malvern, U.K., Jul. 2002.
- [110] Recommendation ITU-R P.1057, "Probability distributions relevant to radiowave propagation modelling", 1994.
- [111] R. B. D'Agostino, M. A. Stephens, "Goodness-of-fit techniques", Marcel Dekker Inc., 1986, pp. 111-114, 372-374.
- [112] B. Biller, B. L. Nelson, "Answers to the top ten input modeling questions", *Procs. of the 2002 Winter Simulation Conf.*, 2002, vol. 1, pt. 1, pp. 35-40.

[113] Decisioneering, "Crystal Ball – User manual", 2004,  
at [http://www.decisioneering.com/crystal\\_ball/index.html](http://www.decisioneering.com/crystal_ball/index.html)

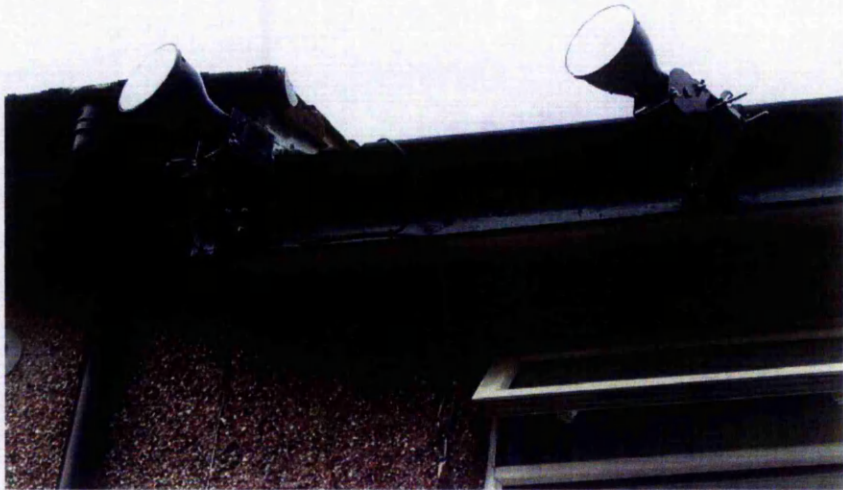
**APPENDIX A - PHOTOS OF REMOTE SITES**



**Remote site photos of Blenheim Hall of Residence, on link  $L_{BHall}$ .**



Remote site photos of York House, on link  $L_{YHouse}$



Remote site photo of Residence House 1, on link  $L_{Tree+path}$  and  $L_{Home LOS}$ .



Remote site photo of Residence House 2, on link  $L_{Home 2}$ .